2016

Quantification of the Effect of Degassing on the Microstructure, Chemistry and Estimated Strength of Nanocrystalline AA5083 Powder

Clara Hofmeister
University of Central Florida

QUANTIFICATION OF THE EFFECT OF DEGASSING ON THE MICROSTRUCTURE, CHEMISTRY AND ESTIMATED STRENGTH OF NANOCRYSTALLINE AA5083 POWDER

by

CLARA M. HOFMEISTER
B.S. University of Central Florida, 2010
M.S. University of Central Florida, 2013

A dissertation submitted in partial fulfillment of the requirements
for the degree of Doctor of Philosophy
in the Department of Materials Science and Engineering
in the College of Engineering and Computer Science
at the University of Central Florida
Orlando, Florida

Fall Term
2016

Major Professor: Yongho Sohn

ABSTRACT

Degassing is a critical heat treatment process in aluminum powder metallurgy, where powders are subjected to high temperature in vacuum to remove volatile gaseous species absorbed in and adsorbed on powders. For cryomilled aluminum alloy powders with nanoscale features, degassing can cause accelerated microstructural and chemical changes including removal of volatiles, grain growth, dislocation annihilation, and formation of dispersoids. These changes can significantly alter the mechanical behavior of consolidated components based on their contributions to strength. In this study, cryomilled AA5083 (0.4 wt.% Mn; 4.5 wt.% Mg; minor Si, Fe, Cu, Cr, Zn, Ti; balance Al) powders were degassed at 200, 300, 350, 410 and 500°C at a ramp rate of 68.3 °C·hr^{-1} for a soak time of 8 hours with a vacuum at or below 6.5 x 10^{-3} Pa. Grain size, dislocation density and dispersoid phase constituents were examined as a function of degassing temperature by X-ray diffraction, scanning electron microscopy and transmission electron microscopy, equipped with high angle annular dark field detector and X-ray energy dispersive spectroscopy. Inert gas fusion and thermal conductivity analysis were employed to determine the oxygen, nitrogen and hydrogen concentrations as a function of degassing temperature. Grain size in as-cryomilled powders (21 ~ 34 nm) increased as a function of degassing temperature, and reached a maximum value of 70 ~ 80 nm for powders degassed at 500°C for 8 hours. The dislocation density of 1.11 x 10^{15} m^{-2} in as-cryomilled powders decreased to 1.56 x 10^{14} m^{-2} for powders degassed at 500°C for 8 hours. The Al_6(MnFeCr) phase was the most commonly observed dispersoid, mostly on samples degassed at or above 300°C. Volume

fraction increased with degassing temperature up to 5 vol.% and the size of the dispersoids grew up to ~ 280 nm. Oxygen and nitrogen content after cryomilling were unaffected by the change in degassing temperature, but the hydrogen content decreased and reached a minimum of 45 ± 3.16 ppm for cryomilled powders degassed at 500°C for 8 hours. Grain growth was quantitatively analyzed based on the general grain growth formula and Burke's model in the presence of pinning forces. Degassing occurred in two different kinetic regimes: Harrison A kinetics at higher temperatures and Harrison B in the lower with a transition temperature of about 287°C. Burke's model exhibited a poor fit to the experimental results in higher temperature regime. Desorption of impurities during degassing was analyzed using Fickian diffusion in a spherical coordinate system and an empirical expression based on the exponential decay of average concentration. The activation energy for degassing was estimated to be 16.2 ± 1.5 $kJ \cdot mol^{-1}$. Evolutions in composition and microstructure in cryomilled powders as a function of degassing temperature were further analyzed and quantitatively correlated to the strengthening mechanisms of solid solution, grain size reduction (i.e., Hall-Petch), dislocation forest and Orowan. For consolidated AA5083 derived from cryomilled powders, strengthening by grain size reduction was the dominant mechanism of strengthening.

ACKNOWLEDGMENTS

First and foremost, thanks be to God who has sustained me through this work. In addition, I would like to thank my friends and family for their patience as I have focused on my research. Without their support and understanding this would not have been possible.

I would like to thank my advisor and chairman Dr. Yongho Sohn for your time and patience with me through all these years. I look forward to continuing our professional relationship as I go out and conduct research in the 'real world'. I would like to also express gratitude to my committee members, Dr. Kevin Coffey, Dr. Challapalli Suryanarayana, Dr. Stephen Kuebler, and Dr. Tengfei Jiang for your time and consideration of this work. Finally, the use of the Materials Characterization Facility is gratefully acknowledged.

This research was sponsored by the U.S. Army Research Laboratory and was accomplished under Cooperative Agreement W911NF-11-2-0020. The views, opinions, and conclusions made in this document are those of the authors and should not be interpreted as representing the official policies, either expressed or implied, of the Army Research Laboratory or the U.S. Government. The U.S. Government is authorized to reproduce and distribute reprints for Government purposes notwithstanding any copyright notation herein.

TABLE OF CONTENTS

LIST OF FIGURES

LIST OF TABLES

LIST OF ACRONYMS

a	radius of sphere
A	constant defined by equation (6.8), see section 6.3
A	constant in the exponential decay function, see section 6.3
A_A	atomic mass of element A
a_{Al}	atomic percent of Al as Al4C3
A_{Al}	atomic mass of Al
Al_2O_3	aluminum oxide
$Al_2O_3 \cdot 3H_2O$	aluminum hydroxide
Al_4C_3	aluminum carbide
$Al_6(MnFeCr)$	aluminum manganese iron chromium
Al_6Mn	aluminum manganese
AlN	aluminum nitride
A_n	atomic mass of element n
b	burgers vector, for Al = 0.286 nm
B	constant defined by equation (6.14), see section 6.3
B	constant in the exponential decay function, see section 6.3
B'	constant defined by equation (6.9), see section 6.3
BF	bright field
BSE	backscatter electron microscopy
C	constant equal to Q/R

C_1	initial concentration of the sphere
C_s	concentration just within the sphere
D	instantaneous grain size at time t
D	diffusivity
d_1	diameter of the aluminum part of the powder particle without the oxide shell
d_2	diameter of powder particle
d_{Al}	aluminum grain size
D_{AlAl}	diffusivity of Al in an Al lattice
D_{max}	maximum grain size where a pinning force is possible
D_o	initial grain size
d_{OS}	diameter of the dispersoids
DSC	differential scanning calorimetry
EDS	energy dispersive spectroscopy
F	volume fraction
f	volume percent
FIB	focused ion beam
G	shear modulus
HAADF	high angle annular dark field
INLO	in situ lift out
I	integrated intensity
JCPDS	Joint Committee on Powder Diffraction Standards

k	grain growth rate constant
k	constant in the exponential decay function, see section 6.3
k_{HP}	Hall-Petch coefficient
k_o	temperature-independent rate constant
L	coefficient defined by $a\alpha/D$, see equation (6.4) section 6.1
M	Taylor constant in dislocation forest strengthening equation, equal to 2.7
M_∞	total amount of remaining solute at $t = \infty$
$Mg(OH)_2$	magnesium hydroxide
M_t	total amount of remaining solute at time t
n	grain growth exponent
n	constant in the exponential decay function, see section 6.3
PCA	process control agent
PPM	parts per million
Q	activation energy
Q_{Gb}	activation energy for Al grain boundary diffusion
Q_H	activation energy for grain growth in the high temperature regime
Q_L	activation energy for grain growth in the low temperature regime
Q_{Latt}	activation energy for self-diffusion of Al in the lattice
R	gas constant, equal to 8.314 $J \cdot mol^{-1} \cdot K^{-1}$

R	distance from the center of the sphere
SEM	scanning electron microscopy
SS	solid solution
t	thickness of oxide layer
t	time
T	temperature
TEM	transmission electron microscopy
T_m	melting temperature
v^f	volume fraction
v^f	volume fraction of grain boundaries
V_{Gb}	volume of grain boundary
V_{oxide}	volume of oxide
w_A	weight percent of element A
$w_{Al6(MnFeCr)}$	weight percent of Al6(MnFeCr)
w_n	weight percent of element n
XEDS	X-ray energy dispersive spectroscopy
XRD	X-ray diffraction
Y	concentration of hydrogen in ppm
α	constant in dislocation forest strengthening equation, equal to 0.3
α	solid-gas distribution ratio
β_n	roots of equation (6.5), see section 6.1

δ	width of the grain boundary
ε	microstrain
Λ	coefficient used to determine onset of Harrison A kinetics regime, see equation (5.4) in section 5.2
λ	distance between dispersoids
ρ	dislocation density
ρ_{AA5083}	density of AA5083 which is equal to 2.66 $g \cdot cm^{-3}$
ρ_{Al4C3}	density of Al4C3, equal to 2.98 $g \cdot cm^{-3}$
ρ_{Al6Mn}	density of Al6Mn, equal to 3.32 $g \cdot cm^{-3}$
σ'_{HP}	Hall-Petch strengthening including the friction stress
$\sigma_{carbides}$	Orowan strengthening contribution from the presence of the nanoscale Al_4C_3
σ_f	dislocation forest strengthening
σ_{HP}	Hall-Petch strengthening
$\sigma_{nitrides}$	Orowan strengthening contribution as a result of the presence of nitrides
σ_o	friction stress
σ_{Orowan}	Orowan strengthening contribution from the $Al_6(MnFeCr)$ dispersoid
σ_{OS}	Orowan strengthening
σ_{oxides}	Orowan strengthening due to nanoscale Al_2O_3
σ_Y	total strength

CHAPTER 1: INTRODUCTION

The automotive industry is consistently striving to produce higher performing, faster vehicles while reducing the carbon-based emissions. One of the most common ways manufacturers have met these demands is by reducing the weight of their vehicles utilizing low density materials. If vehicle components consisting of steel (7.75 $g \cdot cm^{-3}$) could be replaced by a lighter weight material, fuel efficiency could be dramatically improved. Aluminum alloys (~2.7 $g \cdot cm^{-3}$) are of great interest for the development of lightweight vehicles however their low strength has limited its practical applications. Nanostructuring the grains can be used to increase the overall strength of the aluminum alloy.

Powder metallurgy techniques have the ability to produce parts with chemical homogeneity in mass production with short production times. Additional processing steps can be added into the powder metallurgy process to increase the strength of the resultant parts. A schematic of a typical processing sequence for producing parts with enhanced strength via cryomilling for aluminum powders is presented in Figure 1.

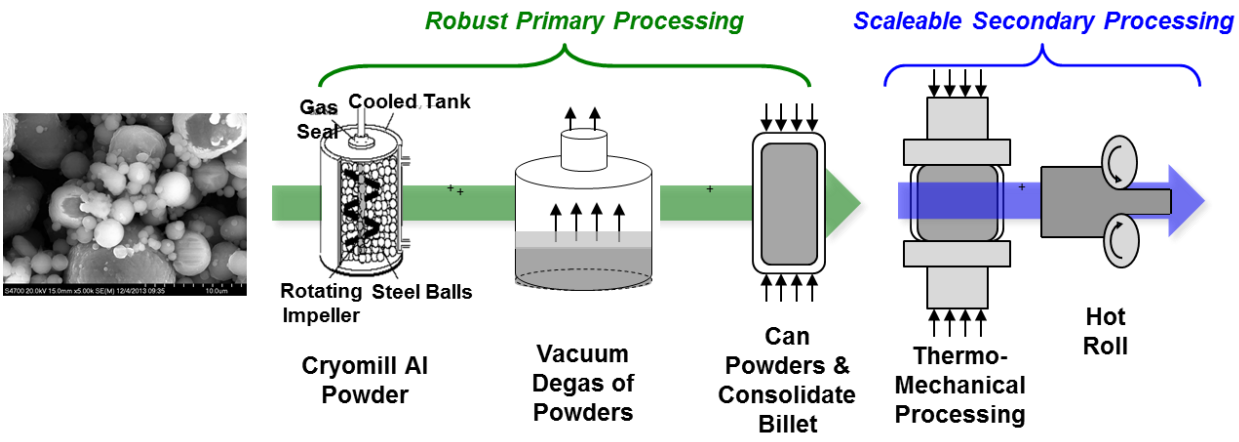

Figure 1: Schematic for cryomilled powder processing. Adapted from Figure 1 of Sohn et al. [1].

The cryomilling process consists of attritor ball milling aluminum powders in the presence of liquid nitrogen. In this step, powders are severe plastically deformed through a simultaneous fracturing and cold welding process reducing the grain size of the aluminum powders to a minimum of about 20 nm [2, 3]. Liquid nitrogen provides environmental protection for the powders thus minimizing oxidation and produces several nanometer-sized dispersoids. These dispersoids help pin grain boundaries and provide additional strengthening to the material [2, 4, 5].

Moisture and other volatiles are trapped in the material during gas atomization and subsequent processing and handling. These gases, if not properly removed during the degassing step, will desorb from the bulk during consolidation and subsequent secondary processing which may cause microcracks and blistering in the part [6]. Therefore, after cryomilling, it is necessary to degas the powder before subsequent consolidation and secondary processing. The process of degassing involves placing the powder in a controlled environment such as nitrogen or vacuum and heating the powder. This process changes the chemistry of the powders by removing adsorbed gases and induces microstructural changes such as precipitation and grain growth. The purpose of this study will be to qualitatively and quantitatively understand the effect of degassing on the microstructure, chemistry and expected mechanical properties of cryomilled aluminum powders by experimentally varying the processing conditions as well as thermo-kinetic modeling of the grain structure via the general grain growth and Burke's grain growth equations as well as chemical evolution with Fickian diffusion and empirical relationships.

CHAPTER 2: MECHANICAL PROPERTY PARAMETRIC STUDY

The microstructure of cryomilled aluminum powders consists of several features which contribute to the overall strength of the material. During cryomilling, dislocations accumulate in the material producing a nanocrystalline grain size and high dislocation density [2, 7, 8]. If an alloy is used and the composition exceeds the solubility limits, intermetallic phases may be present depending on the processing parameters used to create the powder. Intermetallics present in the powder before cryomilling may become mechanically alloyed into the matrix material or simply be reduced in size during cryomilling [9]. Other phases that have been observed in cryomilled aluminum are fine nanoscale dispersoids such as oxides, carbides and nitrides [2, 4, 5, 10]. In brief, the mechanical properties of cryomilled aluminum alloys are affected by:

1. Choice of alloy
2. Nanocrystalline grain structure
3. High dislocation density
4. Presence of large intermetallic dispersoids
5. Presence of fine nanoscale dispersoids

All of these microstructural features contribute towards the total strength of the cryomilled material. In this chapter, a comprehensive study on each of these strengthening mechanisms was conducted to 1) estimate the range of strength provided by each mechanism, 2) determine which one is most critical to the strength of the material, 3) use this information to rationalize the experimental parameters for the degassing study in the following chapters.

2.1 Effect of Alloy Choice

The 5000 series aluminum alloys are non-heat treatable, corrosion resistant, weldable, strain hardened and are commonly used in architectural trim, cans, household appliances, street lights, marine craft, crane parts and automotive structures [11]. The 5000 series aluminum alloys attractive for this study because they are strain hardened and cryomilling introduces significant strain during mechanical attrition therefore the resultant material should exhibit high strength. The primary alloying elements in the 5000 series aluminum alloys are magnesium with a small amount of manganese (typically ≤ 1.4 wt.%) [12]. In a study by Nam and Lee in 2000, alloying with Mn in the range of 0.7 – 1.2 wt.% was found to increase the strength of conventional aluminum alloys without decreasing ductility [13]. The added Mn formed the Al_6Mn dispersoid which contributed to the overall strength through the Orowan mechanism.

According to the Al-Mg phase diagram, the maximum solubility of Mg in Al solid solution (SS) is 17.1 wt.% at 450°C [14]. Because of its high solubility in Al, Mg is used to increase the strength of the alloy through solid solution strengthening. However, as the temperature drops, so does the solubility of Mg in Al. The solubility of Mg in Al at 100°C is only ~1 wt.% Mg [14]. As a result of this, processing at low temperatures can result in formation of the Al_3Mg_2 phase. This phase is unfavorable because it precipitates along the grain boundaries and has been directly correlated to the susceptibility of the alloy to stress corrosion cracking [15]. Fortunately, this phase will dissolve at relatively modest temperatures. For example, Sridharan et al. found that this phase will dissolve in alloys such as AA5083 (4.0 – 4.9 wt.% Mg) and AA5059 (5.0-6.0 wt.% Mg) when processing above ~300°C [15]. Therefore, a simple heat treatment will dissolve the Al_3Mg_2 phase.

The Al-rich region of the Al-Mg-Mn ternary phase diagram at 400°C is provided in Figure 2. For most of the 5000 series aluminum alloys, the alloying content of Mg and Mn results in a two phase mixture of Al (SS) and Al_6Mn. The addition of Mn decreases the solubility of Mg in Al(SS). For example, if only a small amount of Mn is added (≤1 wt.%), up to ~7 wt.% Mg can be added for solid solution strengthening before the ternary compound τ ($Mn_2Mg_3Al_{18}$) forms.

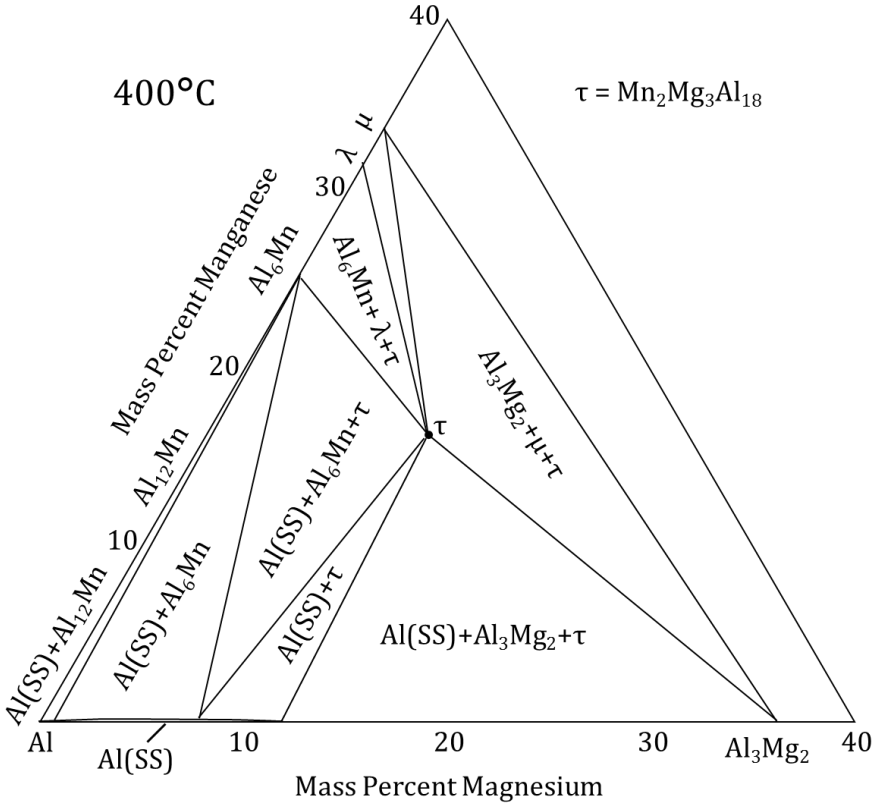

Figure 2: The Al-rich portion of the Al-Mg-Mn ternary phase diagram at 400°C. Adapted from Figure 7 of Raghavan [16].

Table 1 is a list of some 5000 series alloys which contain the highest magnesium alloying content. The list is derived primarily from the ASM Metals Handbook [12] but a

few of the alloys come from other literature. The table is organized in order of lowest to highest magnesium content for easy reference. The alloy with the highest magnesium content, to the author's knowledge, is AA5059 with 5.0 – 6.0 wt.% Mg. However, AA5083 was chosen for this study due to its relatively low cost and the prevalence of related data in the literature.

Table 1: Alloying content for several high Mg content alloys. The range of alloying content for all alloys described come from the ASM Metals Handbook Volume 2 [12] except for alloys 5019 and 5059 which come from Matweb.com.

Aluminum Association	Si (wt.%)	Fe (wt.%)	Cu (wt.%)	Mn (wt.%)	Mg (wt.%)	Cr (wt.%)	Ni (wt.%)	Zn (wt.%)	Ti (wt.%)	Zr (wt.%)	Other	Al
5083	0.4-0.7	0.4	0.1	0.4-1.0	4.0-4.9	0.05-0.25	…	0.25	0.15	…	0.15	Bal
5082	0.2	0.35	0.15	0.15	4.0-5.0	0.15	…	0.25	0.1	…	0.15	Bal
5182	0.2	0.35	0.15	0.2-0.5	4.0-5.0	0.1	…	0.25	0.1	…	0.15	Bal
5014	0.4	0.4	0.2	0.2-0.9	4.0-5.5	0.2	…	0.7-1.5	0.2	…	0.15	Bal
5183	0.4-0.7	0.4	0.1	0.5-1	4.3-5.2	0.05-0.25	…	0.25	0.15	…	0.15	Bal
5283	0.3	0.3	0.03	0.5-1	4.5-5.1	0.05	0.03	0.1	0.03	…	0.15	Bal
5356	0.25	0.4	0.1	0.05-0.2	4.5-5.5	0.05-0.2	…	0.1	0.06-0.2	…	0.15	Bal
5056	0.3	0.4	0.1	0.05-0.2	4.5-5.6	0.05-0.2	…	0.1	…	…	0.15	Bal
5019	0.4	0.5	0.1	0.1-0.6	4.5-5.6	0.2	…	0.2	0.2	…	0.15	Bal
5456	0.25	0.4	0.1	0.5-1	4.7-5.5	0.05-0.2	…	0.25	0.2	…	0.15	Bal
5556	0.25	0.4	0.1	0.5-1	4.7-5.5	0.05-0.2	…	0.25	0.05-0.2	…	0.15	Bal
5059	0.45	0.5	0.25	0.6-1.2	5.0-6.0	0.25	…	0.4-0.9	0.2	0.05-0.25	0.15	Bal

Friction stress, σ_o, is often described in the literature as the inherent strength of a material or the amount of stress required to push a dislocation through a perfect lattice of atoms. Although the term is typically associated with pure materials, σ_o can also be determined for alloys. In this way, the friction stress is a combination of the inherent

strength of a pure lattice plus the contribution from solid solution strengthening. The friction stress is most commonly calculated during studies determining the relationship between grain size and yield strength as described by the Hall-Petch equation [17]:

$$\sigma'_{HP} = \sigma_o + k_{HP}\left(d_{Al}\right)^{-1/2} \quad (2.1)$$

where k_{HP} is the Hall-Petch coefficient, d_{Al} is the aluminum grain size and σ'_{HP} is the increase in strength.

A study by Hasegawa et al. examined the Hall-Petch behavior for pure Al and Al binary alloys containing 1 and 3 wt.% Mg through compression testing for grain sizes ranging from 250 nm to 582 μm [18]. They found that both pure Al and the Al binary alloys followed the Hall-Petch relationship for the grain size range studied. The values determined by Hasegawa et al. for σ_o and k_{HP} are plotted as open circles in Figure 3a and b respectively. Furukawa et al. also determined the friction stress and Hall-Petch coefficient for the Al-3wt.% Mg binary alloy through compression testing for a grain size range from 200 nm – 144 μm and their results are included as a solid diamond for comparison in Figure 3a and b.

The increase in Mg content lead to an increase in both the friction stress and the Hall-Petch coefficient. In Figure 3a, the change in σ_o as a function of Mg content (wt.%) was fitted to a straight line. The y-intercept describes the inherent strength of pure Al which was estimated as 8.6 MPa. The slope of the line can be described as the effect of solid solution strengthening and is 17.4 MPa·(wt.% Mg)$^{-1}$. For AA5083 (4.0-4.9 wt.% Mg), this resulted in a σ_o of 78 – 94 MPa. The change in the Hall-Petch coefficient, k_{HP}, as a function of

Mg alloying content was also fitted to a straight line. The k_{HP} of pure Al was found to be 0.12 MPa·m$^{1/2}$ and increased with Mg alloying content at a rate of 0.01 MPa·m$^{-1/2}$·(wt.% Mg)$^{-1}$. For AA5083, the range of k_{HP} was 0.16 – 0.17 MPa·m$^{1/2}$.

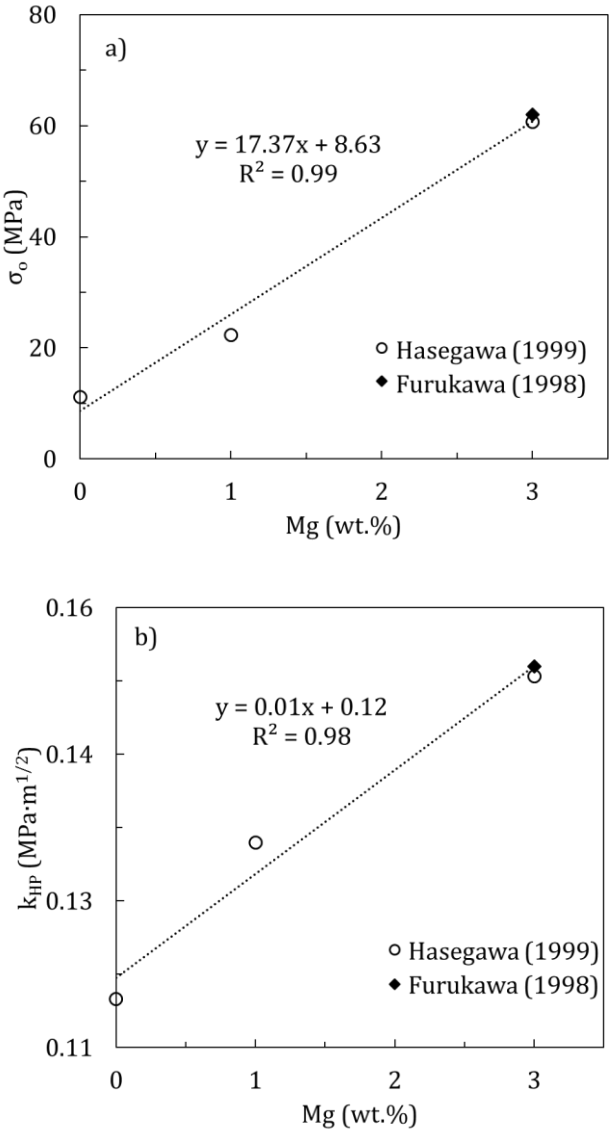

Figure 3: The effect of the addition of Mg content on the a) friction stress, σ_o, and b) the Hall-Petch coefficient, k_{HP}.

2.2 Hall-Petch Behavior

During cryomilling, stainless steel balls collide and crush powder between other balls and the attritor walls. During this process, the aluminum grains undergo severe plastic deformation and restructuring. Fecht described the process in three steps [19]: 1) deformation is localized into shear bands with high dislocation densities, 2) dislocations annihilate and recombine into small angle grain boundaries, 3) further deformation causes grain rotation and grain boundary sliding in such a way that the grain orientation becomes random. In this way, the aluminum grains become nanostructured. Additional milling beyond ~12 hours does not decrease the grain size further [3] and the minimum grain size for cryomilled Al has been determined as ~ 20 nm [2].

Further milling however, can lead to additional nitrogen incorporation into the material through mechanical alloying in the form of nanoscale nitrogen-rich dispersoids [2, 4, 20]. These nitrogen-rich dispersoids have been shown to help limit grain growth during thermal and thermo-mechanical treatment by pinning the grain boundaries [2, 21]. A study by Hashemi-Sadraei et al. found that the cryomilled Al grains only grew up to ~60 nm after heat treating an 8 hr cryomilled AA5083 powder at 500°C for 24 hours [21]. However, since 100 nm is commonly considered the 'upper-limit' of the nanocrystalline regime, the Hall-Petch strengthening will be calculated for grain sizes between 20 and 100 nm.

In order to distinguish between solid solution strengthening and strengthening from the grain structure, the friction stress term from the Hall-Petch equation was removed for this study:

$$\sigma_{HP} = k_{HP}\left(d_{Al}\right)^{-1/2} \tag{2.2}$$

As discussed in section 2.1, the Hall-Petch coefficient for AA5083 varies depending on the exact composition of the alloy from 0.16 – 0.17 MPa·$m^{1/2}$. Figure 4 is the resultant Hall-Petch strength if the grain size is varied from 20 to 100 nm. The open boxes illustrate what the strengthening contribution would be if the Hall-Petch coefficient corresponding to the lower Mg limit of AA5083 (4.0 wt.% Mg) was chosen and filled diamonds if the upper limit of 4.9 wt.% Mg is used. These two lines illustrate the range of Hall-Petch strengthening as a result of adjusting the Mg content in the alloy. From these two curves, it can be noted that the effect of Mg alloying allowed for in the AA5083 does not significantly affect the Hall-Petch-type strengthening. However, the effect of grain size on the strength is obvious since σ_{HP} more than triples when the grain size is 20 versus 100 nm.

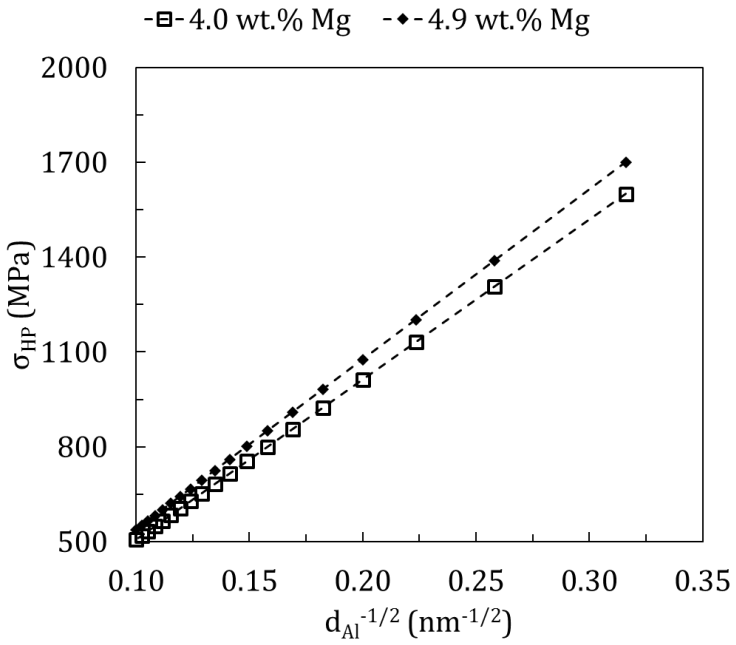

Figure 4: Calculated Hall-Petch strengthening as a function of grain size, d_{Al}, and Mg alloying content. The open squares represent the Hall-Petch strength calculated from the k_{HP} based on alloying with 4.0 wt.% Mg and the filled diamonds represent the strength based on alloying with 4.9 wt.% Mg.

2.3 Dislocation Forest Strengthening

As discussed in the previous section, dislocations are produced during the mechanical attrition of the powders. In addition, milling at cryogenic temperatures limits recovery processes and helps retain the high dislocation density. However, dislocations will anneal out during thermal treatments such as degassing. Therefore, the parameters chosen for degassing will need to be chosen so as to minimize the effect on the dislocation density.

The dislocation density, ρ, is equal to 10^{10} – 10^{12} m^{-2} for a well-annealed metal and ρ is 10^{14} – 10^{15} m^{-2} for a heavily cold-rolled metal [22]. For the case of a cryomilled material, Zhou et al. analyzed the dislocation density of an Al-7.6 at.% Mg binary alloy cryomilled for 8 hours using high resolution transmission electron microscopy and found that the larger crystals (~20 nm diameter) had a dislocation density of $1.3 \cdot 10^{17}$ m^{-2} but estimated that the overall dislocation density was only $5 \cdot 10^{16}$ m^{-2} [8]. In this parametric study, the potential range of strengthening for a cryomilled AA5083 powder due to the presence of dislocations in the material was calculated based on a dislocation density varied from 10^{10} to 10^{17} m^{-2}.

The strengthening from the presence of dislocations can be described by the dislocation forest strengthening equation also sometimes referred to as the Taylor equation [23-26]:

$$\sigma_f = \alpha G b M \rho^{1/2} \tag{2.3}$$

where ρ is the dislocation density, G is the shear modulus which is equal to 25.9 GPa for Al [27], b is the burgers vector of Al which is 0.286 nm [27], α and M are constants equal to 0.3 and 2.7 respectively [24]. Using equation (2.3), the dislocation forest strengthening was

calculated as a function of dislocation density and is plotted in Figure 5. Up until $\rho \sim 10^{14}$ m^{-2} the dislocation forest strengthening is roughly zero. Beyond $\rho \sim 10^{14}$ m^{-2} the dislocation forest strengthening increases dramatically up to ~ 1900 MPa for a dislocation density of 10^{17} m^{-2}.

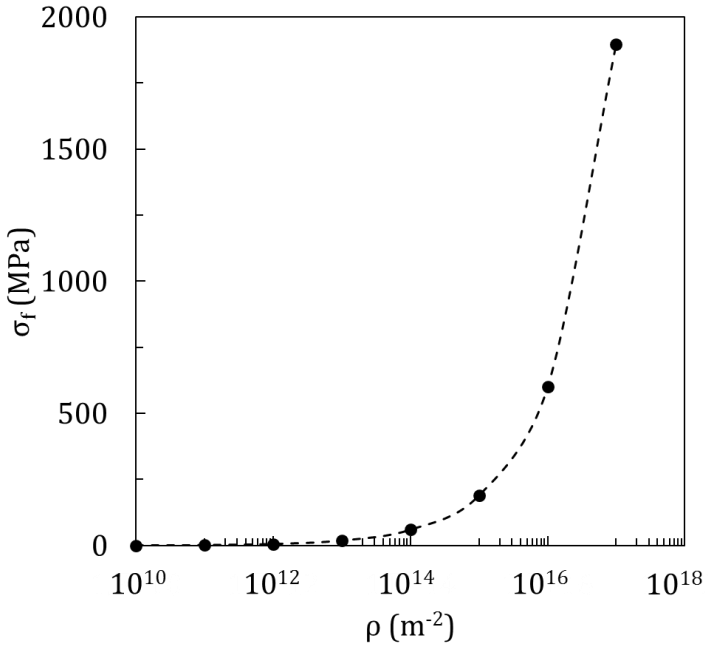

Figure 5: Dislocation forest strengthening as a function of dislocation density.

2.4 Orowan Strengthening

Small dispersoids present in the material can hinder dislocation motion. If we consider a pair of dispersoids spaced λ apart, a dislocation impinging upon these two dispersoids will be unable to pass the barrier. If the stress is increased, the dislocation will begin to bend around the dispersoids until it meets itself on the other side of the dispersoid. This section of the dislocation annihilates allowing the rest of the dislocation to

continue moving through the lattice leaving behind a dislocation loop around the dispersoid. This mode of increasing the inherent strength of the material is called Orowan strengthening and is generally considered as a viable means to increase the strength of a material without loss to ductility.

Orowan strengthening is described by the Orowan-Ashby equation [17]:

$$\sigma_{OS} = \frac{0.13Gb}{\lambda} \ln \frac{d_{OS}}{2b} \tag{2.4}$$

where σ_{OS} is the incremental increase in strengthening due to the Orowan mechanism, G is the aluminum shear modulus, b is the Burgers vector, λ is the interparticle spacing and d_{OS} is the diameter of the dispersoids. The interparticle spacing, λ, can be determined using the volume fraction, F, and diameter, d_{OS} of the dispersoids [17]:

$$\lambda = \frac{2(1-F)d_{OS}}{3F} \tag{2.5}$$

Using these two equations, the strengthening contribution from various dispersoids found within the cryomilled AA5083 material were estimated.

2.4.1 Large Dispersoids

Dispersoid phases observed to form in cryomilled AA5083 are $Al_6(MnFeCr)$, $Al_{12}(FeMn)_3Si$, $Al_{12}Mg_2$, and Mg_2Si [28]. The most common of these is $Al_6(MnFeCr)$ and is typically 100 nm – 1 μm in diameter [28]. The Al_6Mn dispersoid in particular has been

hailed as an effective means to strengthen the aluminum alloy through Orowan strengthening [13]. This study will estimate the Orowan strengthening contribution from the presence of Al_6(MnFeCr) dispersoids and determine its significance for strengthening nanocrystalline AA5083.

Table 2: AA5083 alloy composition ranges in weight and atomic percent for each element present in the alloy.

AA5083	Si	Fe	Cu	Mn	Mg	Cr	Zn	Ti	Al
wt.% [29]	0.4-0.7	0.4	0.1	0.4-1.0	4.0-4.9	0.05-0.25	0.25	0.15	Bal
at. %	0.4-0.7	0.2	0.04	0.2-0.5	4.5-5.5	0.03-0.13	0.10	0.08-0.09	Bal

In order to calculate Orowan strengthening with equations (2.4) and (2.5), it will be necessary to determine the volume fraction of Al_6(MnFeCr) dispersoid in the alloy. The weight and atomic percent of each element in the AA5083 alloy is provided in Table 2. If all of the Mn, Fe and Cr present in the alloy is used to form the Al_6(MnFeCr) phase, then there is Fe (at.%) + Mn (at.%) + Cr (at.%) = 0.42 – 0.82 at.% (MnFeCr) available to form Al_6(MnFeCr). According to stoichiometry, every one mole of (MnFeCr) atoms ties up 6 mol of Al atoms. Therefore, 2.5 – 4.9 at.% Al or 2.3 – 4.4 wt.% Al is tied up as Al_6(MnFeCr). The weight percent of Al_6(MnFeCr) is simply the sum of the wt.% of each constituent, i.e. Fe (wt.%) + Mn (wt.%) + Cr (wt.%) + Al (wt.% in dispersoid) = 3.1 – 6.1 wt.% Al_6(MnFeCr) in the AA5083 alloy. The volume percent of Al_6(MnFeCr) can be calculated by:

$$vol.\%Al_6(MnFeCr) = \frac{w_{Al_6(MnFeCr)} / \rho_{Al_6(MnFeCr)}}{w_{Al_6(MnFeCr)} / \rho_{Al_6Mn} + \left(100 - w_{Al_6(MnFeCr)}\right) / \rho_{AA5083}} \cdot 100\% \qquad (2.6)$$

where $w_{Al6(MnFeCr)}$ is the weight percent of $Al_6(MnFeCr)$ in the alloy, ρ_{Al6Mn} is the density of Al_6Mn which is equal to 3.32 $g \cdot cm^{-3}$ [30] and ρ_{AA5083} is the density of AA5083 which is 2.66 $g \cdot cm^{-3}$. The volume percent of $Al_6(MnFeCr)$ was calculated as 2.5 – 4.9 vol.%. Using this value and the size of the dispersoids 100 nm – 1 μm, the Orowan strengthening contribution from these dispersoids was calculated according to equations (2.4) and (2.5).

In order to visualize the effect of varying these two parameters, the strengthening contribution from these dispersoids, σ_{Orowan}, was calculated by fixing one or the other parameter. Figure 6a demonstrates the change in Orowan strengthening as a function of dispersoid diameter at several fixed volume percent, and in Figure 6b the change in Orowan strengthening with varying volume percent at a fixed dispersoid diameter is presented. The σ_{Orowan} increases with higher volume percent of the dispersoid. However, the change in strength due to the volume fraction is small compared to the effect of dispersoid diameter. This can clearly be seen in Figure 6b, where although the difference in strengthening between a dispersoid size of 1000 nm and 500 nm is small, reducing the dispersoid size to 100 nm more than doubles the strengthening contribution. In general, σ_{orowan} increases as the dispersoid size decreases and the volume fraction increases. Regardless, the overall contribution to strength from the $Al_6(MnFeCr)$ dispersoid is small (<4 MPa) and therefore is not a viable means to strengthen the material. Additionally, it is within reason that the other large dispersoid phases present in the material, which are of similar size and volume fraction, are also unlikely to significantly contribute towards the overall strength of the material.

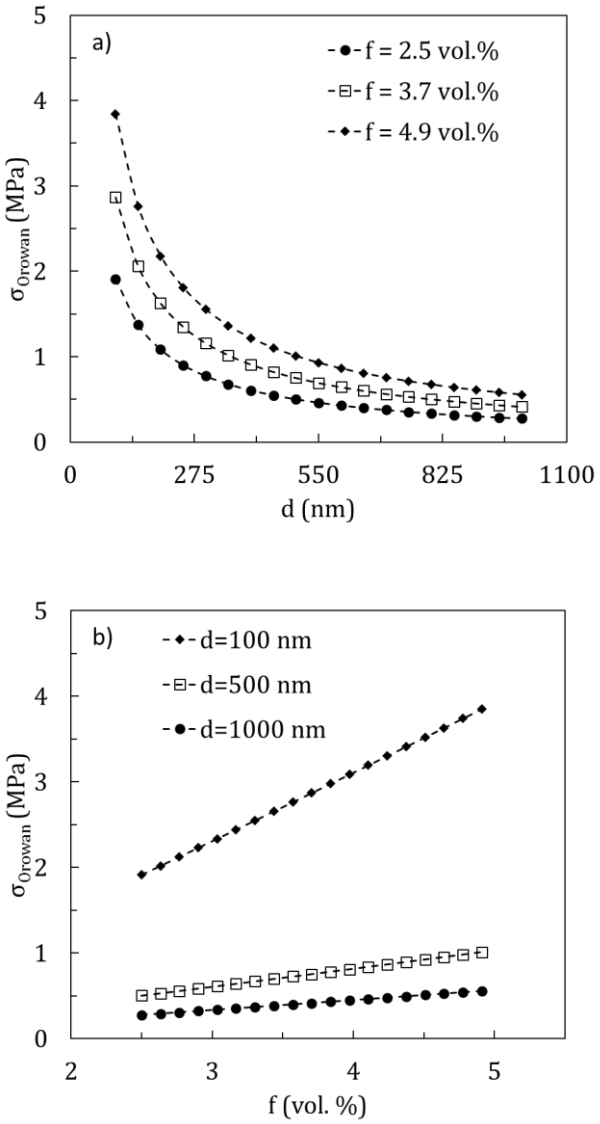

Figure 6: Orowan strengthening from the $Al_6(MnFeCr)$ dispersoid; a) Orowan strengthening as a function of dispersoid diameter at fixed volume percent; b) Orowan strengthening as a function of volume percent at fixed dispersoid diameter.

2.4.2 Fine Dispersoids

Several types of fine dispersoids have been found in cryomilled aluminum and aluminum composites including nanoscale aluminum carbide, aluminum oxide, aluminum nitride and amorphous domains rich in nitrogen, oxygen and carbon [2, 4, 5, 10]. The

dispersoids are typically 3 – 15 nm in diameter and are frequently found within the nanoscale aluminum grain boundaries [2]. These dispersoids provide Orowan strengthening and serve to pin the small aluminum grains during thermal and thermo-mechanical treatment thus retaining strength.

2.4.2.1 Carbide Dispersoids

Aluminum carbide, Al_4C_3, forms as a result of mechanical alloying between the carbon-rich process control agent (PCA) and the aluminum powder [10]. A PCA is used in order to prevent excessive agglomeration of the aluminum powder during mechanical attrition. Several examples of PCA used in mechanical milling or cryomilling of aluminum and aluminum alloys are:

- Methanol, CH_3OH (37 wt.% C) [3, 31]
- Caprylic Acid, $C_8H_{16}O_2$ (67 wt.% C) [32]
- Stearic Acid, $C_{18}H_{36}O_2$ (76 wt.% C) [3, 31, 32]
- Oleic Acid, $C_{18}H_{34}O_2$ (77 wt.% C) [32]
- Nopcowax 22-DS, $C_{38}H_{76}N_2O_2$ (77 wt.% C) [10]
- Graphite, C (100 wt.% C) [33]

Typically, 0.12 – 2 wt.% PCA is added to the aluminum for milling. Although many different types of PCA exist, for simplicity, a graphite PCA was assumed. It was also assumed that all of the carbon added to the system will react with aluminum to form Al_4C_3. The composition of the AA5083 alloy with the added graphite content is provided in Table 3 in both weight percent and atomic percent. The atomic percent of each element in the modified powder was calculated using:

$$at.\%A = \frac{w_A / A_A}{\sum_n w_n / A_n} \cdot 100\% \quad (2.7)$$

where w_n is the weight percent of element n, and A_n is the atomic mass of element n.

Table 3: Composition of AA5083 after adding a graphite PCA

AA5083 + graphite	C	Si	Fe	Cu	Mn	Mg	Cr	Zn	Ti	Al
wt.%	0.12 – 2.00	0.4 - 0.7	0.4	0.1	0.4 – 1.0	3.9 - 4.9	0.05 - 0.25	0.25	0.15	Bal
at.%	0.27-4.32	0.4-0.7	0.2	0.04	0.2-0.5	4.2-5.5	0.02-0.13	0.10	0.08	Bal

From Table 3, there is 0.27 – 4.32 at.% C available to form Al_4C_3. According to stoichiometry, every 3 mol of C atoms ties up 4 mol of Al atoms to form Al_4C_3. Therefore, 0.36 – 5.76 at.% Al is used to form Al_4C_3. The weight percent of Al as Al_4C_3 can be described by:

$$wt.\%Al\left(Al_4C_3\right) = \frac{a_{Al} \cdot A_{Al}}{\sum_n a_n \cdot A_n} \quad (2.8)$$

where a_{Al} is the atomic percent of Al as Al_4C_3, A_{Al} is the atomic mass of Al and the summation in the denominator is of the atomic percent of each element in the alloy multiplied by its respective atomic mass. From this equation, 0.36 – 5.87 wt.% Al is used to form Al_4C_3. The total weight percent of Al_4C_3 in the alloy is C(wt.%) + Al(wt.% in Al_4C_3) =

0.48 – 7.87 wt.%. A modified version of equation (2.6) can be used to determine the volume percent of Al_4C_3 from the weight percent:

$$vol.\%Al_4C_3 = \frac{w_{Al_4C_3} / \rho_{Al_4C_3}}{w_{Al_4C_3} / \rho_{Al_4C_3} + \left(100 - w_{Al_4C_3}\right) / \rho_{AA5083}} \cdot 100\% \quad (2.9)$$

where ρ_{AA5083} is the density of AA5083 equal to 2.66 g·cm^{-3} and ρ_{Al4C3} is the density of Al_4C_3 and is 2.98 g·cm^{-3} [34]. From this equation, the volume percent of Al_4C_3 in the alloy is 0.4 – 7.1 vol.%.

2.4.2.2 Oxide Dispersoids

Gas atomized aluminum powders are typically spherical and have a naturally occurring oxide scale consisting of aluminum oxides and hydroxides typically 2 – 15 nm thick [6, 35, 36]. During cryomilling, this oxide layer is broken up into fine 3 – 15 nm diameter dispersoids [2]. Ideally, because the powder is submerged in liquid nitrogen, no further oxidation should occur during the cryomilling process. But, since oxidation of aluminum is roughly instantaneous, as soon as the AA5083 powders are removed from the cryomill the powders will form a new surface oxide layer even in an atmosphere controlled glovebox. Therefore, measuring the oxide content in the cryomilled powder will not be relatable to the volume fraction of nanoscale oxide dispersoids needed to determine Orowan strengthening. Instead the volume fraction of oxide dispersoids was estimated from the calculated volume fraction of the original surface oxide of the as-atomized AA5083 powders based on the thickness of the oxide scale and particle size.

In order to estimate the Orowan strengthening contribution from the presence of nanoscale oxide dispersoids, several assumptions were made: 1) the surface oxide layer of the original, gas atomized aluminum powder consists of a uniform layer of Al_2O_3, 2) the original surface oxide layer of the powder is completely broken up during cryomilling and redistributed throughout the bulk of the powder particle and 3) no additional oxidation occurs during cryomilling. The volume fraction of the nanoscale oxide dispersoids is simply the volume fraction of the oxide layer of the as-atomized powders before cryomilling. The absolute volume of oxide, V_{oxide}, can be estimated knowing the thickness, t, of the oxide layer and the diameter of the powder particle, d_2:

$$V_{oxide} = V_{particle} - V_{aluminum} = \frac{1}{6}\pi\left(d_2^e - d_1^e\right) \tag{2.10}$$

where d_1 is the diameter of the aluminum part of the powder particle without the oxide shell and can be described in terms of the oxide thickness, t:

$$d_1 = d_2 - 2t \tag{2.11}$$

The volume fraction of oxide, F, is simply the volume of the oxide, V_{oxide}, divided by the total volume of the particle:

$$F = \frac{\frac{1}{6}\pi\left(d_2^3 - d_1^3\right)}{\frac{1}{6}\pi d_2^3} = 1 - \frac{d_1^3}{d_2^3} \tag{2.12}$$

Combining equations (2.11) and (2.12), F can be written in terms of only t and d_2:

$$F = 1 - \frac{(d_2 - 2t)^3}{d_2^3} \tag{2.13}$$

These parameters are demonstrated schematically in Figure 7. Use of this equation requires particle size analysis on the as-atomized powders.

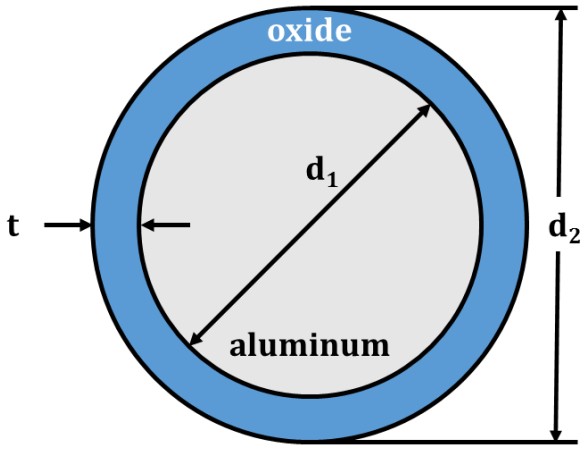

Figure 7: Schematic of aluminum powder particle of diameter d_2, with oxide scale of thickness, t, and inner core aluminum particle of diameter, d_1.

Particle size analysis was conducted on as-atomized AA5083 powders used in this study with a Beckman Coulter LS 13 320 particle size analyzer. The average particle diameter was 13 μm with the majority of the particles in the range of 2.5 – 27 μm. The volume fraction of aluminum oxide was calculated from equation (2.13) and the range was $4.4 \cdot 10^{-4}$ – $3.6 \cdot 10^{-2}$ which is equal to 0.044 – 3.60 vol.%.

2.4.2.3 Nitride Dispersoids

Nitrogen-rich dispersoids form as a result of mechanical alloying of the AA5083 powder with the surrounding liquid nitrogen during the cryomilling process. Nitrogen-rich dispersoids have been found in the form of AlN and amorphous regions rich in nitrogen [2, 4]. The remarkable grain size stability of cryomilled aluminum is attributed to these dispersoids which are frequently located in the grain boundaries of the nanocrystalline aluminum [2, 21].

Previously, Hofmeister et al. conducted a study to determine the amount of nitrogen mechanically alloyed as a function of cryomilling time up to 72 hours milling time [33]. Nitrogen concentration was measured by secondary ion mass spectrometry and quantified using a ^{14}N ion implanted standard. In general, it was found that the nitrogen concentration in the aluminum increased with cryomilling time up to 72 hours without saturation. Nitrogen concentration varied from 0.80 ± 0.08 wt.% for an 8 hr cryomilled AA5083 to 13.17 ± 0.71 wt.% after cryomilling for 72 hours [33]. Assuming that all nitrogen in the system formed AlN or an amorphous dispersoid of equivalent density, the volume fraction of nitrogen was calculated as $9.55 \cdot 10^{-3} \pm 0.96 \cdot 10^{-3}$. Although higher volume fractions of nanoscale nitrides could be formed with a longer cryomilling time, for practical reasons this study limited the cryomilling time to 8 hours such that it could be completed within a typical work day thus minimizing cost from consumables and labor.

2.4.2.4 Fine Dispersoid Strengthening

If all the nanoscale dispersoids are evenly distributed throughout the bulk and are of similar size (3 – 15 nm), dislocations traveling through the bulk will interact with all the nanoscale dispersoids similarly regardless of their specific composition. Therefore, the

Orowan strengthening from the presence of these nanoscale dispersoids was calculated based on the sum of the respective volume fractions of the carbide, oxide and nitride dispersoids which was $1.3 \cdot 10^{-2}$ – $11.7 \cdot 10^{-2}$. The Orowan strengthening contribution from the combined presence of all the fine, nanoscale dispersoids, σ_{nano}, was calculated from equations (2.4) and (2.5). The strengthening contribution is plotted in Figure 8a and 8b where Figure 8a is σ_{nano} as a function of dispersoid diameter at constant volume percent and Figure 8b is σ_{nano} as a function of volume percent with fixed dispersoid diameter. The Orowan strengthening increased as the volume percent of dispersoid increased and the dispersoid diameter decreased. The Orowan strengthening from the fine, nanoscale dispersoids ranged from 4 – 106 MPa.

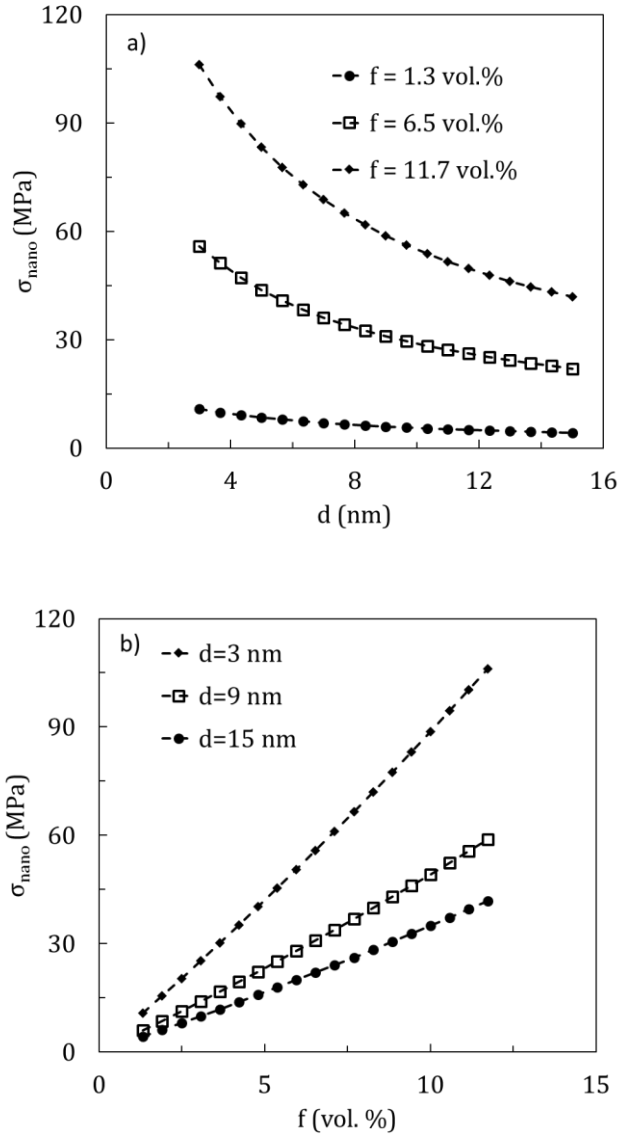

Figure 8: Orowan strengthening resulting from nanoscale dispersoids; a) change in σ_{nano} as a function of dispersoid diameter and fixed volume percent; b) change in σ_{nano} as a function of volume percent with fixed dispersoid diameter.

2.5 Summary

From this study, several observations have been made:

1. AA5059 has the highest Mg alloying content in the Al 5000 series alloys (5.0 – 6.0 wt.%) and therefore, this alloy should exhibit the highest solid solution

strengthening. However, in this study, AA5083 (4.0 – 4.9 wt.% Mg) was chosen due to alloy cost and the availability of existing literature on the alloy.

2. Hall-Petch strengthening is one of the predominant strengthening mechanisms for nanocrystalline materials. In this study, the Hall-Petch strengthening contribution was calculated to be up to 1700 MPa. Therefore, preserving the fine grain size even after themo-mechanical treatment is of paramount importance to retaining the high strength of this material.
3. Defects such as dislocations are formed in the material as a result of the cryomilling process. Dislocation forest strengthening has been estimated and found to vary from 0 to ~1900 MPa for dislocation densities varying from 10^{10} – 10^{17} m^{-2}. Since dislocations could potentially anneal out during the degassing process, the effect of degassing on the dislocation density will need to be determined in order to optimize the strength of this material.
4. Both large and fine dispersoids contribute to the overall strengthening, but the magnitude of that contribution is small due to either the large dispersoid diameter and/or the small volume fraction present in the material. The fine dispersoids provide small to moderate strengthening to the material. In addition to strengthening, the fine dispersoids serve to pin the aluminum grain boundaries thus retaining the nanocrystalline grain size and Hall-Petch strength.

A summary of the parameters and calculated strength for each of the strengthening mechanisms is provided in Table 4. As can be seen from Table 4, both the Hall-Petch and dislocation forest strengthening could potentially play a large role in the high strength

exhibited in cryomilled materials. Solid solution strengthening and Orowan strengthening provide a small to moderate contribution to the overall strength.

Table 4: Summary of strengthening mechanisms in cryomilled AA5083, the respective input parameters and the calculated increase of strength in MPa

Strengthening Mechanism	**Parameter 1**	**Parameter 2**	**σ (MPa)**
Solid Solution + Inherent Strength, σ_o	Mg (wt.%) = 4.0 – 4.9	-	78 – 94
Hall-Petch, σ_{HP}	Mg (wt.%) = 4.0 – 4.9	Al grain size = 20 – 100 nm	506 – 1700
Dislocation Forest, σ_f	$\rho = 10^{10} – 10^{17}$ m^{-2}	-	0 – 1900
Orowan – Al_6Mn, σ_{Orowan}	Fe (wt.%) = 0.4 Mn (wt.%) = 0.4 – 1.0 Cr (wt.%) = 0.05 – 0.25	d = 100 – 1000 nm	0.3 – 3.8
Orowan – Al_4C_3, $\sigma_{carbides}$	C (wt.%) = 0.12 - 2	d = 3 – 15 nm	4.2 – 106
Orowan – Al_2O_3, σ_{oxides}	oxide thickness, = 2 – 15 nm	d_2 = 2.47 – 27.3 μm	
Orowan – AlN, $\sigma_{nitrides}$	F = f(cryomilling time)	d = 3 – 15 nm	

CHAPTER 3: EXPERIMENTAL

3.1 Manufacturing Methodology

Gas atomized AA5083 powder (0.4 wt.% Mn; 4.5 wt.% Mg; minor Si, Fe, Cu, Cr, Zn, Ti; balance Al) produced by Valimet Inc was cryomilled in a Union Process 1-S attritor mill modified to allow for the continuous flow of liquid nitrogen. The AA5083 powder was cryomilled in the presence of liquid nitrogen for 8 hours using 440C stainless steel balls at a 32:1 ball to powder ratio. In order to minimize agglomeration, a graphite process control agent (Alfa Aesar, 0.15 wt.%) was V-blended with the AA5083 powder before milling. In addition, the attritor was surrounded by a liquid nitrogen-cooled jacket to ensure temperature stabilization. The powder was sieved after cryomilling with a -325 mesh sieve to remove any excessively large agglomerates.

A custom static vacuum degasser, located at Army Research Laboratory in Aberdeen Proving Ground, MD, was used to degas the powders. Powders were poured into a metallic canister and sealed inside a glove box to prevent atmospheric contamination. The canister was placed into a heater sleeve and connected to the vacuum system to draw off volatiles and minimize oxidation. The canister was slowly evacuated until the vacuum held steady at or below 6.5×10^{-3} Pa. The degassing temperatures in this study were chosen based on a differential scanning calorimetry (DSC) work conducted by Tellkamp et al. [37] such that the powders were degassed at temperatures between the major transitions observed in the DSC spectrum. An additional powder was degassed at 300°C after the start of the study to help explain a sharp transition in the hydrogen concentration. The powder was degassed at 200°C, 300°C, 350°C, 410°C, or 500°C with a ramp rate of 68.3°C/hr and a soak time of 8

hours at about 2.7 x 10^{-3} Pa. The ramp rate is based on the typical ramp of 6 hours for degassing at 410°C of a commercially processed powder.

3.2 Microstructural Characterization and Spectroscopy

In order to observe the microstructure, powders were dispersed in epoxy and metallographically polished down to 0.02 μm with colloidal silica as the final polish. A Zeiss Ultra-55 field emission Scanning Electron Microscope (SEM) working at 10 kV was used to examine the microstructures of the powders. The dispersoid size and volume fraction in the powders was examined via backscatter electron microscopy (BSE). A Pananalytical MRD Pro X-ray Diffraction (XRD) system was used to calculate the grain size and identify dispersoids in the powder. The grain size of the powders was calculated by Rietveld analysis with a Pseudo Voigt profile function and a polynomial background fit of the XRD spectrum.

In order to prepare the thin foils for transmission electron microscopy (TEM), a FEI 200 TEM Focused Ion Beam using an in situ lift out technique (FIB-INLO) was used. Powders were first sprinkled onto carbon tape and placed inside the FIB. Platinum was deposited on top of the powder surface and material was removed on either side. A foil was cut out from the powder leaving only a thin bridge connecting the foil from the parent powder (see Figure 9). A microprobe was inserted into the chamber and attached to the foil using platinum. The thin foil was then cut free from the powder and removed. The thin foil was then attached to a TEM grid with platinum and thinned down to electron transparency.

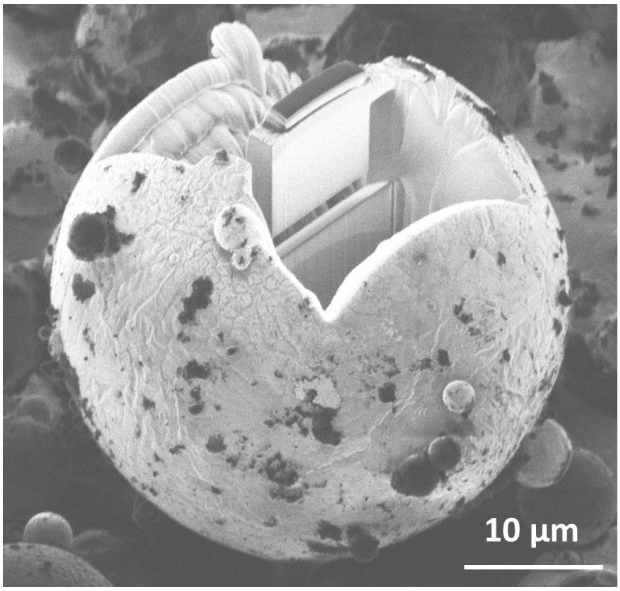

Figure 9: Preparation of a TEM thin foil from a powder sample via the FIB-INLO technique. This micrograph is of a thin foil cut from a gas atomized Mg WE43 powder

Transmission electron microscopy (TEM) was conducted with a FEI Tecnai F30 TEM operating at 300 kV equipped with X-ray Energy Dispersive Spectroscopy (XEDS) and a High Angle Annular Dark Field (HAADF) detector. Bright field TEM (BF TEM) images were used for grain size analysis. Chemical analysis was conducted using a LECO 836 OHN inert gas fusion infrared and thermal conductivity detection unit to measure the hydrogen, oxygen and nitrogen impurity concentrations.

3.3 Grain Size Analysis

For a nanocrystalline material, it is difficult to produce TEM foils thin enough for a single layer of grains, therefore grain overlapping is inevitable. The overlapping of the grains and complexities such as dislocations and other defects makes computer-aided analysis based on the pixel brightness difficult. Therefore, manual tracing of the grains is the preferred method of grain size analysis. Figure 10a is an example of a BF TEM

micrograph of the Al powder cryomilled for 8 hours. Each BF TEM micrograph was enlarged and printed. A plastic transparency was placed over the micrograph and the grain boundaries observed in the BF TEM micrograph were traced. The transparency was scanned to form a digital image. The grain boundaries in Figure 10a were traced and the resulting image is Figure 10b.

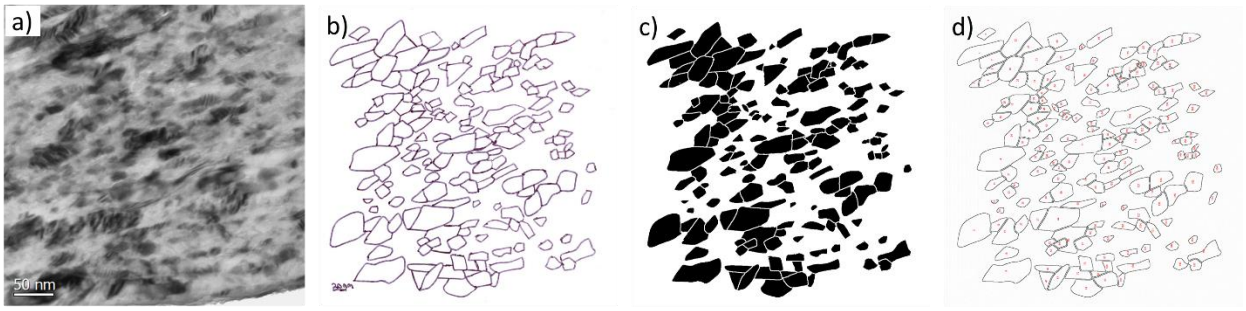

Figure 10: The process of grain size analysis by manual tracing: a) BF TEM micrograph, b) the grain boundaries in the BF TEM micrograph in a) have been traced and scanned, c) The image has been digitally manipulated such thats the grains are of black contrast and may now be quantified using the analyze particles tool, and d) the outlines of each grain quantified from c)

ImageJ™ software was used to process the image [38]. The threshold tool isolated the grain boundaries from any noise picked up from the scan. Occasionally a broken grain boundary would be found in the scanned image and the brush tool was used to connect it. The skeletonize tool reduced the grain boundary width to 1 pixel, thus removing any variations in the grain boundary thickness created during tracing. Then the dilate tool was used to expand the grain boundary thickness to 3 pixels in width. The background of the image was then colored black with the paint tool. The image was inverted (see Figure 10c) creating black colored grains. The grains were then quantified using the analyze particles tool. After the analysis was complete, the grains were checked to make sure they were

counted correctly by inspecting the outlines of the grains (see Figure 10d). The areas of each grain were measured and the equivalent circular diameter was calculated as the grain size. A minimum of 200 grains were counted for to determine the average grain size and distribution for each powder examined in this study.

3.4 Dispersoid Quantification

Dispersoids form from the cryomill-induced supersaturated solid solution powders when the powders are heated above a critical temperature. In backscatter SEM, these dispersoids appear with a bright contrast as compared to the aluminum matrix (see Figure 11a). The BSE SEM micrographs were also analyzed using the ImageJ™ software [38]. In order to calculate the size of the dispersoids, the threshold tool was used to isolate the dispersoids from the aluminum matrix by pixel brightness. Once isolated, the analyze particles tool was used to calculate the areas of each dispersoid (see Figure 11b). The equivalent circular diameter was calculated for each dispersoid, and the average and standard deviation of each powder is reported.

Figure 11: Dispersoid quantification through image analysis: a) BSE micrograph, b) dispersoids quantified from micrograph a), and c) outline of the area occupied by the powder agglomerate in micrograph a)

The volume fraction of dispersoids was also calculated for each powder sample. Because the powder agglomerates are small, epoxy was often imaged with a black contrast in the BSE micrographs. In order to determine the volume fraction of dispersoids, it was necessary to measure the area of the micrograph occupied by the aluminum agglomerate. The threshold tool was used to select the regions occupied by both the aluminum matrix and the brighter dispersoids. The agglomerate area measured from Figure 11a is illustrated by the outline in Figure 11c. The volume fraction of the dispersoids in the powder was simply the total area of the dispersoids divided by the area of the aluminum agglomerate. Dispersoid size and volume fraction was measured from three random agglomerates for each powder sample.

CHAPTER 4: MICROSTRUCTURAL EVOLUTION WITH DEGASSING TEMPERATURE

Previously, there has not been a comprehensive study on the evolution of the microstructure and chemistry of cryomilled aluminum powders degassed isothermally and examined in the as-degassed condition. The objective of this study was to determine the effect of degassing temperature on the microstructure and chemistry of cryomilled nanocrystalline AA5083, specifically: the formation and growth of dispersoids, evolution of grain size, annealing of dislocations and the removal of impurities which are key to the ultra-high strength of the material [2]. This information can be used to optimize the degassing conditions for a cryomilled AA5083 powder.

4.1 Grain Growth

During degassing, the powders are subjected to a thermal treatment resulting in grain growth. In order to determine the extent of grain growth occurring as a result of degassing, XRD was initially used to determine the grain size as a function of degassing temperature. The XRD profiles of samples examined in this study are presented in Figure 12. The predominant phase is FCC Aluminum in all profiles. The peaks are broadened indicating that a nanocrystalline structure is retained even at the highest degassing temperature of 500°C. Grain size and microstrain calculated for each powder are summarized in Table 5.

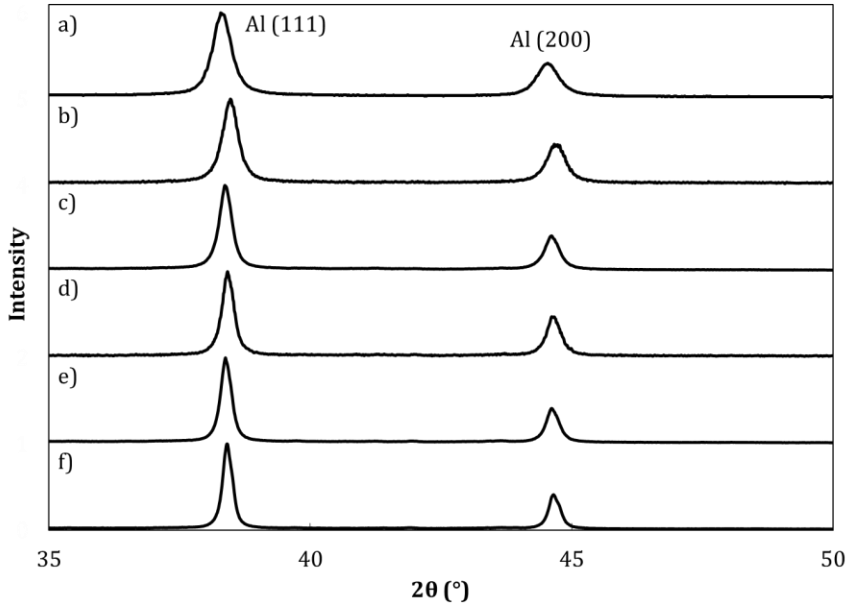

Figure 12: XRD profile of cryomilled and degassed AA5083 powders. XRD indicates that the primary phase present in the cryomilled powders is Al regardless of degassing temperature. XRD profiles are provided for a) as-cryomilled, and degassed at b) 200°C, c) 300°C, d) 350°C, e) 410°C, and f) 500°C.

For comparison, the grain size was also measured directly by TEM. Representative BFTEM images for each sample are provided in Figure 13. More than 200 grains were counted for each degassing temperature. The grain size calculated by TEM is reported in Table 5. Some elongation of the grains was observed in the as-cryomilled powders as shown in Figure 13a, but, after degassing at 200°C, the grains became equiaxed as presented in Figure 13b. Figures 13a through 13c illustrate that the grain size was relatively stable for powders degassed up to 300°C. However, degassing at or above 350°C resulted in a noticeable grain growth as presented in Figures 13d through 13f.

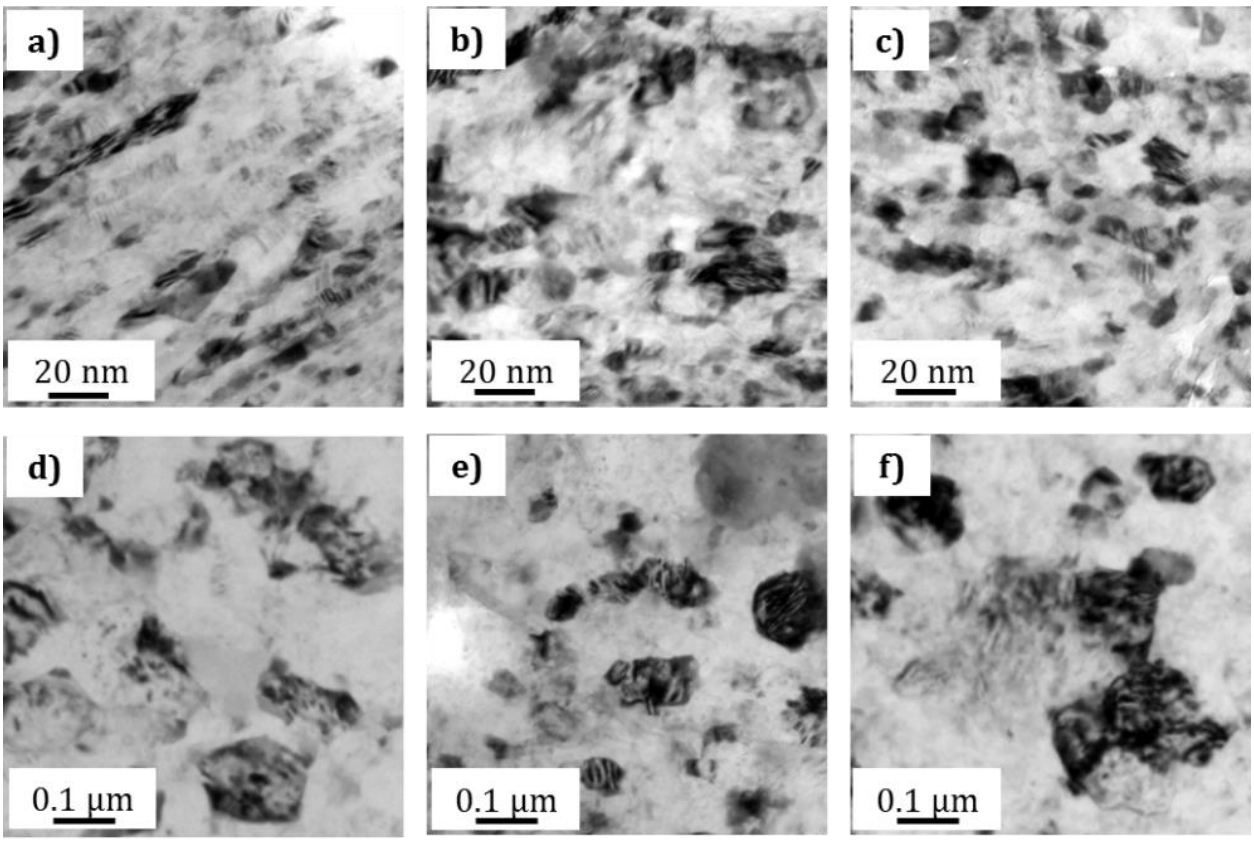

Figure 13: Representative BFTEM micrographs used to measure the grain size of the nanocrystalline Al grains: a) as-cryomilled, degassed at b) 200°C, c) 300°C, d) 350°C, e) 410°C, and f) 500°C.

Table 5: Comparison of grain size measured by XRD and TEM

	XRD Grain Size (nm)	XRD Microstrain (%)	TEM Grain Size				
			Mean (nm)	Standard Deviation (nm)	Standard Error (nm)	95% Confidence Interval	Number of Grains Counted
As-cryomilled	34	0.31	20.7	9.5	0.4	(19.9, 21.5)	585
200°C degassed	36	0.21	25.1	14.2	0.5	(24.0, 26.1)	716
300°C degassed	51	0.16	27.2	14.2	0.8	(25.7, 28.8)	334
350°C degassed	53	0.13	56.8	35.1	2.2	(52.5, 61.2)	249
410°C degassed	63	0.13	45.1	24.5	1.5	(42.2, 48.1)	263
500°C degassed	79	0.10	69.2	43.7	2.3	(64.7, 73.8)	353

The evolution of grain size is presented as a function of degassing temperature in Figure 14. The as-cryomilled sample is represented by plotting as room temperature (25°C) degassing. Grain size measured by both TEM (filled circles) and XRD (open squares) are similar and increase with degassing temperature. The majority of the average grain sizes calculated by XRD are within the standard deviation measured by TEM. A significant increase in grain size standard deviation can be seen for samples degassed at temperatures at or above 350°C.

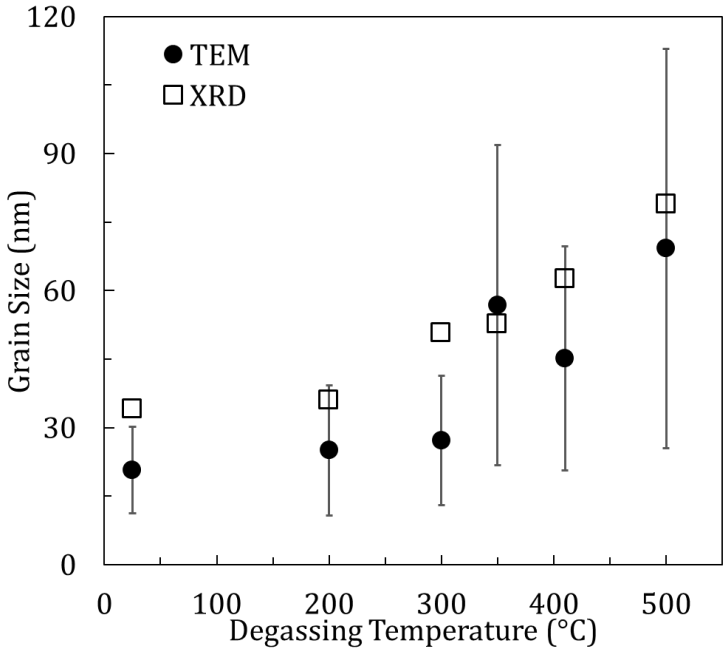

Figure 14: Grain size (both XRD and TEM) increases with degassing temperature. The TEM grain size standard deviation increases significantly after degassing at temperatures at or higher than 350°C.

Histograms of the grain size measurement of all the samples are presented in Figure 15 in order to explore the increase in standard deviation. The as-cryomilled powder and the powders degassed at 200°C and 300°C, presented in Figures 15a, 15b and 15c

respectively, have relatively narrow distributions in grain size. However, after degassing at temperatures at or above 350°C, as shown in Figures 15d, 15e and 15f, the distribution spreads towards the larger grain sizes. The majority of the grains are still in the 30-60 nm range, however the presence of a few abnormally large grains shifts the average to a larger grain size and increases the standard deviation.

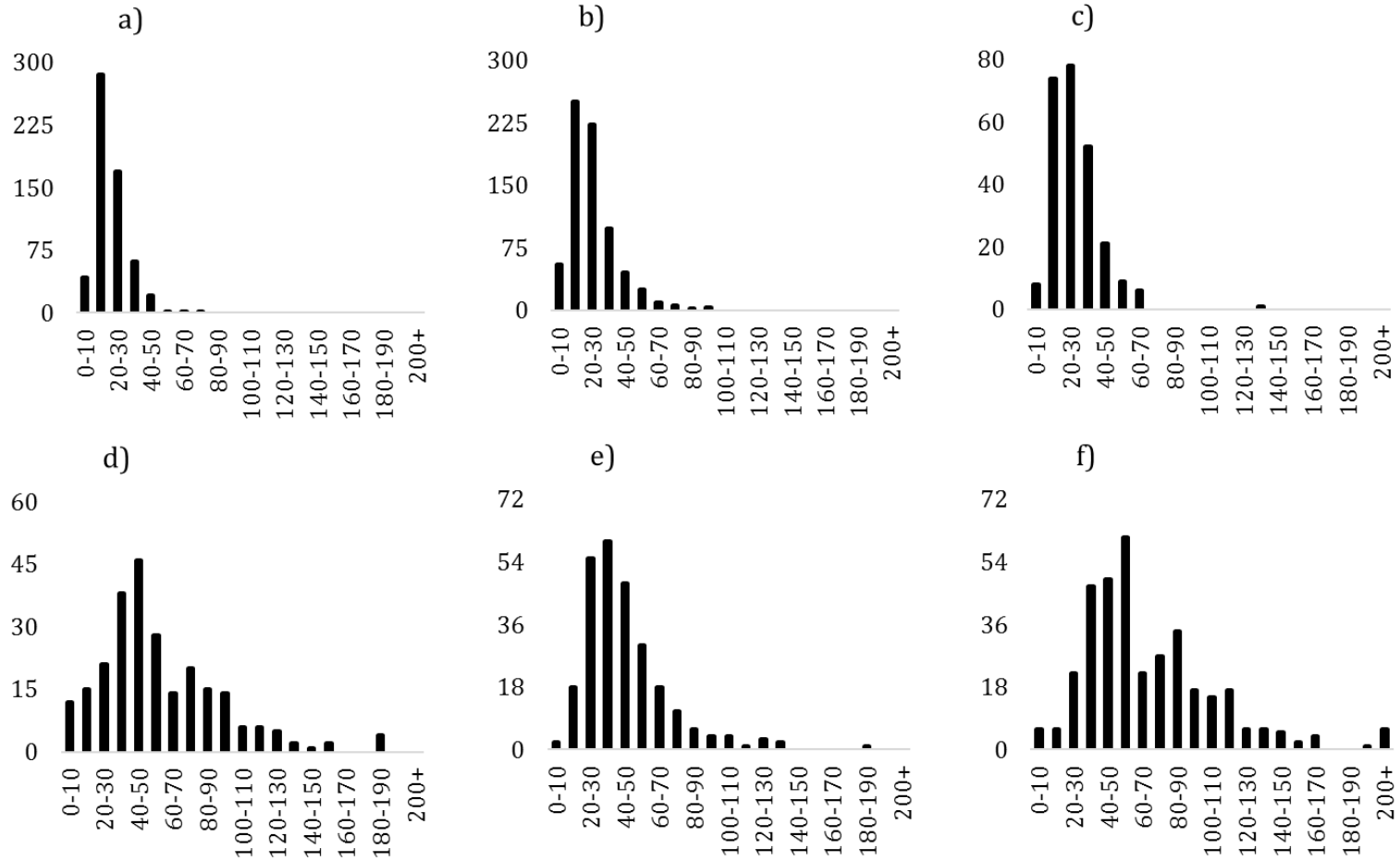

Figure 15: Distributions of grain size observed in TEM: a) as-cryomilled, b) 200°C degassed, c) 300°C degassed, d) 350°C degassed, e) 410°C degassed, f) 500°C degassed. The grain size distribution dramatically increases for powders degassed at or above 350°C which explains the large standard deviation observed in those samples.

4.2 Dislocation Density

The high dislocation density in nanocrystalline aluminum has been shown in a previous chapter (see chapter 2) to be one of the primary contributors to the overall strength of the material. However, during degassing those dislocations, generated during the cryomilling process, anneal out. Therefore, it is critical to understand the effect of degassing on the dislocation density of the material.

Of the ways to determine dislocation density, a method utilizing XRD was chosen for its simplicity and the ability to determine an estimate for the overall dislocation density. Drawbacks of this technique include that it is subject to curve fitting errors and that it assumes a uniform distribution of dislocations throughout all slip systems. The dislocation density, ρ, can be estimated from the Al grain size, d_{Al}, and microstrain, ε, measured by XRD through the Williamson-Smallman Equation [39-43]:

$$\rho = 2\sqrt{3}\left\langle \varepsilon^2 \right\rangle^{1/2} / \left(d_{Al} b\right) \tag{4.1}$$

where b is the Burger's vector for aluminum which is 0.286 nm [27]. The dislocation density as a function of degassing temperature was calculated using equation (4.1) and the result is plotted in Figure 16 and listed in Table 6.

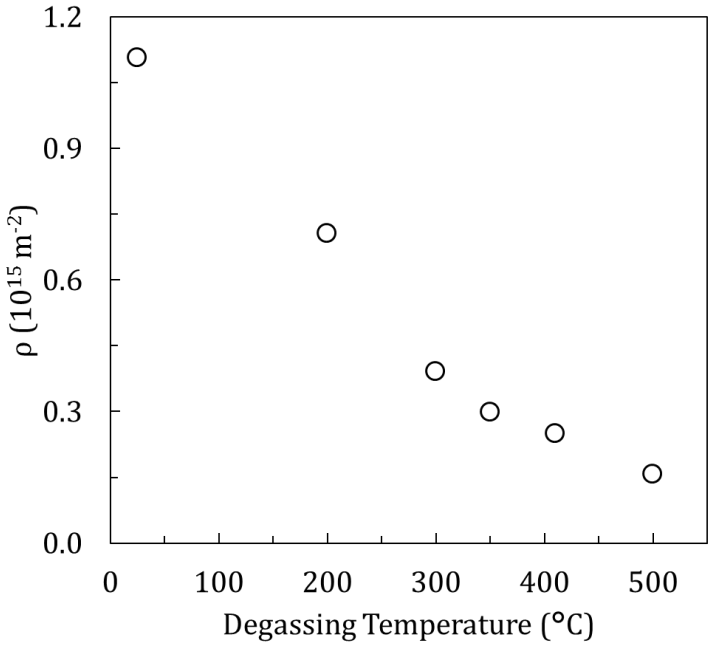

Figure 16: Dislocation density as a function of degassing temperature calculated from equation (4.1). The dislocation density decreases with increasing degassing temperature.

The 8 hr as-cryomilled dislocation density is $1.1 \cdot 10^{15}$ m^{-2}. For comparison, Zhou et al. measured the dislocation density of a 24 hr cryomilled Al-7.6(at.%)Mg via high resolution TEM to be $1.35 \cdot 10^{17}$ m^{-2} for a large submicron grains and the overall dislocation density was estimated as $5 \cdot 10^{16}$ m^{-2} [8]. This is 1-2 orders of magnitude larger than the value calculated from XRD data in this study. However, if the grain size and microstrain measured in their study is used in equation (4.1), the dislocation density is $1 \cdot 10^{15}$ m^{-2}. It is of no surprise that the dislocation density for the 24 hr cryomilled Al-Mg is similar to the 8 hr cryomilled powder in this study since steady-state deformation occurs in cryomilled Al-Mg alloys when milling for roughly 8 hours or more [3]. Therefore, the initial difference in dislocation densities is a result of the choice of analysis technique alone.

As the powders are degassed, the dislocation density is reduced due to grain recovery. Recovery should occur at relatively modest temperatures in nanocrystalline Al. Zhou et. al reported that recrystallization started as early as 100°C and occurred concurrently with grain growth up to 370°C [8]. Therefore, recovery will occur during degassing even at the lowest temperatures. The dislocation density decreased with increasing degassing temperature down to a minimum of $1.6 \cdot 10^{14}$ m^{-2} due to recovery occurring in the material. Even though the dislocation density was reduced by about an order of magnitude from the as-cryomilled condition, this dislocation density is still very high and in the same range as a heavily-cold-rolled material (10^{14} – 10^{15} m^{-2}) [22]. However, since the dislocation density measured by XRD is 1-2 orders of magnitude smaller than what was measured by TEM, the dislocation density measured by XRD should be considered a lower limit.

Table 6: Dislocation density as a function of degassing temperature calculated with the grain size and microstrain measured

	XRD Grain Size (nm)	**XRD Microstrain (%)**	**dislocation density (m^{-2})**
As-cryomilled	34	0.31	$1.1 \cdot 10^{15}$
200°C degassed	36	0.21	$7.1 \cdot 10^{14}$
300°C degassed	51	0.16	$3.9 \cdot 10^{14}$
350°C degassed	53	0.13	$3.0 \cdot 10^{14}$
410°C degassed	63	0.13	$2.5 \cdot 10^{14}$
500°C degassed	79	0.10	$1.6 \cdot 10^{14}$

4.3 Dispersoid Formation

Dispersoid formation from supersaturation occurs as a result of heating during degassing and from thermo-mechanical treatment. In these powders, dispersoids were identified by XRD (see Figure 17) between the two main aluminum peaks at 38° and 45° 2θ. Aluminum manganese, Al_6Mn (orthorhombic, oC28), peaks were found on all samples degassed at or above 300°C (Figures 17c-f). Two peaks, located at 39.86° and 41.79° 2θ, that may correspond to alumina, Al_2O_3 (hexagonal, hP60), were observed on all powders. Although aluminum oxide dispersoids have already been observed in cryomilled and consolidated AA5083 [44], the current work illustrates that these oxides are present in the as-cryomilled powders before any processing or consolidation occurs. An additional set of peaks corresponding to aluminum carbide, Al_4C_3 (rhombohedral, hR7), were also observed at 40.09° and 43.43° 2θ. Aluminum carbide dispersoids can form as a result of the reaction between aluminum and carbon-based process control agents such as the graphite used in this study [10].

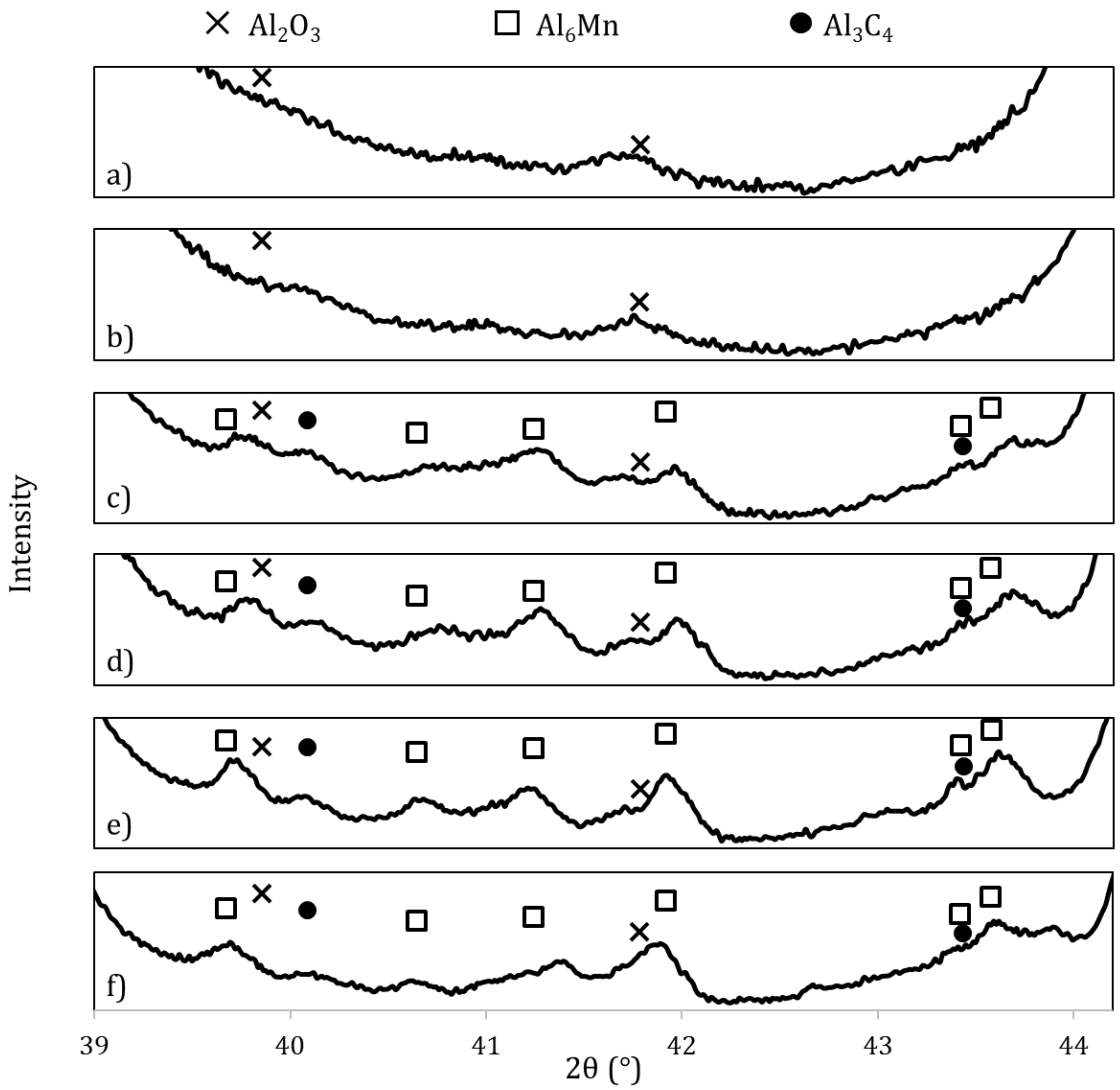

Figure 17: Fine structure observed in XRD between the two primary Al peaks in the range of 38° to 45° 2θ. Dispersoids observed were aluminum manganese, Al_6Mn; alumina, Al_2O_3; and aluminum carbide, Al_4C_3. XRD profiles are provided for a) as-cryomilled, and degassed at b) 200°C, c) 300°C, d) 350°C, e) 410°C, and f) 500°C.

The ratio of the integrated intensity of the dispersoid peaks to the main aluminum peaks provides an idea of the relative volume fraction of the dispersoid in the material (based on the direct comparison method described by Cullity [45]):

$$\frac{I_{dispersoid}}{I_{Al}} \propto \frac{v^f_{dispersoid}}{v^f_{Al}} \tag{4.2}$$

where I is the integrated intensity of the peak and v^f is the volume fraction of the phase present in the material. In this way the formation and growth of the dispersoids can be compared as a function of degassing temperature. The range evaluated was between 40.5 and 42.5 2θ since peaks outside this range tended to be too close to the main aluminum peaks which made deconvolution impossible. The Al_4C_3 phase was not analyzed as it did not lie within this range. Four peaks were analyzed, three belonging to Al_6Mn and one to Al_2O_3. Some peak height variation was observed in the Al_6Mn phase as compared to the JCPDS which may be indicative that the phase exhibits some amount of texturing. To minimize this effect, the sum of the three Al_6Mn integrated areas were normalized to the Al (111) plane in order to provide some indication of the change in the volume fraction of Al_6Mn with degassing temperature. The relative integrated intensity was also calculated for the Al_2O_3 dispersoid. The result is plotted in Figure 18. The relative intensity for the Al_2O_3 phase remains roughly constant regardless of degassing temperature indicating that the powder neither oxidizes nor do the present oxides decompose during degassing. The Al_6Mn phase is only detected in the powders degassed at or above 300°C. There is an arguably small increase in the volume fraction of Al_6Mn from degassing at higher temperatures.

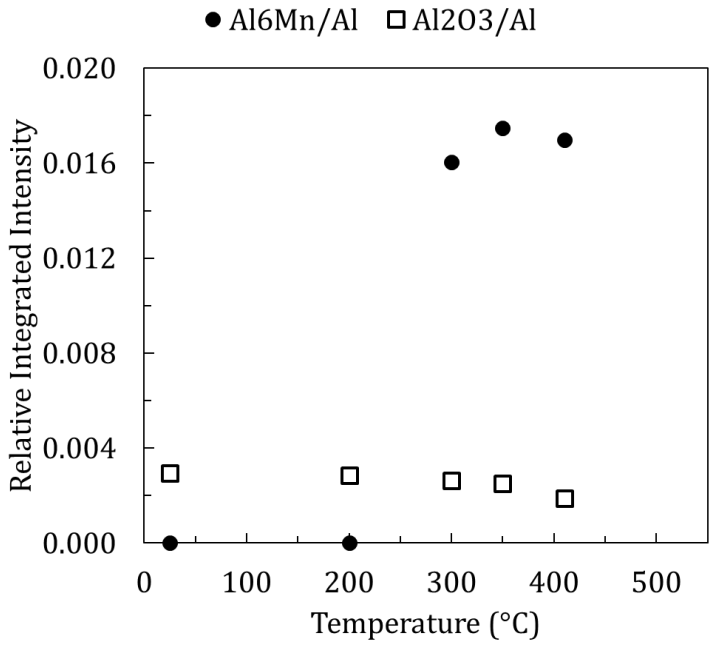

Figure 18: Relative integrated intensity of Al_6Mn and Al_2O_3, respectively as a function of degassing temperature.

Backscatter electron micrographs of the AA5083 powders after cryomilling and at each degassing step are given in Figure 19. Dispersoids were not observed on the as-cryomilled powders nor the powders degassed at 200°C, as presented in Figures 19a and 19b, respectively. Small dispersoids were observed to have formed on the powder after degassing at or above 300°C as shown in Figures 19c through 19f. For the powder degassed at 500°C, coarser dispersoids were observed (Figure 19f).

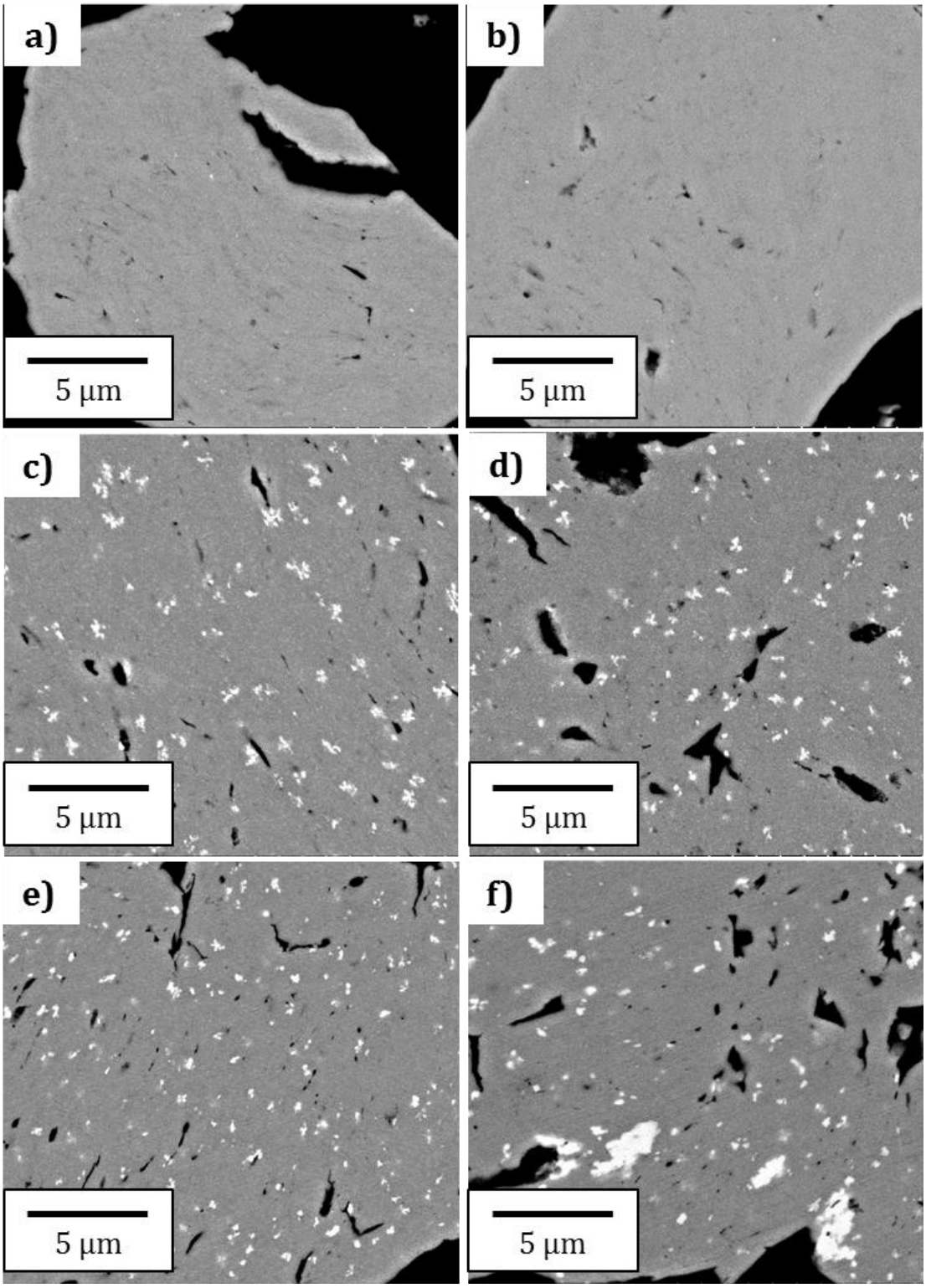

Figure 19: Microstructural evolution of the powders as a function of degassing temperature.

The size and volume fraction of the dispersoids were quantified using ImageJ software [38]. The areas of the individual dispersoids were measured and the equivalent circular diameter was calculated. Three regions of each powder were measured. The average diameter for each powder is presented in Figure 20. Dispersoids were not observed in the as-cryomilled powder (e.g., room temperature degassing, 25°C) or the powder degassed at 200°C, so the dispersoid diameter is zero. The smaller dispersoids observed in powders degassed at 300°C, 350°C and 410°C were similar in size (~200 nm). The average dispersoid size increased significantly after degassing at 500°C presumably due to coarsening of the smaller dispersoids.

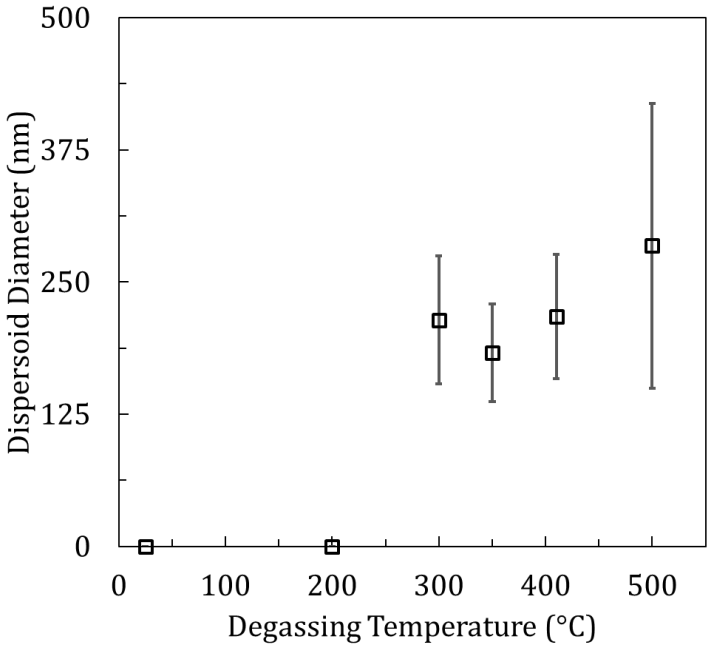

Figure 20: Influence of degassing temperature on the resultant dispersoid diameter observed in backscatter electron micrographs.

Since the cryomilled powder was porous and portions of the image also contained the epoxy surrounding the agglomerates, it was necessary to measure the volume fraction of the aluminum matrix in the powder in addition to the volume fraction of the dispersoids. The volume fraction of the dispersoids in the powder was calculated by dividing the area fraction of the dispersoids observed in the micrograph by the area fraction of the aluminum matrix. The volume fraction of dispersoids in each powder is presented in Figure 21 and summarized in Table 7. In general, the volume fraction of dispersoids increased with higher degassing temperature for an 8 hour soak at 2.7×10^{-3} Pa. Because the solubility of Mn in Al increases with temperature, it was unexpected that the Al_6Mn volume fractions increased with degassing temperature [46] . This shows that even after degassing for 8 hours, the system has not yet reached equilibrium and demonstrates the need for a comprehensive formation kinetics study for Al_6Mn in cryomilled AA5083 powders.

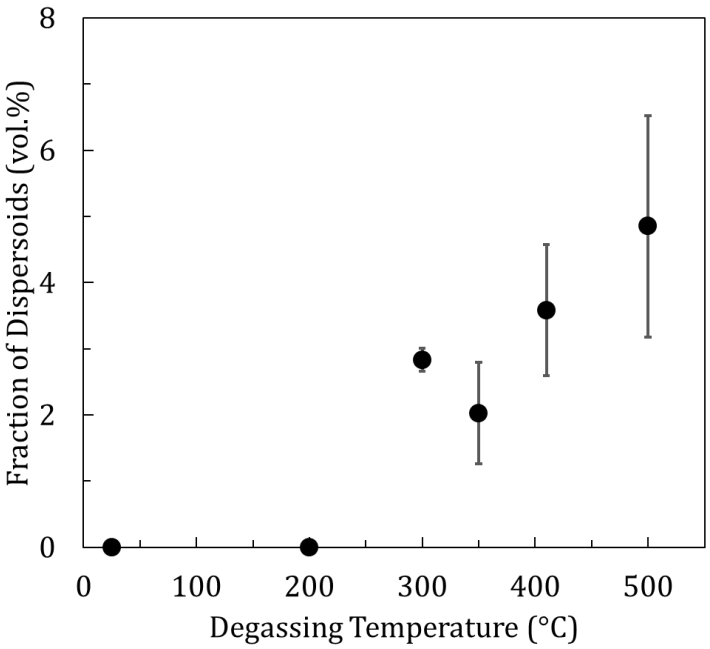

Figure 21: Influence of degassing temperature on the volume fraction of dispersoids observed in backscatter electron micrographs.

Table 7: Diameter and volume fraction of dispersoids observed in SEM.

	Dispersoid diameter (nm)	Fraction of Dispersoids (vol.%)	Number of Dispersoids Counted
As-cryomilled	0	0	0
200°C degassed	0	0	0
300°C degassed	214 ± 61	2.8 ± 0.2	768
350°C degassed	183 ± 46	2.0 ± 0.8	780
410°C degassed	217 ± 59	3.6 ± 1.0	898
500°C degassed	284 ± 135	4.9 ± 1.7	382

TEM was conducted to investigate the dispersoids observed by XRD and SEM. In Figure 22, the HAADF micrograph shows, in bright contrast and indicated by white arrows, the Al_6Mn dispersoids found in powders degassed at 410°C. Corresponding XEDS

measurements indicate the presence of Cr and Fe in these dispersoids, and therefore is identified as Al_6(MnFeCr). The Al_6(MnFeCr) phase has also been observed previously through TEM in cryomilled AA5083 [28]. These dispersoids are much larger than the surrounding nanocrystalline aluminum grains and tend to agglomerate. The larger micrometer-scale dispersoids observed in the 500°C degassed sample were not sampled via TEM, and therefore the exact chemistry is unknown but are believed to be coalesced Al_6(MnFeCr), since there are fewer of the smaller dispersoids in the powders degassed at 500°C than those degassed at 410°C as presented in Figures 19e and 19f. In general, because the dispersoids are brittle and tend to agglomerate (see Figure 22), the presence of these dispersoids should be avoided in order to preserve the fracture toughness of the resultant part.

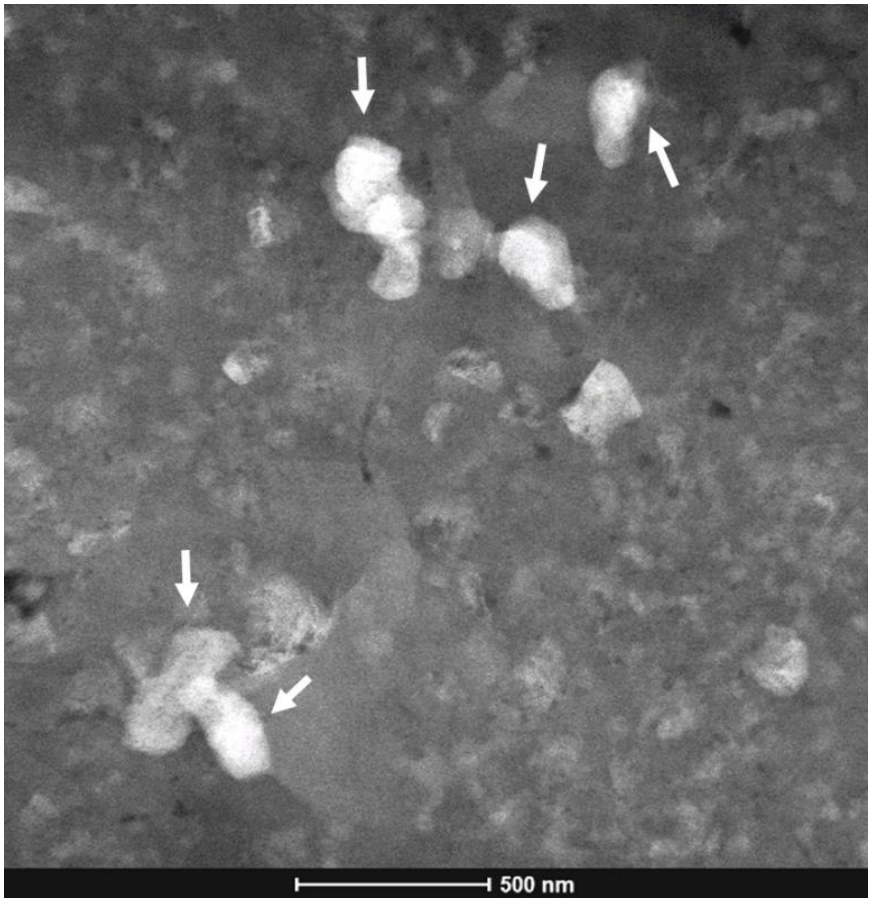

Figure 22: Typical HAADF micrograph of $Al_6(MnFeCr)$ dispersoids (brighter contrast phase indicated by white arrows) in the aluminum nanocrystalline matrix. This particular micrograph is from the powder degassed at 410°C.

4.4 Concentration of Oxygen, Nitrogen and Hydrogen

Inert gas fusion infrared and thermal conductivity chemical analysis was conducted on the powders to determine the concentration of oxygen, nitrogen and hydrogen as a function of degassing temperature and the results are summarized in Table 8. The precursor as-atomized AA5083 powder was also analyzed for comparison. It is noted that the concentration of hydrogen, 346 ppm, for the starting as-atomized powder, is much

higher than that previously reported (10 - 25 ppm) by Estrada et al. [6]. The high concentration of hydrogen may be due to absorption of moisture during the long term storage of the powder outside a glovebox. Oxygen, nitrogen and hydrogen concentrations all increase as a result of the cryomilling process.

Table 8: Chemical analysis (O, N & H) of the cryomilled and degassed powders. As-atomized AA5083 is provided for comparison.

Sample	Oxygen (wt.%)	Nitrogen (wt.%)	Hydrogen (ppm)
As-atomized AA5083	0.38 ± 0.08	0.01 ± 0.00	346 ± 3.53
As-cryomilled	1.57 ± 0.04	0.86 ± 0.15	616 ± 17.32
200°C degassed	1.18 ± 0.35	0.79 ± 0.02	504 ± 41.89
300°C degassed	1.63 ± 0.05	1.13 ± 0.02	487 ± 6.61
350°C degassed	1.00 ± 0.58	0.81 ± 0.01	136 ± 9.11
410°C degassed	1.69 ± 0.15	0.80 ± 0.02	51 ± 2.61
500°C degassed	1.74 ± 0.21	0.95 ± 0.03	45 ± 3.16

The degassing reactions that result in a change of oxygen consist of oxygen removal through the volatilization of moisture. Based on Figure 23, overall no additional oxidation nor oxygen removal is observed as a result of degassing. Therefore, we can conclude that any moisture removed from the powder reacts with free Al forming Al_2O_3 and hydrogen gas. At this point it is still unclear why the standard deviation is high for the 200 and 350°C powders.

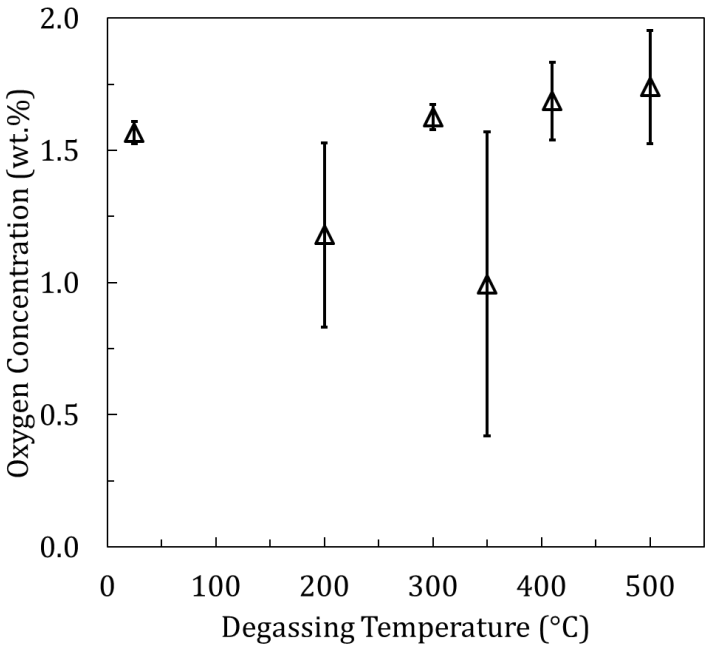

Figure 23: Oxygen concentration as a function of degassing temperature

Nitrogen is mechanically alloyed with aluminum during cryomilling [2, 4, 20, 33]. The nitrogen concentration as a function of degassing temperature is presented in Figure 24. It is unclear why the nitrogen concentration is much higher for the 300°C degassed powder than the other powders. However, based on the remaining data, it is concluded that the nitrogen is not released during degassing, and remains unchanged with degassing temperature.

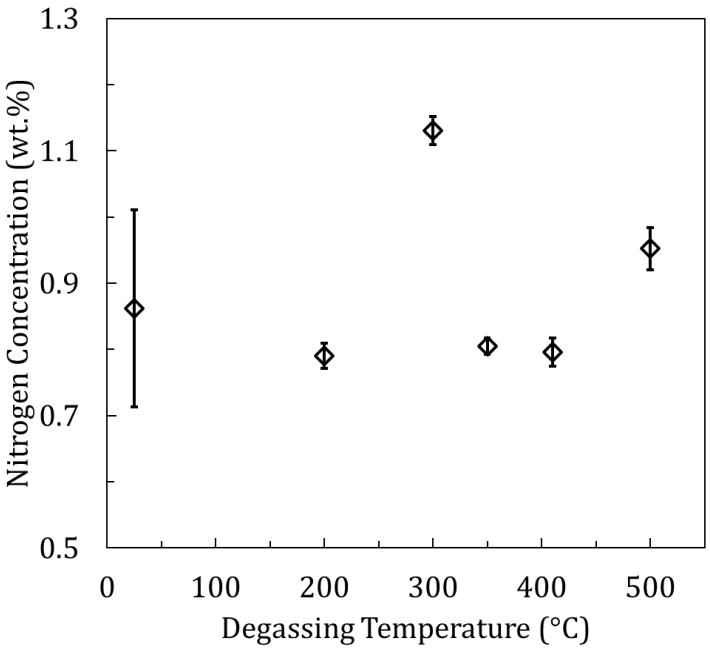

Figure 24: Nitrogen concentration as a function of degassing temperature

The concentration of hydrogen, presented in Figure 25, decreased with increasing degas temperature, in particular, significantly between 300°C and 350°C. This decrease may be associated with the decomposition of one or more hydroxides such as $Al_2O_3 \cdot 3H_2O$ or $Mg(OH)_2$. After degassing at 500°C, the hydrogen concentration reaches an apparent minimum of 45 ± 3.16 ppm. This concentration is still much higher than the maximum solubility of hydrogen of 0.0448 ppm [47] in aluminum. Therefore, it is concluded that degassing at 500°C for 8 hours at a vacuum level of 2.7×10^{-3} Pa is not sufficient to completely decompose the hydroxide into γ-Al_2O_3.

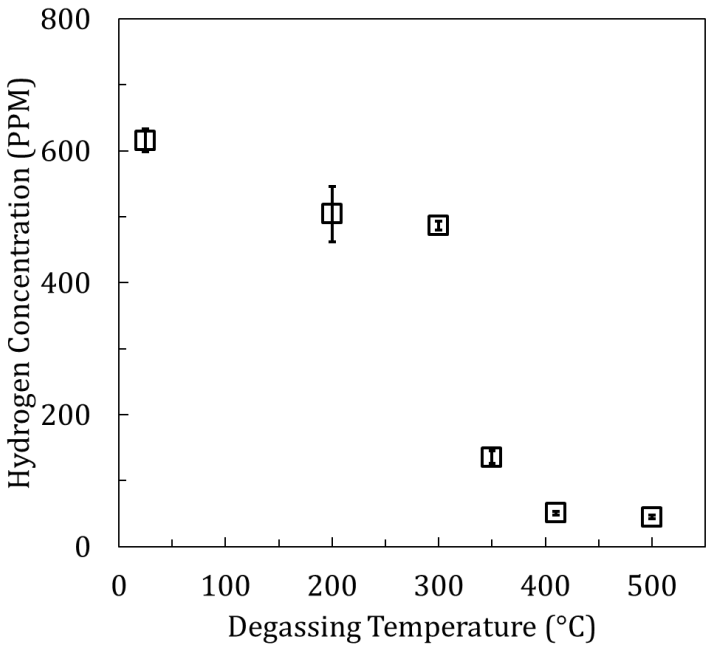

Figure 25: Hydrogen concentration as a function of degassing temperature

4.5 Summary

The microstructure and chemistry of cryomilled AA5083 powders were characterized as a function of degas temperature. Each degas process was carried out at $2.7 \cdot 10^{-3}$ Pa for 8 hours. The grain size increased with increased degassing temperature. A sharp increase in the grain size standard deviation was observed after degassing at or above 350°C which is due to growth of a few unusually large grains. After cryomilling for 8 hours, the powder had a dislocation density of $1.1 \cdot 10^{15}$ m^{-2}. The dislocation density decreased with increasing degassing temperature down to a minimum of $1.6 \cdot 10^{14}$ m^{-2} at 500°C as a result of recovery. The dislocation density calculated with XRD is 1-2 orders of magnitude smaller than that measured by TEM, and therefore should be considered a

lower limit. The $Al_6(MnFeCr)$ phase was observed in SEM, XRD and TEM for samples degassed at or above 300°C. The smaller dispersoids observed on powders degassed at 300°C, 350°C and 400°C were all roughly 200 nm in diameter. Large dispersoids were observed on the powders degassed at 500°C, and are likely coalesced $Al_6(MnFeCr)$. The volume fraction of dispersoids, in general, increased with degassing temperature. An increase in concentration of oxygen, nitrogen and hydrogen were observed as a result of cryomilling process. The nitrogen and oxygen concentrations did not significantly change by the degassing process. The concentration of hydrogen was dramatically affected by the choice of degassing temperature and decreased with an increase in degassing temperature down to a minimum of 45 ± 3.16 ppm at 500°C.

CHAPTER 5: GRAIN GROWTH

During degassing, the powders were subjected to thermal treatment resulting in grain growth. In chapter 4, the grain size varied from 34 nm in the as-cryomilled state to 79 nm after degassing at 500°C (as measured by XRD). In addition, the size distribution of grain sizes increased significantly for powders degassed at or above 350°C. It is necessary to understand the grain growth kinetics in order to explain the mechanisms behind the grain growth and estimate the effect of this processing step on the mechanical properties. In this study, the grain growth kinetics of cryomilled and degassed AA5083 were explored using the two models: the general grain growth equation and Burke's equation for grain growth in the presence of pinning dispersoids, respectively.

5.1 Analytical Approach

The typical empirical equation for isothermal grain growth is as follows:

$$D^n - D_o^n = kt \tag{5.1}$$

where D is the instantaneous grain size at time t, D_o is the initial grain size, n is the grain growth exponent and k is the rate constant. The rate constant, k, follows an Arrhenius-type relation, and can be described by:

$$k = k_o \exp\left(\frac{-Q}{RT}\right) \tag{5.2}$$

where k_o is the temperature-independent rate constant, Q is the activation energy for grain growth, R is the gas constant and T is temperature. Some versions of this equation exclude the initial grain size, D_o, from the equation however, it is necessary when the instantaneous grain size approaches the initial grain size D_0. For "ideal" grain growth the value of n is equal to 2 however, it can be much greater than 2 in experiments [48].

The general belief is that if the grain growth exponent is much greater than 2, the growth is inhibited by pinning forces such as dispersoids (Zener pinning) [49]. In this case, Burke's equation for grain growth in the presence of pinning dispersoids is typically used to model the grain growth behavior [21, 37, 49-51]:

$$\frac{D_o - D}{D_{\max}} + Ln\left(\frac{D_{\max} - D_o}{D_{\max} - D}\right) = \frac{k}{D_{\max}^2} t \qquad (5.3)$$

where D_{max} is the maximum grain size where a pinning force is possible. Grain growth has been extensively studied for cryomilled Al and Al composites. For cryomilled Al and Al composites, two separate activation energies have been reported (see Table 9). Q_H and Q_L are the activation energies for the high and the low temperature regimes respectively.

These activation energies for grain growth are typically explained in relation to the activation energy for self-diffusion of Al in the lattice, Q_{Latt}, 143.4 kJ·mol^{-1} [52], the activation energy for Mg impurity diffusion in Al 130.5 kJ·mol^{-1} [53] and the activation energy for Al grain boundary diffusion, Q_{Gb}. Because there are not any available Al tracers the activation energy for Al grain boundary diffusion can only be estimated. Mohamed and Langdon

estimate the Q_{Gb} as $0.6 \cdot Q_{Latt}$ = 86 kJ·mol^{-1} [52]. Heitjans and Karger estimate Q_{Gb} for face centered cubic metals in relation to their melting temperature as either $83.0 \cdot T_m$ or $75.4 \cdot T_m$ which is equal to 77.5 and 70.4 kJ·mol^{-1} respectively. For the purposes of this study, 81.5 kJ·mol^{-1}, the average of the previous three values, was taken as Q_{Gb}. Upon inspection of the activation energies listed in Table 9, the majority of the activation energies for the higher temperature regime are comparable to Q_{Latt} with the exception of the two composites. For the cryomilled pure Al, Q_L is close to the estimated value of Q_{Gb}. For the rest of the studies, Q_L is much smaller and was explained as relating to the relaxation and restructuring of the grains. The transition temperatures for these studies varies from 300 to 450°C and was provided without explanation. From this data, it can be concluded that for cryomilled aluminum powders (1) grain growth may be described by either the general grain growth equation or by Burke's equation, and (2) there are two grain growth temperature regimes, a low and high temperature, with their own respective activation energies.

Table 9: Summary of reported activation energies for grain growth in Al and Al composites.

Material	Method	Temperature Range Studied (°C)	Transition Temperature (°C)	Q_H (kJ/mol)	Q_L (kJ/mol)
Pure cryomilled Al [49]	Mix	200 – 600	450	112	79
Cryomilled Al + 1 wt.% diamantine [50]	Burke	150 – 500	400	25	1.1
Cryomilled AA5083 [37]	General	158 – 475	381	142	5.6
Consolidated cryomilled AA5083 [51]	Burke	200 – 400	300	124 ± 5	25 ± 5
24 h cryomilled AA5083 + 14.3 wt.% B_4C [21]	Burke	400 – 550	450	58	15

5.2 Parameter Choice

Grain growth occurs when atoms from smaller grains diffuse into larger grains and is described by the process of self-diffusion. Determination of the self-diffusion coefficient is typically approximated using tracer diffusion, i.e. a thin layer of isotopic tracer material is placed on the surface of the chemically similar bulk material (same number of protons and electrons, different number of neutrons) and diffusion occurs for a set time and temperature. Polycrystalline material contains grain boundaries where accelerated diffusion occurs. Since the diffusivity in the grain boundaries is several orders of magnitude higher than the bulk or lattice diffusivity, it is assumed the diffusion from the tracer source occurs only through the grain boundaries and tracer diffusion into the bulk occurs due to leakage from the grain boundaries.

The kinetics of diffusion can be classified into one of three regimes depending on the time, temperature, and grain size of the material according to Harrison's A-B-C classification system [54]. The Harrison A kinetics regime is a limiting case where there is mixture of grain boundary and lattice diffusion in such a way that diffusion occurs in a planar front. The Harrison A kinetics regime typically occurs at high temperatures, long anneals and/or small grain sizes. Harrison B kinetics is a mixture of grain boundary and volume diffusion however the diffusion front is not planar and concentration of tracer atoms in the grain boundaries will be higher than that in the grains forming a concentration gradient. Harrison B kinetics occurs at lower temperatures, shorter times and larger grain sizes than Harrison A kinetics. For Harrison C kinetics, the diffusion through the bulk is negligible and diffusion occurs entirely through the grain boundaries.

Harrison C kinetics occurs during short times or when a material has a very high grain boundary diffusion coefficient.

The three Harrison kinetics regimes can be differentiated by the relative amount of leakage of tracer atoms into the bulk material. This leakage is described by the diffusion length or the distance that tracer atoms have traveled into the bulk during a time, t. Mathematically, the diffusion length is the square root of the lattice diffusivity of aluminum multiplied by time. In order to differentiate each kinetics regime it is necessary to define a the parameter, Λ [54]:

$$\Lambda \equiv d_{Al} / \sqrt{D_{AlAl} t} \tag{5.4}$$

where d_{Al} is the grain size, D_{AlAl} is the diffusivity of Al in an Al lattice and t is time. Each kinetic regime, is associated with a range of Λ. In the Harrison kinetics A regime, the grain size is small compared to the diffusion length and therefore the system will be effectively homogeneous at any particular distance from the surface and diffusion will occur with a planar front. For this to occur, Harrison estimated that $\Lambda \leq 10^{-3}$ in the kinetics A regime [55]. More recently, Belova and Murch re-examined the kinetics in the Harrison A regime using Monte Carlo simulations and determined that the Harrison A regime occurred at Λ ≤ 0.4 – 0.7 [56]. The Harrison B regime occurs when Λ is in the range of 0.5 – 2 [54] and Harrison C occurs at larger Λ. D_{AlAl} has been experimentally determined as [52]:

$$D_{AlAl}\left(cm^2 s^{-1}\right) = 1.86 \cdot \exp\left(-143{,}400 / RT\right) \quad (5.5)$$

Using 8 hours as the time, t, Λ can be calculated as a function of temperature and the results are listed in Table 10. According to Table 10, the system is expected to obey Harrison A kinetics at temperatures at or above 300°C and Harrison B kinetics for the powder degassed at 200°C.

Table 10: Diffusivity for the self-diffusion of Al and Λ parameter calculated as a function of degassing temperature and grain size

T (°C)	XRD Grain Size (nm)	D (nm^2/s)	Λ
200	36	$3.0 \cdot 10^{-2}$	1.29
300	51	$1.6 \cdot 10^{1}$	0.08
350	53	$1.8 \cdot 10^{2}$	0.02
410	63	$2.0 \cdot 10^{3}$	0.01
500	79	$3.8 \cdot 10^{4}$	0.00

For the Harrison A regime, the diffusivity is determined from a rule of mixtures between the diffusivity of the bulk and the grain boundaries. Similarly, for this study the activation energy for grain growth in the high temperature regime, Q_H, will be determined as a rule of mixtures of the activation energies of the bulk and grain boundaries as follows:

$$Q_H = v^f Q_{Gb} + (1 - v^f) Q_{Latt} \quad (5.6)$$

where v^f is the volume fraction of grain boundaries. The volume fraction of grain boundaries is dependent on the grain size, d_{Al}, and the width of the grain boundary, δ. If spherical grains are assumed, the diameter of the grain has δ/2 worth of grain boundary width on either side since the grain boundaries are shared with neighboring grains. Therefore, the volume of the grain boundary can be described by:

$$V_{Gb} = \frac{\pi}{6} d^3 - \frac{\pi}{6}(d-\delta)^3 \tag{5.7}$$

The volume fraction of grain boundaries is simply the volume of the grain boundary divided by the total volume of the grain which simplifies to:

$$v^f = 1-(d-\delta)^3/d^3 \tag{5.8}$$

Taking 0.5 nm as a reasonable grain boundary width [57], the volume fraction of grain boundaries was calculated. In this study, the grain size varied from 36 – 79 nm which results in a v^f range of 0.02 – 0.04. In order to calculate a consistent Q_H, an average value of 0.03 was used for v^f. Using equation (5.6), Q_H was calculated to be 141.5 kJ·mol^{-1}.

The kinetics of the lower temperature regime will be estimated using the as-cryomilled (assumed room temperature, 25°C, degassing) combined with the 200°C results. Although Harrison B kinetics is a mixture of both bulk and grain boundary diffusion, Q_{Gb} will be used as the activation for grain growth at the lower temperature regime since the

diffusivity is much higher through the grain boundaries than the bulk for this kinetic regime. In this study, the grain size measured by XRD will be fitted first using the general grain growth equation and then via Burke's equation with OriginPro 2016 © OriginLab Corporation software.

5.3 General Grain Growth

In this study, only the temperature was varied. If equations (5.1) and (5.2) are combined, the instantaneous grain size, D, can be written in terms of T:

$$D^n - D_o^n = k_o t \exp\left(\frac{-Q}{RT}\right) \tag{5.9}$$

In order to fit the grain size to the general grain growth formula, equation (5.9) was solved for D:

$$D = \left[tk_o \exp\left(\frac{-Q}{RT}\right) + D_o^n \right]^{(1/n)} \tag{5.10}$$

The grain size in the higher temperature regime (>300°C) was fitted to equation (5.10) with D as the dependent variable and T the independent variable. Q was fixed to Q_H = 141.5 kJ·mol^{-1} and the parameters n, D_o^n, and the product t·k_o were free to vary with the fitting procedure. As a result of the fitting, n was determined as 11.8, the product t·k_o was $9.63 \cdot 10^{31}$ nm^2, and D_o was 50 nm. If t is taken as 8 hours, then k_o is equal to $3.34 \cdot 10^{27}$ nm^2·s^{-}

^{1}. The calculated D_o is somewhat larger than the as-cryomilled grain size of 34 nm and is closer to the grain size of 51 measured at 300°C. At this point it is unclear if this difference is an artifact of the fitting or if it is indicative of a jump in grain size at the transition temperature. The high temperature fitted curve is plotted as a dashed line in Figures 26a and 26b along with the measured grain size represented by open circles. The goodness of fit can be more readily judged when the natural log of the left-hand side of equation (5.9) is plotted versus the reciprocal of temperature as is done in Figure 26b. In this case, the curve becomes a straight line with a slope of -Q/R. The raw data follows the high temperature fitted line closely so we can be fairly confident in the quality of the fit.

Similarly, the low temperature regime was also fitted with equation (5.10). Because only two data points were available for fitting, all of the constants had to be specified except the product $t \cdot k_o$. Q was fixed to Q_L = 81.5 kJ·mol^{-1}, D_o was set to the as-cryomilled grain size of 34 nm, and n was 11.8. With these values it was possible to fit the lower temperature regime and is plotted in Figures 26a and 26b as a dash-dot line. After fitting, the product $t \cdot k_o$ was equal to $1.26 \cdot 10^{27}$ nm^2. If t is equal to 8 hours, then k_o is $4.39 \cdot 10^{22}$ nm^2·s^{-1}. Again, the quality of fit can be examined from Figure 26b. Unfortunately, the as-cryomilled data did not show on this graph because one cannot take the natural log of zero so only the 200°C data point is present with the lower temperature fitted curve. Ideally, this study should be repeated with additional data points in the lower temperature regime so that more confidence could be put in the fitted curve.

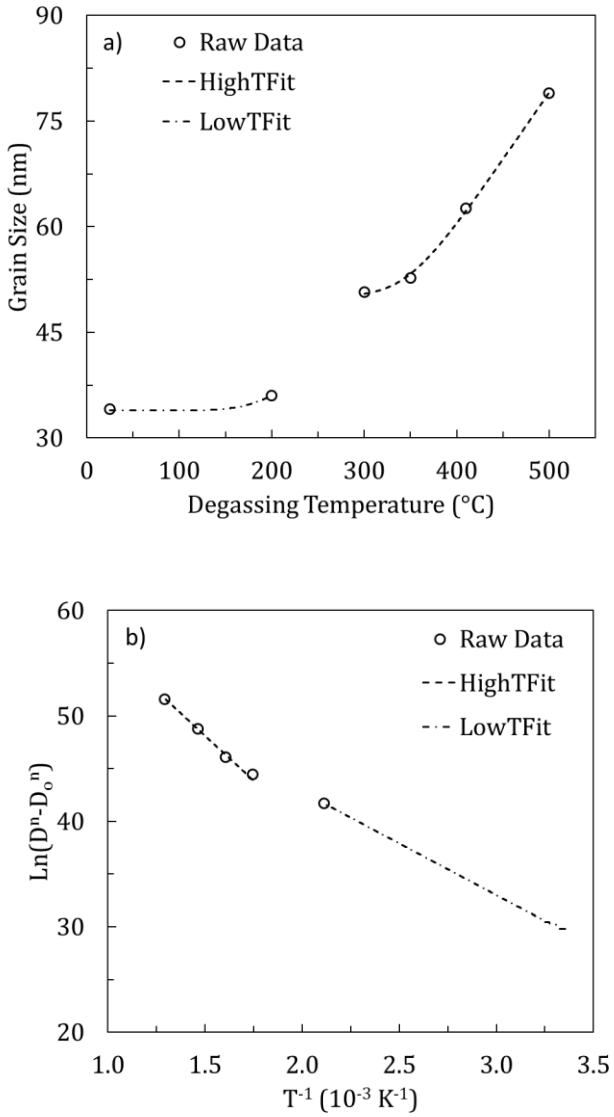

Figure 26: Grain size measured by XRD (open circles) fitted to the general grain growth equation (5.1). The data is split into two regimes: a high and low temperature with the transition temperature occurring between 200 and 300°C. The fit to the higher temperature regime is represented by a dotted line and the lower temperature by a dash-dot line. a) grain size versus degassing temperature, b) natural log of $D^n - D_o^n$ versus T^{-1}.

The two lines, in Figure 26b, representing the fitted high and low temperature regimes follow the measured grain size closely, however, there appears to be a

discontinuity at the transition temperature. Mehrer estimated the transition temperature between the Harrison A and Harrison B kinetic regimes as $0.6 \cdot T_m$ where T_m is the melting point of the material [57]. For Al, this would result in a transition temperature of 287°C which is in good agreement with the range estimated in section 5.3. Therefore, the fitted higher and lower temperature lines could be extended to connect at 287°C. Considering that the lower temperature fitted line is only an approximation, the minor difference in grain size resulting from the connection of the two lines at 287°C can be neglected.

In order for fitting to converge, the higher temperature regime required a larger D_o than the as-cryomilled grain size. This same D_o could not be used in the lower temperature regime for fitting. Since the two curves theoretically meet at ~287°C, the grain growth is continuous throughout both regimes without any discontinuity. However, the fitting shows the need for a different D_o at the beginning of each temperature regime.

5.4 Grain Growth with Pinning

In the previous section the grain growth exponent was found to be 11.8. In cases where the exponent is much higher than 'ideal' (n = 2) typically it is assumed that grain growth is occurring in the presence of pinning dispersoids in which case Burke's equation should be used. Because Burke's equation is somewhat complicated, it was found to be easier to solve for the temperature as the dependent variable and the grain size as the independent variable. Equation (5.3) was rearranged to solve for k:

$$\frac{D_{\max}^2}{t}\left[\frac{D_o - D}{D_{\max}} + \ln\left(\frac{D_{\max} - D_o}{D_{\max} - D}\right)\right] = k \tag{5.11}$$

Combining equations (5.11) and (5.2):

$$\frac{D_{\max}^2}{t}\left[\frac{D_o - D}{D_{\max}} + \ln\left(\frac{D_{\max} - D_o}{D_{\max} - D}\right)\right] = k_o \exp\left(\frac{-Q}{RT}\right) \tag{5.12}$$

Both sides were divided by the pre-exponential coefficient and a natural log was taken:

$$Ln\left\{\frac{D_{\max}^2}{k_o t}\left[\frac{D_o - D}{D_{\max}} + \ln\left(\frac{D_{\max} - D_o}{D_{\max} - D}\right)\right]\right\} = \frac{-Q}{RT} \tag{5.13}$$

Equation (5.13) was then solved for 1/T:

$$\frac{-R}{Q} Ln\left\{\frac{D_{\max}^2}{k_o t}\left[\frac{D_o - D}{D_{\max}} + \ln\left(\frac{D_{\max} - D_o}{D_{\max} - D}\right)\right]\right\} = \frac{1}{T} \tag{5.14}$$

Equation (5.14) was used to fit the measured XRD grain size using Q_H as 141.5 kJ/mol for the higher temperature regime. D_o, D_{max} and $D_{max}^2/(k_o t)$ were constants that were allowed to vary with the fitting. After fitting, D_o was equal to 51 nm, D_{max} was 1000 nm and $D_{max}^2/(k_o t)$ was $3.54 \cdot 10^{-8}$. Using the fitted value of D_{max} and a time of 8 hours, k_o was equal

to $9.91 \cdot 10^8$ $nm^2 \cdot s^{-1}$. The initial grain size is close to the grain size measured at 300°C and similar to that calculated by the general grain growth equation. The high temperature fit to Burke's equation is presented as a dotted line in Figures 27a and 27b. Unfortunately, the fit deviated significantly from the measured grain size (open circles) which is apparent in Figure 27a. Burke's model estimates the grain size at 500°C to be 129.3 nm which is much larger than the 79 nm measured in this study. This indicates that the dispersoids present in the grain boundaries are more effective in grain size suppression than allowed for in Burke's equation.

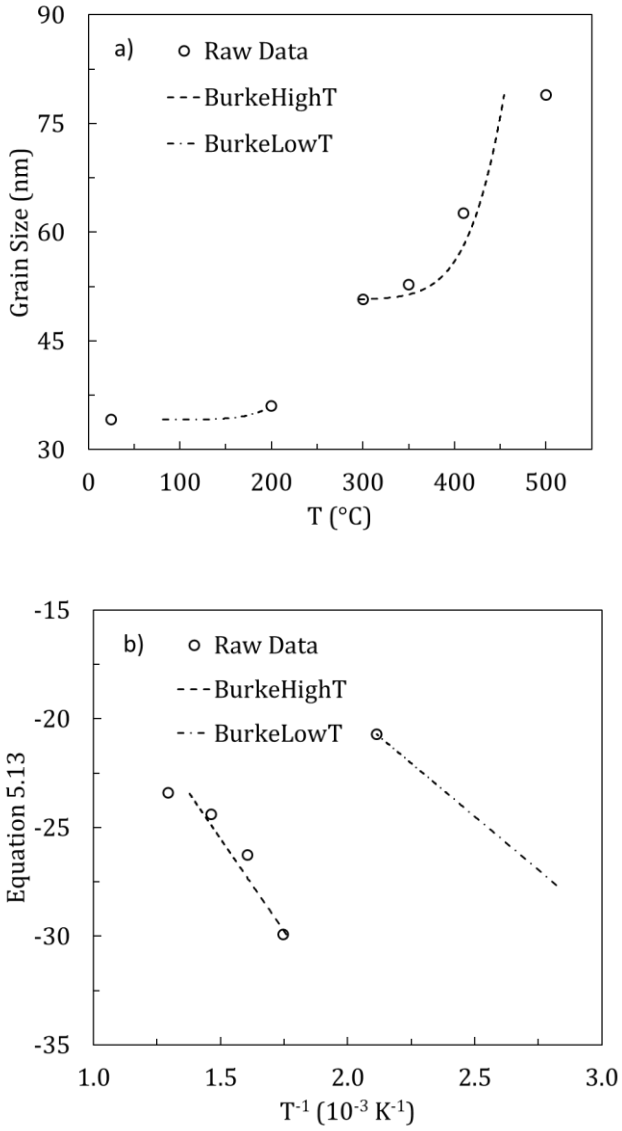

Figure 27: Grain size measured by XRD (open circles) fitted to Burke's equation for grain growth equation (5.3). The fit to the higher temperature regime is represented by a dotted line and the lower temperature by a dash-dot line. a) grain size versus temperature, b) the left-hand side of equation (5.13) versus T^{-1} such that well-fitted data should follow a straight line with slope -Q/R.

In order to fit equation (5.14) to the grain size measured in the lower temperature regime, several parameters had to be fixed. D_o was set to 34 nm, D_{max} as 1000 nm (as

determined in the higher temperature fitting), and Q_L as 81.5 kJ/mol. $D_{max}^2/(k_o t)$ was allowed to vary and was fitted as $1.46 \cdot 10^{-5}$. Using D_{max} and a time of 8 hours, k_o was calculated as $2.39 \cdot 10^6$ $nm^2 \cdot s^{-1}$. The fitted curve for the lower temperature regime is plotted in Figure 27a and 27b as a dash-dot line. Again, since so few data points were available in the lower temperature regime, this data should only be considered as an estimate until further studies are conducted.

5.5 Summary

For the first time, grain growth in a cryomilled Al alloy has been analyzed from a fundamental kinetics perspective. Two temperature regimes, commonly observed in the grain growth of cryomilled nanocrystalline aluminum, were explained using Harrison's classification of A-B-C kinetic regimes. The transition temperature between the Harrison A and B regimes was estimated to be 287°C which put the majority of our grain size data in the higher temperature, Harrison A regime. The volume fraction of grain boundaries was estimated as 0.031 assuming spherical grains. The activation energy in the higher temperature regime was calculated as 141.3 $kJ \cdot mol^{-1}$ using a rule of mixtures relation between the activation energies for the self-diffusion of aluminum through the lattice and the grain boundary diffusion respectively. This activation energy is similar to what was calculated in the related grain growth studies. The activation energy of the lower temperature regime was set equal to the activation energy for aluminum grain boundary diffusion which was estimated as 81.5 $kJ \cdot mol^{-1}$.

Grain growth was successfully modeled with the general grain growth equation for the high temperature regime with a grain growth exponent of 11.8. Since the grain growth exponent was greater than 2, Burke's equation was also applied to determine if grain growth was occurring in the presence of pinning forces. Burke's equation overestimated the grain size significantly at the higher temperatures. This indicates that the dispersoids are more effective at grain boundary pinning than allowed for in this equation.

In this study, degassing was used as a means to thermally treat the powders. It is important to note that the process of degassing requires a slow, controlled ramp to temperature in order to retain powder which is typically achieved over a number of hours. After achieving the hold temperature, the powder was held at temperature for 8 hours but for simplicity, the ramp time was neglected. Future calculations will account for the ramp time in the fitting of the equations.

CHAPTER 6: HYDROGEN EVOLUTION WITH DEGASSING

There are sources of hydrogen in as-atomized aluminum powders: 1) hydrogen dissolved into the melt before gas atomization and 2) moisture on the surface of the aluminum powders. Hydrogen readily dissolves in liquid aluminum and becomes trapped once the aluminum solidifies. Hydrogen sorption in the melt can be minimized through the use of fluxes or nitrogen gas bubbling of the melt. Hydrogen is also present in the surface oxide layer in the form of chemisorbed/physisorbed moisture. During cryomilling this surface oxide layer is broken up and redistributed throughout the bulk. Hydrogen has a low solubility in Al and may form pores or microcracks during typical consolidation processes such as hot isostatic pressing or vacuum hot pressing. Degassing of the powders is typically conducted to remove these volatiles to minimize defects in the consolidated part. In chapter 4 section 4.4, the concentration of hydrogen was measured as a function of degassing temperature with a constant soak time and it was found that the hydrogen concentration decreased with increasing degassing temperature. In this chapter, the change in hydrogen concentration will be modeled using: 1) thermo-kinetic model based on Crank's solution for desorption in a sphere and 2) an empirical model based on exponential decay.

6.1 Kinetics of Degassing Spheres

Modeling of the evolution of the microstructure and chemistry of nanocrystalline AA5083 powders due to degassing will be conducted by assuming the independence of precipitation, grain growth and impurity concentrations. For the purposes of this study, the

shape of the powder agglomerate is assumed to be spherical. The kinetics of degassing was determined based on Crank's derivation for the degassing of a sphere [58]. Fick's 2nd law in spherical coordinates:

$$\frac{\partial C}{\partial t} = D\left(\frac{\partial^2 C}{\partial r^2} + \frac{2}{r}\frac{\partial C}{\partial r}\right) \tag{6.1}$$

Initial Conditions:

1. Sphere is initially at a uniform concentration, C_1
2. Surface condition [58]:

$$-D\partial C/\partial r = \alpha\left(C_s - C_o\right) \tag{6.2}$$

where C_s is the concentration just within the sphere, C_o is the concentration required to maintain equilibrium with the surrounding atmosphere and α is a type of solid-gas distribution ratio which accounts for the difference in interfacial concentrations between the solid powder and the surrounding atmosphere. The solution to Fick's 2nd order differential equation gives the impurity concentration as a function of position and time [58]:

$$\frac{C - C_o}{C_1 - C_o} = \frac{2L\alpha}{r}\sum_{n=1}^{\infty}\frac{e^{-D\beta_n^2 t/a^2}}{\left\{\beta_n^2 + L\left(L-1\right)\right\}}\frac{\sin\left(\beta_n r/a\right)}{\sin\beta_n} \tag{6.3}$$

where r is the distance from the center of the sphere, D is the diffusivity, t is time, and a is the radius of the sphere. L is given by:

$$L = \frac{a\alpha}{D} \tag{6.4}$$

and β_n is the roots of:

$$\beta_n \cot \beta_n + L - 1 = 0 \tag{6.5}$$

In this study, we are primarily concerned with evolution of hydrogen as the powder degasses. Because hydrogen is difficult to measure, especially as a function of position, this equation was integrated with respect to position to give an expression for the remaining hydrogen solute. The expression for the total amount of diffusing substance remaining in the powder as a function of time is as follows:

$$\frac{M_t}{M_\infty} = \sum_{n=1}^{\infty} \frac{6L^2 e^{-\beta_n^2 Dt/a^2}}{\beta_n^2 \left\{\beta_n^2 + L(L-1)\right\}} \tag{6.6}$$

where M_t is the total amount of remaining solute at time t and M_∞ is the total amount of remaining solute at t = ∞.

6.2 Parametric Study

Equation (6.6) can be used to model the degassing of hydrogen from spherical aluminum powders. A parametric study was conducted in order to determine the effect of various processing conditions on the concentration of hydrogen remaining in the powder. This is conducted with the goal of predicting chemistry based on the methods currently employed and possibly illuminating variations in current processing methods which may yield better results than the standard methods currently employed. Equation (6.6) requires an infinite series summation in order to determine the concentration at any time and temperature. As it is not practical to use an infinite series for the purposes of modeling, the concentration as a function of dimensionless time $(Dt/a^2)^{1/2}$ is plotted in Figure 28 as a function of the number of summations. The equation is expected to vary from 0 to 1. However, the first summation only varies from 0 to 0.6 therefore using only the 1^{st} summation is not adequate to produce a viable solution. As the number of summations is increased, the curve approaches the target range of 0 to 1 with diminishing returns. Based on Figure 28, it is recommended to use at least 20 summations to properly represent equation (6.6).

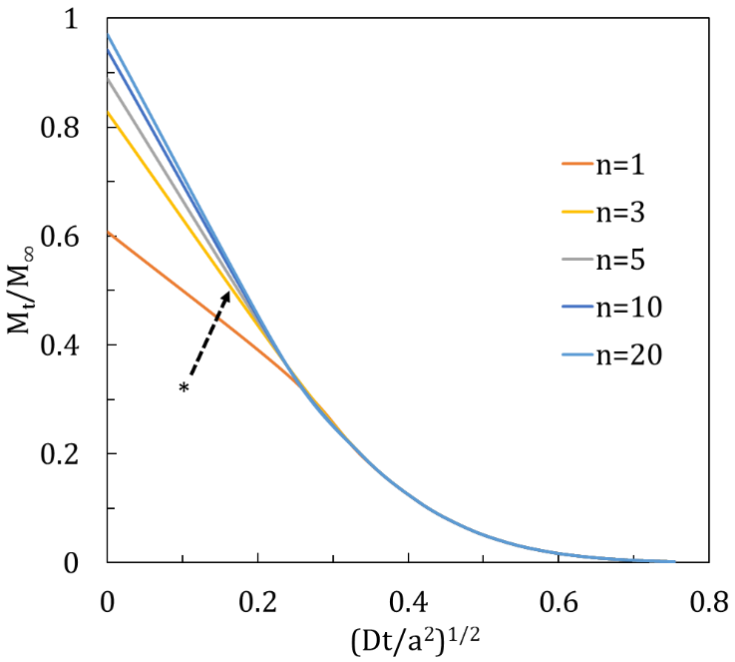

Figure 28: Shape dependency of equation (6) as a function of the number of summations. The asterisk (*) and arrow indicate the direction of increasing number of summations.

Values for the various coefficients of equation (6.6) have been chosen based on the literature. The agglomerate size was approximated to 50 μm, the diffusivity was evaluated based on Young and Scully's determination of the interstitial hydrogen diffusivity in aluminum [59] and β_n and L were derived assuming a large α. The actual values for these coefficients will need to be determined experimentally but can be used to evaluate trends. The relative concentration of degassing species according to equation (6.6) was plotted as a function of degassing time and temperature in Figure 29. The longer the powder is held at temperature, the lower the impurity concentration. In addition, the solute is degassed faster at higher degassing temperatures.

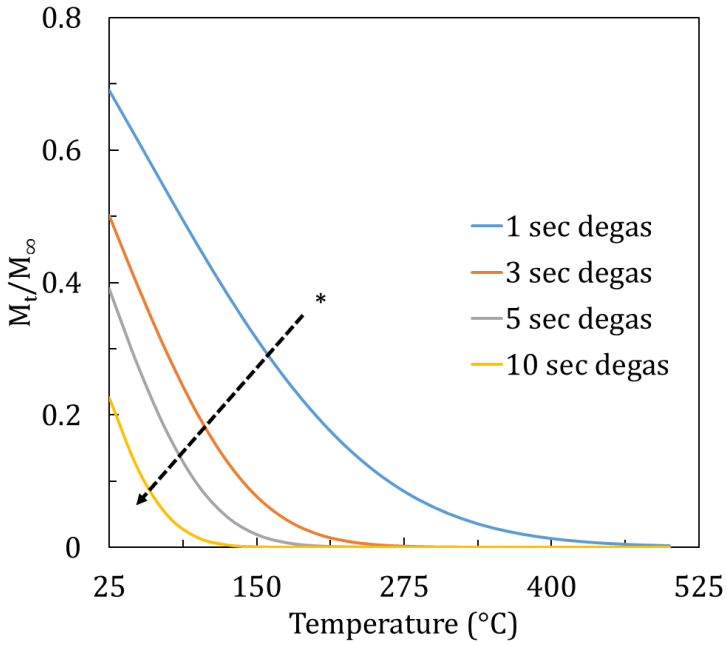

Figure 29: Relative concentration of the degassing species as a function of temperature and time. The asterisk (*) and arrow represent the direction of increasing time at temperature.

The size of the agglomerates also has a significant effect on the rate of impurity removal from the particles. A larger agglomerate has a larger diffusion distance and therefore would take longer to degas than smaller powders. To illustrate this effect, the relative concentration of degassing species was plotted as a function of degassing time for various agglomerate sizes in Figure 30. Increasing the agglomerate size by one order of magnitude dramatically reduces the rate of impurity removal from the powders. This variation in concentration is important to note for stochastic processes such as cryomilling which produce a range of agglomerate sizes. During cryomilling, two competing processes compete: cold welding and fracturing. These two processes produce a wide distribution of powder agglomerate sizes. Ye et. al. found the particle size to vary 60.40 ± 46.59 μm for 8 h

cryomilled AA5083 powders [60]. In this study, the powders were size classified with a -325 mesh sieve after cryomilling to remove any excessively large agglomerates larger than 45 μm in diameter. However, agglomerates ranging from 13 – 45 μm will still be present creating some variation in the residual hydrogen concentration.

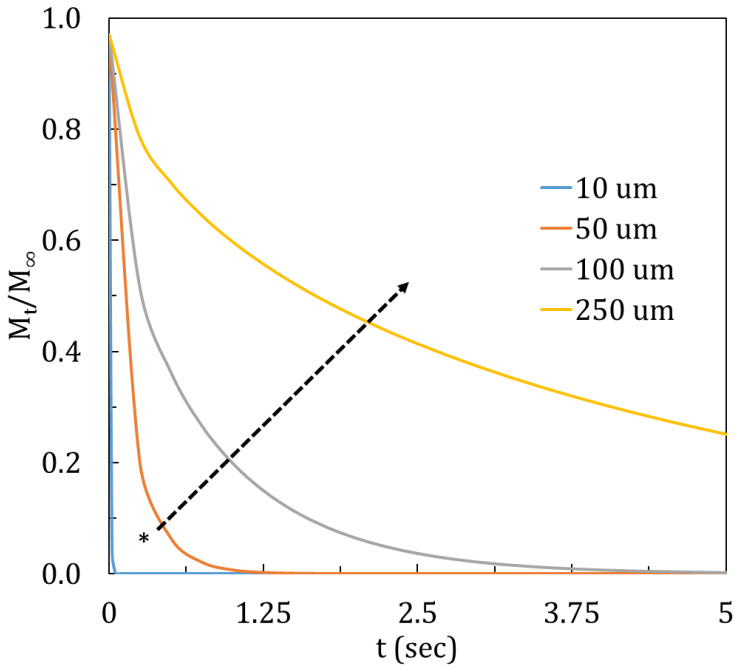

Figure 30: Relative concentration of the degassing species as a function of time and agglomerate size. The asterisk (*) and arrow indicate the direction of increasing agglomerate size.

In a work by Young and Scully, they determined that hydrogen can be trapped in aluminum by the presence of defects such as vacancies and dislocations [59]. Based on the number of ratio of the respective dislocation and vacancy sites to lattice sites the effective diffusivity can be determined. A highly defective structure, such as the case of a cryomilled

material, will have a dramatic influence on the diffusivity. Hydrogen diffusivity parameters vary widely in the literature. Room temperature diffusivities were found to vary from 10^{-24} to 10^{-5} [59]. Young and Scully were able to account for this range of diffusivities by introducing the concept of hydrogen trapping and by experimentally calculating the activation energy for the release of hydrogen from each type of trap site. Based on their work, a range of diffusivities has been chosen to explore the effect of diffusivity on the shape of equation (6.6) (see Figure 31).

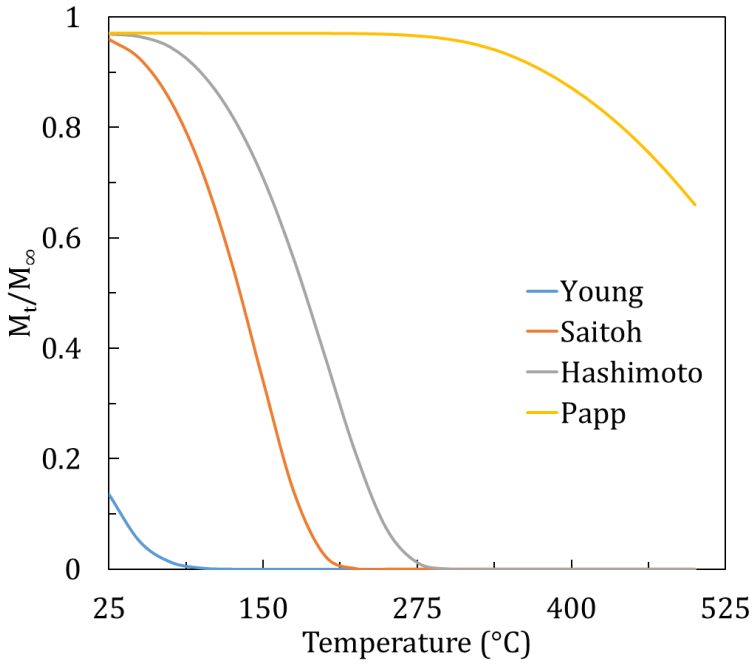

Figure 31: Effect of diffusivity parameters on the shape of the concentration vs. temperature curve. Young had the highest diffusivity and Papp had the lowest diffusivity, regardless of temperature.

Based on Young and Scully's work, diffusivities were chosen to represent various defect structures in aluminum, i.e. pure lattice diffusion (Young [59]), trapping through dislocations (Saitoh [61]), combination of dislocation and vacancy trapping (Hashimoto [62]) and an example of extremely low diffusivity (Papp [63]). The diffusion coefficients and activation energies for the diffusivities used in Figure 31 are summarized in Table 11. The equation (6) using purely lattice-based diffusivity (Young [59]) looks like a typical exponential decay curve whereas the other curves have an sigmoid-type shape to them. The diffusivity based on Papp's data is so low there is a temperature segment where there is no diminishment in concentration up until the temperature reaches a critical value. Hydrogen trapping dramatically affects the hydrogen diffusivity therefore a full understanding of the defect structure can be used to derive the effective hydrogen diffusivity.

Table 11: The diffusion coefficients for hydrogen in aluminum used in order to plot the corresponding curves in Figure 31.

Reference	Temperature Range (°C)	D_o (m^2/s)	Q (kJ/mol)
Young [59]	30 - 600	1.75×10^{-8}	16.2
Saitoh [61]	173 - 408	6.1×10^{-5}	54.8
Hashimoto [62]	300 - 400	2.6×10^{-5}	58.7
Papp [63]	450 - 590	2.5×10^{-6}	90

6.3 Hydrogen Evolution Model

In order to see the applicability of a diffusion-limited degassing model, equation (6.6) is now applied to the hydrogen concentration data derived in section 4.3. As a first approximation, a few simplifications were made to the equation (6.6) in order to fit to the experimental data. The equation was simplified to one summation and all parameters were combined into fewer constants:

$$M_t = Ae^{-B'D} \tag{6.7}$$

where A is:

$$A = 6M_\infty L^2 / \beta_n^2 \left\{\beta_n^2 + L(L-1)\right\} \tag{6.8}$$

and B' is:

$$B' = \beta_n^2 t / a^2 \tag{6.9}$$

For convenience, the natural log can be taken of both sides of equation (6.7) to remove diffusivity from the exponential:

$$Ln(M_t) = LnA - B'D \tag{6.10}$$

The diffusivity, D, changes with temperature through the Arrhenius relation:

$$D = D_o \exp\left(-\frac{Q}{RT}\right) \tag{6.11}$$

Equation (6.10) can now be updated as:

$$Ln(M_t) = LnA - B' D_o \exp\left(-\frac{Q}{RT}\right) \tag{6.12}$$

The last simplification creates an equation for the concentration of hydrogen as a function of temperature with only three constants:

$$Ln(M_t) = LnA - B \exp\left(-\frac{C}{T}\right) \tag{6.13}$$

where B is:

$$B = B_1 D_o = D_o \beta_n^2 t / a^2 \tag{6.14}$$

and C is Q/R.

The natural log of hydrogen concentration was then plotted against 1/T and fitted to equation (6.13) (see Figure 32). From this fit A was determined to be 734.92, B was 67.63 and C was 2387.45 K. The parameters making up constants A and B are difficult to deconvolute and will be addressed in future work. From parameter C it is possible to extract the activation energy for diffusion, Q as 19.8 kJ/mol. This calculated activation energy is not very different from the 16.2 ± 1.5 kJ/mol for hydrogen interstitial diffusion measured by Young and Scully [59].

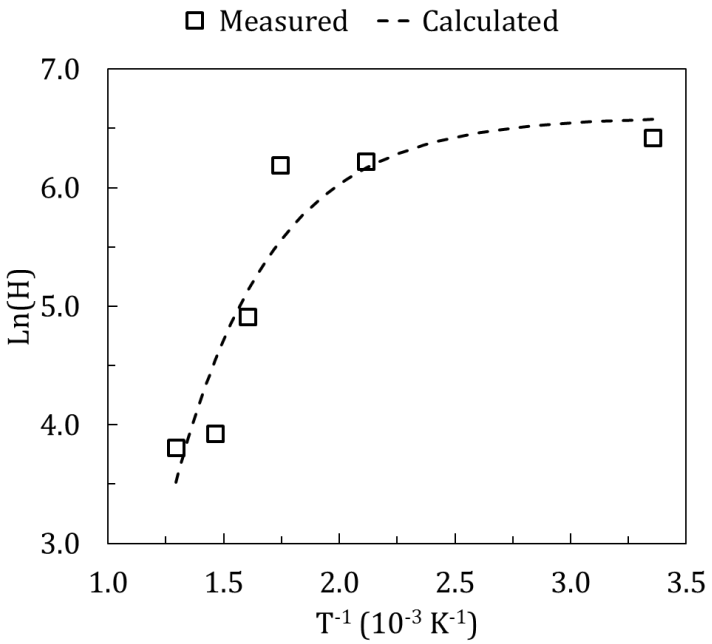

Figure 32: Fitting of the diffusion-based degassing model to the measured hydrogen data.

These parameters were then used to plot the calculated hydrogen concentration versus temperature and directly compared to the hydrogen data (see Figure 33). At lower

temperatures, there is a large deviation of the calculated curve from the raw data. This is likely caused by only using the first summation of equation (6.6) (also observed in Figure 28). The fit follows the data more closely at higher temperatures.

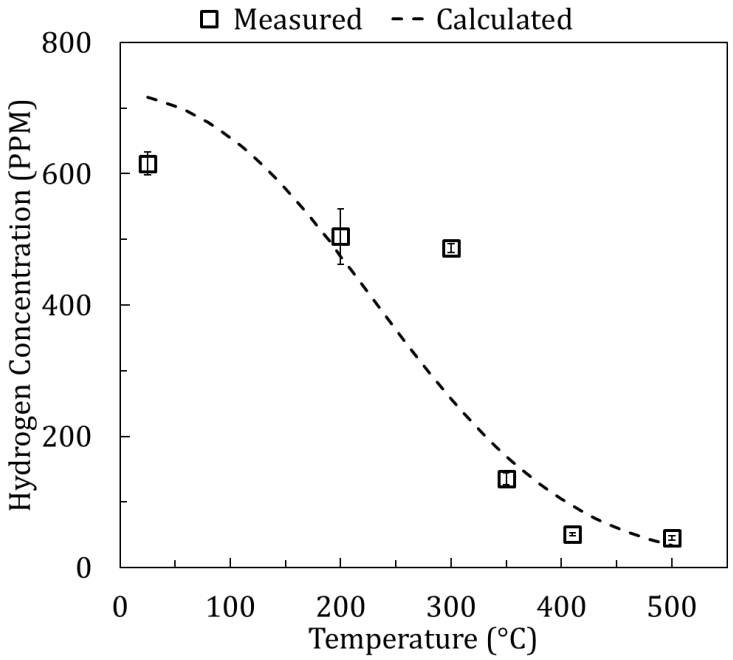

Figure 33: Crank's degassing sphere model fit to the hydrogen experimental data

An alternative to Crank's derivation is to simply fit the degassing curve using a simple exponential decay function:

$$Y = A + B\exp(-kT^n) \tag{6.15}$$

where Y is the concentration of hydrogen in ppm; A, B, k and n are constants. A and B can easily be determined from the data. A is an offset equal to the minimum hydrogen concentration attained via degassing, which in this case is 45 ppm. B is a scaling parameter which is equal to the as-cryomilled hydrogen concentration minus the minimum hydrogen concentration. In this study the maximum hydrogen concentration was 616 ppm which makes B equal to 571 ppm. In order to determine the other coefficients, equation (6.15) can be rearranged as follows:

$$\ln\left[-\ln\left(\frac{Y-A}{B}\right)\right] = n\ln T + \ln k \tag{6.16}$$

This equation was plotted in Figure 34. The equation is a straight line where the slope is equal n and the intercept is equal to ln(k). After applying this to the hydrogen data n was determined to be 9.88 and k was $3.43 \cdot 10^{-28}$ $K^{1/n}$.

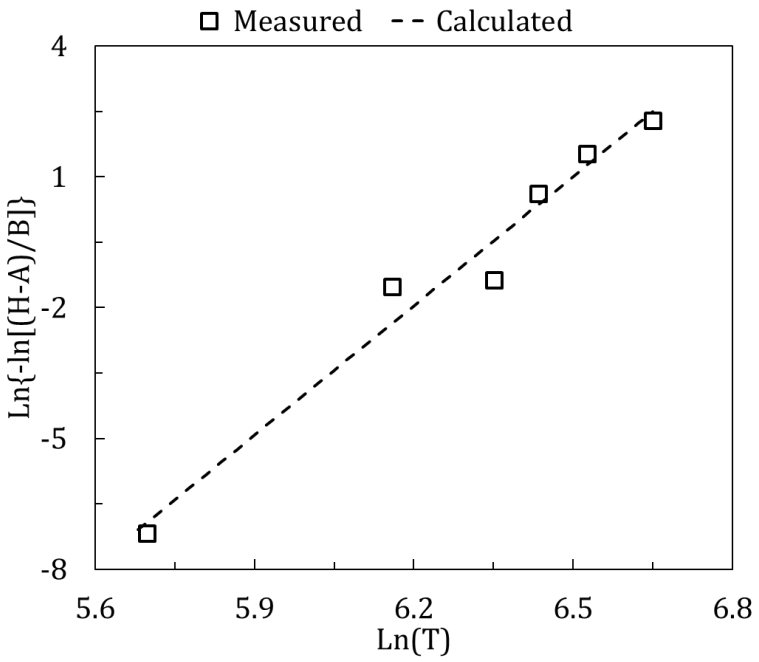

Figure 34: Plot of equation (17) used to determine the k and n coefficients

The resultant fitted profile is presented in Figure 35. The advantage to this model is that is has a better fit to the experimental data than Crank's degassing model. For engineering applications, the exponential decay model may provide a more reliable estimate, however it lacks scientific significance, i.e., diffusivities and activation energies cannot be derived from this equation.

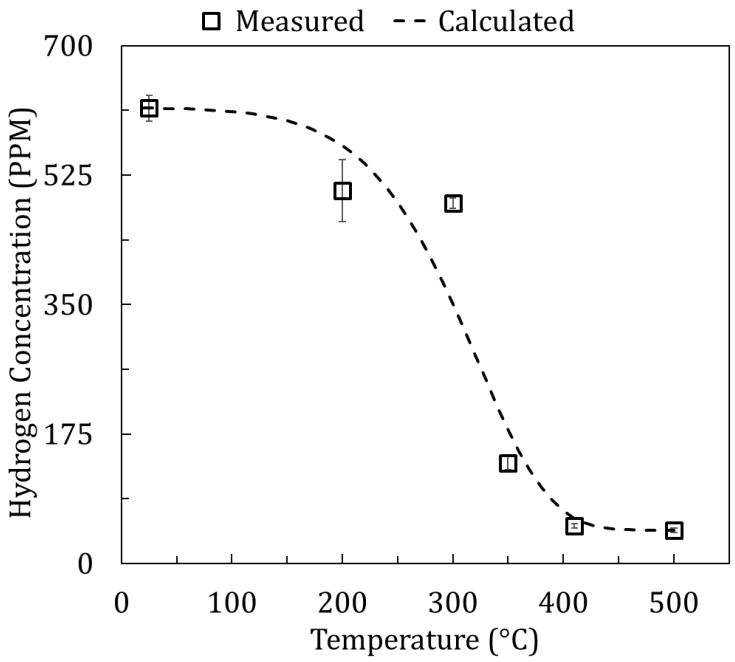

Figure 35: Exponential decay degassing model fit to the hydrogen experimental data

6.4 Summary

Pores and microcracks can form in aluminum powder during thermo-mechanical processing resulting in poor mechanical properties. To avoid this, degassing is conducted to remove hydrogen and other volatiles in the powder before consolidation. This study was conducted to examine the kinetics of degassing in a cryomilled Al alloy with the goal of fitting the hydrogen concentration as a function of degassing temperature at a fixed time. Two models were evaluated in respect to the degassing of hydrogen from cryomilled AA5083 powders: Crank's solution for desorption from a sphere and an empirical model based on a simple exponential decay function.

A parametric study was conducted on Crank's solution for desorption from a sphere in order to determine the shape and characteristics of the equation. Several observations were made:

1. Roughly 20 summations were required for an accurate solution.
2. The concentration of the degassing species decreased with increasing degassing temperature and time.
3. Large powder agglomerates inhibited the degassing of volatiles.
4. The activation energy for diffusion and the diffusion coefficient dramatically affect the shape of the degassing curve. For example, Young and Scully measured a relatively small diffusion coefficient ($\sim 10^{-8}$ $m^2 \cdot s^{-1}$) and activation energy ($\sim$16 $kJ \cdot mol^{-1}$) and the resultant curve resembled a typical exponential decay curve whereas for a moderate diffusion coefficient (10^{-6} – 10^{-5} $m^2 \cdot s^{-1}$) and activation energy ($\sim$55 $kJ \cdot mol^{-1}$) the curve appeared more s-shaped.

Some practical conclusions, based on these observations, are that it is recommended that 1) a higher temperature is used for reducing the impurity species to the lowest concentrations, and 2) that the powder be sieved before degassing to remove larger agglomerates thus decreasing the overall time and temperature required for degassing.

Due to the complexity of Crank's solution, only the activation energy of degassing could be extracted from the curve fitting. The activation energy of degassing was 19.8 $kJ \cdot mol^{-1}$ which is consistent with that measured by Young and Scully for hydrogen interstitial diffusion through the aluminum lattice. It is noted that a large deviation of the

data from the fit was observed at low temperatures and is likely due to fitting only the 1st summation from Crank's equation. A much closer fit could be obtained by fitting the hydrogen concentration to the exponential decay function but this equation is only useful for 'engineering purposes' since no thermo-kinetic parameters can be calculated from this equation.

CHAPTER 7: EFFECT ON MECHANICAL PROPERTIES

In chapter 2, the potential strength of cryomilled and degassed AA5083 powders was examined with respect to each of the available strengthening mechanisms: 1) solid solution strengthening, 2) Hall-Petch strengthening, 3) dislocation forest strengthening, and 4) Orowan strengthening. The microstructural features responsible for each mechanism was surveyed based on the available literature and the potential range of strengths for each were calculated. In this chapter the strength of 8 hr cryomilled and degassed AA5083 powders will be calculated as a function of degassing temperature based on the microstructural results observed in chapter 4.

7.1 Hall-Petch Behavior

In Chapter 2 section 2.2, nanocrystalline grains were found to be one of the primary strengthening mechanisms in cryomilled AA5083. However, these nanocrystalline grains can grow during a thermal treatment such as degassing. In Chapter 4 section 4.1, the effect of degassing on the grain size of cryomilled AA5083 powder was discussed as a function of degassing temperature. The grain size, as measured by XRD, increased from 34 nm, in the as-cryomilled powder, to 79 nm after degassing at 500°C for 8 hrs. As a result, the overall strength of the material is expected to be reduced from the degassing process. The change in strength from grain growth can be described by the Hall-Petch equation (equation (2.2)) as discussed in section 2.2 of this text. The Hall-Petch coefficient, k_{HP}, varied with Mg alloying content from 0.16 – 0.17 MPa·$m^{1/2}$ for 4.0 – 4.9 wt.% Mg. For the purposes of this study, the Hall-Petch coefficient was chosen to be 0.16 MPa·$m^{1/2}$ corresponding to an

average Mg content of 4.5 wt.% Mg. Using this coefficient and the XRD grain size in Table 5 (section 4.1), the Hall-Petch strengthening was calculated as a function of degassing temperature and is plotted in Figure 36.

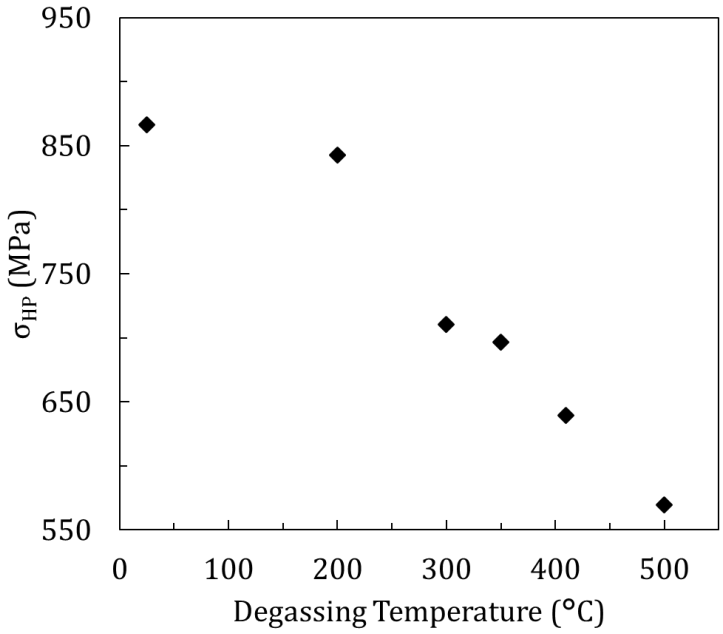

Figure 36: The Hall-Petch strengthening as a function of degassing temperature.

The Hall-Petch strengthening decreased with increasing degassing temperature from 866 MPa, in the as-cryomilled condition, to a minimum of 569 MPa after degassing at 500°C for 8 hrs. The difference in strength is roughly 300 MPa.

7.2 Dislocation Forest Strengthening

Another microstructural feature that is critical to the high strength of cryomilled materials is the high dislocation density imparted into the material during the cryomilling

process. As was seen in chapter 2 section 2.3, strengths up to ~1900 MPa could be achieved in cryomilled Al-Mg from the high dislocation density alone. In chapter 4 section 4.2, the grain size and microstrain of cryomilled AA5083, measured by XRD, were used to estimate the dislocation density via the Williamson-Smallman equation. Using this information, the dislocation forest strengthening (equation (2.3)) was calculated as a function of degassing temperature and is plotted in Figure 37.

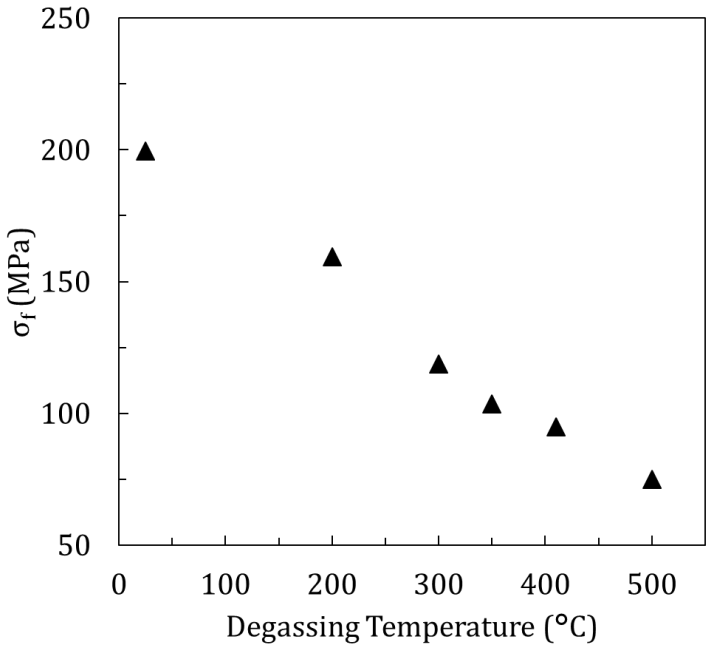

Figure 37: Calculated dislocation forest strengthening as a function of degassing temperature.

The dislocation forest strengthening decreases with increasing degassing temperature from 200 MPa in the as-cryomilled condition to 75 MPa after degassing at 500°C for 8 hours. These values are much smaller than what was originally predicted in

chapter 2. The difference can be accounted for if the method of dislocation density measurement is considered. Therefore, this estimate of dislocation forest strengthening should be considered a conservative estimate with much higher strengths possible.

7.3 Orowan Strengthening

In chapter 2 section 2.4, the Orowan strengthening relation was applied to describe 1) the large Al_6(MnFeCr) dispersoids inherent to the AA5083 alloy and 2) fine nanometer-sized dispersoids of aluminum carbides, oxides and nitrides produced as a result of the cryomilling process.

7.3.1 Large Dispersoids

The large Al_6(MnFeCr) dispersoids were initially in solid solution in the as-atomized powder and only formed while degassing at or above 300°C (see chapter 4 section 4.3). The dispersoids were roughly 204 nm in diameter after forming from 300 – 410°C. A bimodal distribution of dispersoids was observed in the 500°C degassed powder due to some coalescence of the smaller dispersoids. This resulted in a slightly higher average dispersoid size and a much larger standard deviation. The volume fraction of Al_6(MnFeCr) dispersoids increased with increasing degassing temperature. Equations (2.4) and (2.5) were used to calculate the Orowan strengthening contribution from the Al_6(MnFeCr) dispersoid and is plotted in Figure 38. Orowan strengthening increased with degassing temperature up to a maximum of 1.63 ± 0.88 MPa after degassing at 500°C.

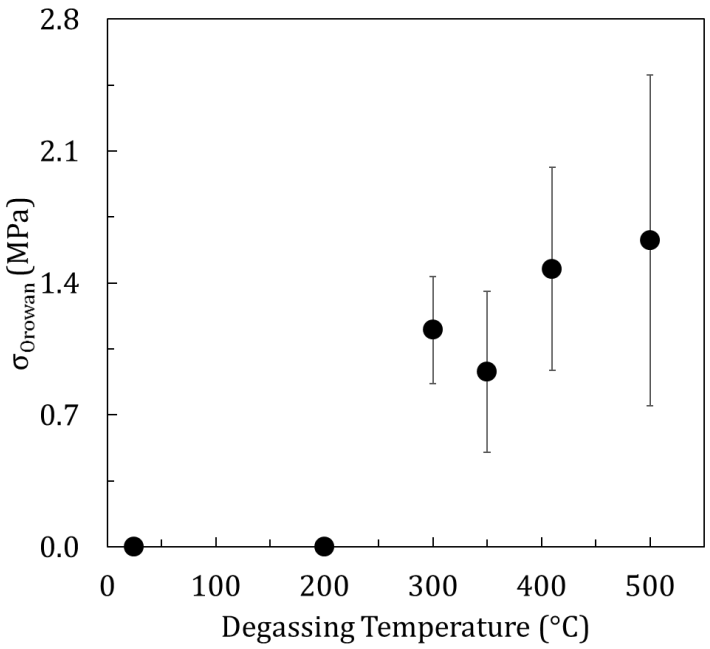

Figure 38: Orowan strengthening contribution from the presence of $Al_6(MnFeCr)$ dispersoids as a function of degassing temperature.

7.3.2 Fine Dispersoids

Aluminum carbide, Al_4C_3, forms through the mechanical alloying of the aluminum powder with the carbon-rich process control agent. In this study 0.15 wt.% graphite was uniformly blended with the AA5083 powder before milling. Assuming that all of the graphite added reacts with the aluminum to form Al_4C_3, and performing a similar calculation to that detailed in chapter 2 section 2.4, the amount of Al_4C_3 in the powder is estimated to be 0.60 wt.% which translates to 0.53 vol.%. Al_4C_3 is fairly stable and therefore is not likely to be affected by degassing so it is expected that the strengthening provided by these dispersoids is independent of the degassing conditions assuming that

the dispersoids are far enough apart that they do not coalesce as a result of the thermal treatment.

Previously in chapter 2 section 2.4, the volume fraction of nanoscale Al_2O_3 was estimated based on the thickness of the oxide layer found in literature. In this study, the oxygen content was directly measured using gas fusion and thermal conductivity chemical analysis. Assuming that 1) all of the oxygen measured in the as-atomized powder is part of the surface oxide layer in the form of Al_2O_3 and 2) this oxide layer is completely broken up to form 3-15 nm nanoscale Al_2O_3 dispersoids the weight percent of Al_2O_3 can be determined. The as-atomized AA5083 powder contained 0.38 ± 0.08 wt.% oxygen. The volume fraction of Al_2O_3 can be calculated using the procedure outlined in section 2.4 using the atomic mass of oxygen as 16.0 $g \cdot mol^{-1}$ and the density of Al_2O_3 is 3.98 $g \cdot cm^{-3}$ [64]. The volume fraction of Al_2O_3 was $5.40 \cdot 10^{-3}$. This amount of Al_2O_3 is on the lower end of the range predicted in section 2.4 and is indicative of a thin initial surface oxide layer.

After cryomilling, a new surface oxide layer formed on the surface of the aluminum powders during powder handling which remained stable through the degassing process. Characterizing this oxide layer is important to understand how the material will behave during consolidation. On average this surface oxide layer consists of 1.09 wt.% oxygen. Following the calculations above, this translates to a volume fraction of Al_2O_3 of $1.55 \cdot 10^{-2}$. Assuming the particles are spherical, the new oxide layer thickness can be estimated by solving equation (2.13) for the thickness of the oxide layer, t:

$$t = \frac{d_2}{2}\left[1-\left(1-F\right)^{1/3}\right] \tag{7.1}$$

where F is the volume fraction and d_2 is the diameter of the particle. The powder was sieved with a -325 mesh (45 μm) and the particle size is about 20 μm which can be seen in the cross-section of the 8 hr as-cryomilled powder in Figure 39. Therefore, from equation (7.1) the oxide layer thickness is 52 nm. This thickness is much larger than the 2 – 15 nm observed in gas-atomized powders [6, 35, 36] and is likely overestimated since the surface roughness of the powder increases due to deformation occurring during the cryomilling process.

Aluminum nitride, AlN, formed as a result of the mechanical alloying of the Al powder with the liquid nitrogen medium. As was seen in chapter 4 section 4.4, nitrogen increased as a result of cryomilling and remained roughly stable at 0.89 ± 0.05 wt.% regardless of degassing temperature. This corresponds well to the 0.80 ± 0.08 wt.% observed in a cryomilled AA5083 and B_4C composite [33]. Assuming that the majority of the nitrogen reacts with aluminum to form AlN it is reasonable that the nitrogen concentration does not vary with degassing temperature since AlN is stable up to about 2527°C [65]. Knowing the atomic mass of N is 14 g·mol^{-1} and the density of AlN is 3.35 g·cm^{-3} [66], the same calculation used in chapter 2 section 2.4 was to calculate the volume fraction of AlN and was $2.07 \cdot 10^{-2}$. The combined volume fraction of nanoscale dispersoids was $3.14 \cdot 10^{-2}$. Using equations (2.4) and (2.5), the Orowan strengthening contribution from

the presence of nanoscale dispersoids, σ_{nano}, was calculated to be 10.2– 25.9 MPa for dispersoids ranging in size from 3 – 15 nm.

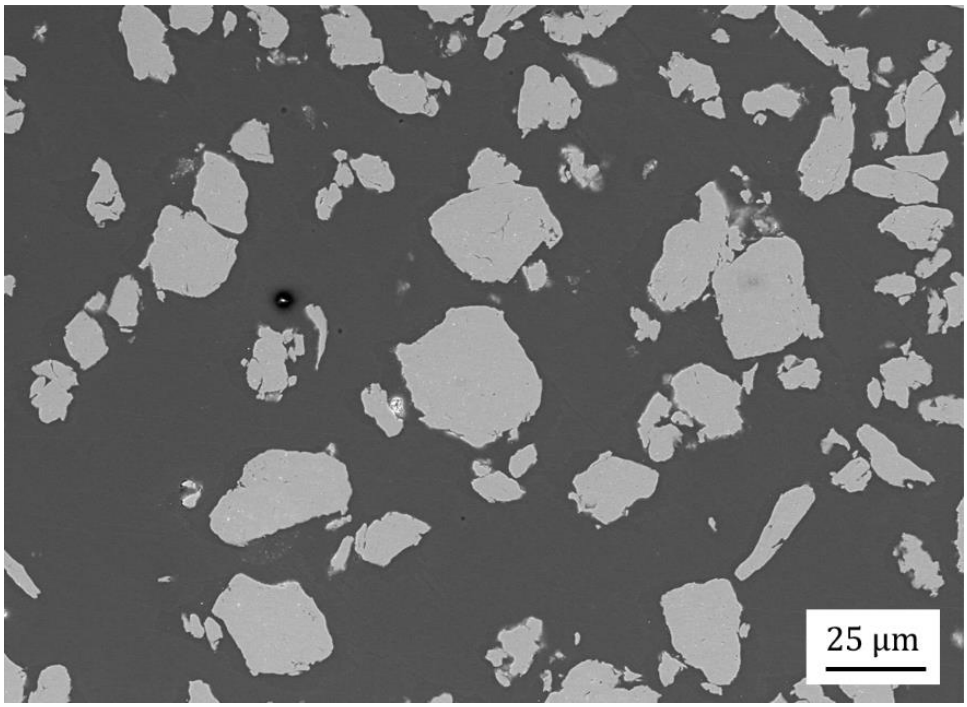

Figure 39: Secondary electron micrograph of the cross-section of the as-cryomilled powder. The particle size is roughly 20 μm.

7.4 Total Strength

In addition to the above strengthening mechanisms, the friction stress, σ_o assuming 4.5 wt.% Mg alloying, is 86.8 MPa. The sum of all of the above strengthening mechanisms is the total strength of this material and can be described by:

$$\sigma_y = \sigma_o + \sigma_{HP} + \sigma_f + \sigma_{Orowan} + \sigma_{nano} \quad (7.2)$$

The total strength is the strength expected if the powder could be consolidated without changing the microstructure. Clearly the microstructure will change as a result of thermo-mechanical processing but a complete understanding of the microstructure and mechanical properties before consolidation is necessary in order to be able to optimize the consolidation process.

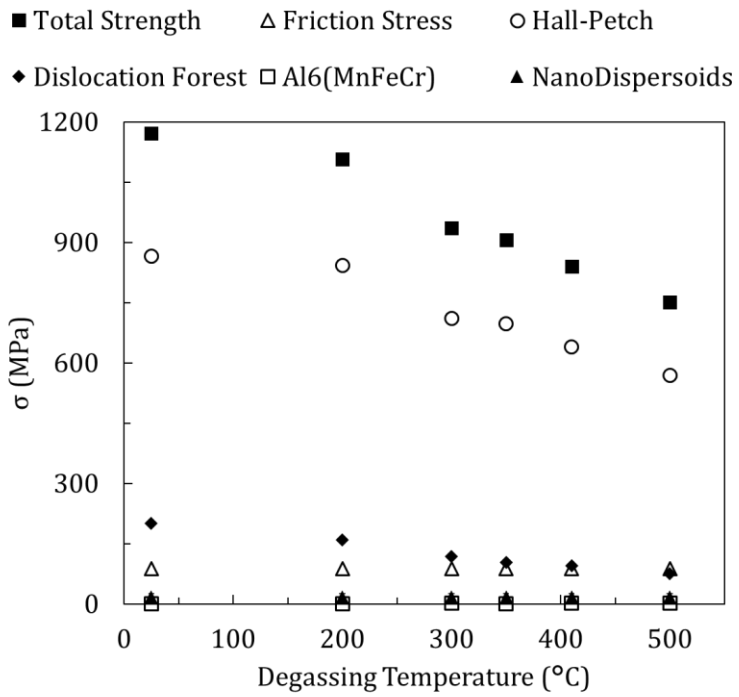

Figure 40: Strengthening contribution and total strength as a function of degassing temperature.

The change in each of the strengthening mechanisms and the resultant yield strength is plotted in Figure 40 and with the strength in log scale in Figure 41. Strengths in

excess of 1 GPa are possible with this material with the majority of the ultra-high strength from the nanocrystalline grain size. For comparison, the yield and ultimate tensile strength of a bulk AA5083-H112 alloy is only 190 and 300 MPa respectively. The other strengthening mechanisms with smaller contributions are more visible in Figure 41 where the strength is plotted in log scale. The friction stress and dislocation forest strengthening provide moderate strength of roughly 100 – 200 MPa and Orowan strengthening only provides a small strengthening increase. Although the Orowan contribution is small, the fine dispersoids help pin the grain boundaries and retard grain growth. Therefore, the fine dispersoids play an important role in preserving the overall strength of the material. A summary of the strengthening contributions and total strength as a function of degassing temperature is listed in Table 12.

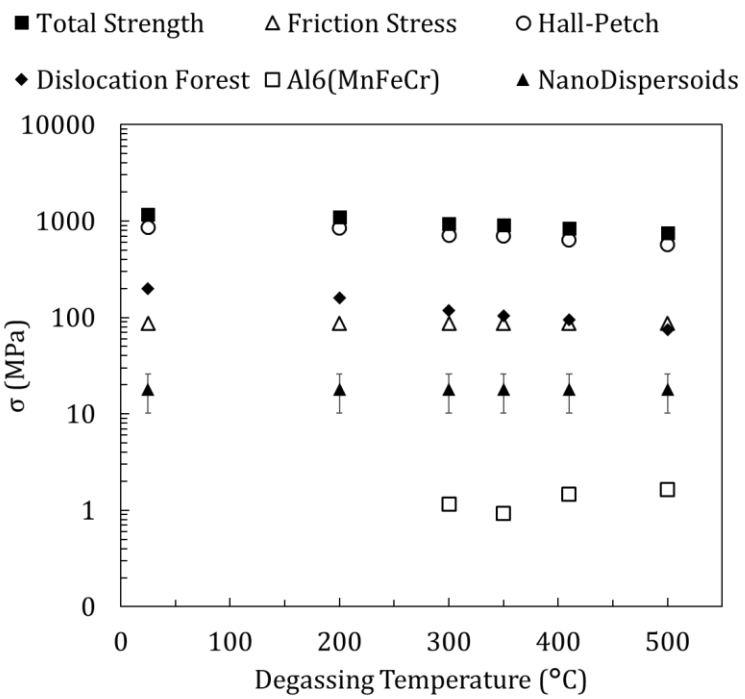

Figure 41: Strengthening contribution and total strength plotted in log scale as a function of degassing temperature.

Table 12: Summary of strengthening contributions and total strength for a cryomilled AA5083 powder

Degassing Temp (°C)	σ_o (MPa)	σ_{HP} (MPa)	σ_f (MPa)	σ_{Orowan} (Mpa)	σ_{nano} (MPa)	Total, σ_y (MPa)
25	86.8	866	200	0.00 ± 0.00	18.0 ± 7.8	1170 ± 7.71
200	86.8	843	159	0.00 ± 0.00	18.0 ± 7.8	1110 ± 7.71
300	86.8	710	119	1.15 ± 0.28	18.0 ± 7.8	935 ± 7.99
350	86.8	697	104	0.93 ± 0.43	18.0 ± 7.8	906 ± 8.14
410	86.8	639	94.8	1.47 ± 0.54	18.0 ± 7.8	840 ± 8.25
500	86.8	569	75.1	1.63 ± 0.88	18.0 ± 7.8	751 ± 8.59

7.5 Optimization of the Degassing Process

Previously, each strengthening mechanism has been discussed in detail regarding the individual contribution to strengthening except for the effect of hydrogen concentration on the overall strength. Although it is well-known that excessive hydrogen concentration is deleterious to strength even in concentrations of only several hundreds of parts per million [6, 32], currently neither a fundamental nor empirical relationship between hydrogen concentration and strength exists. Instead, to optimize the mechanical properties of cryomilled and degassed aluminum powders, the goal will be to minimize the hydrogen concentration while simultaneously minimizing the effect of the heat treatment on the microstructure. In chapter 4 it was observed that the hydrogen concentration decreased with increasing degassing temperature in a sigmoid-type curve. In chapter 6, the change in hydrogen concentration was modeled via both Fickian diffusion and through the exponential decay function. Since the exponential decay function the simpler equation, it will be further analyzed for this analysis. For sigmoid-type functions, it is easier to see the critical transition points of the curve by taking the derivative. The derivative of equation 6.15 is:

$$\frac{dY}{dT} = -BknT^{n-1}\exp\left(-kT^{n}\right) \tag{7.3}$$

The parameters of this equation are as defined in chapter 6, section 6.3. Using equation (7.3) with B equal to 571 ppm, n equal to 9.88, and k equal to 3.43·10-28 K1/n

(as-fitted in chapter 6, section 6.3); the inflection point was at 320°C. The derivative, dY/dT, was normalized by the value of the derivative at the inflection point and multiplied by 100% to observe the behavior of this transition and is plotted as a function of temperature in Figure 42. The completion of the hydrogen transition occurs when the slope of the hydrogen versus temperature plot approaches zero on the right-hand side of the transition temperature. The ideal degassing temperature should occur where the hydrogen concentration is minimized but at the lowest possible temperature to limit grain growth. If 10% of the normalized slope of the hydrogen versus temperature curve is considered as acceptably near the minimum hydrogen concentration, then according to Figure 42 the ideal degassing temperature should be 430°C corresponding to a hydrogen concentration of 50 PPM.

The effect on the microstructure and mechanical properties was re-evaluated with respect to degassing at 430°C. The friction stress and Orowan strengthening from the nanoscale dispersoids are unaffected by the degassing temperature and are 86.8 MPa and 18.0 ± 7.8 MPa respectively. The Orowan strengthening from the presence of Al_6(MnFeCr) dispersoids was small and is neglected in this analysis. Based on the general grain growth model developed in chapter 5, the grain size is expected to grow to 66 nm after degassing at 430°C. The corresponding Hall-Petch strengthening for the AA5083 alloy is 623 MPa. The relationship between dislocation density and degassing temperature is not well understood therefore, the dislocation density at 430°C was estimated by drawing a line between the dislocation densities corresponding to degassing at 410°C and 500°C and estimated the dislocation density at 430°C. The dislocation density at 430°C was estimated

as $2.3 \cdot 10^{14}$ m^{-2} corresponding to a dislocation forest strengthening of 90.76 MPa. If the powder is degassed at 430°C, the overall strength is expected to be about 819 ± 7.8 MPa. Likewise, if specific microstructural or chemical conditions are required by the consumer, the degassing temperature can be optimized and the mechanical properties estimated utilizing the work done in this study.

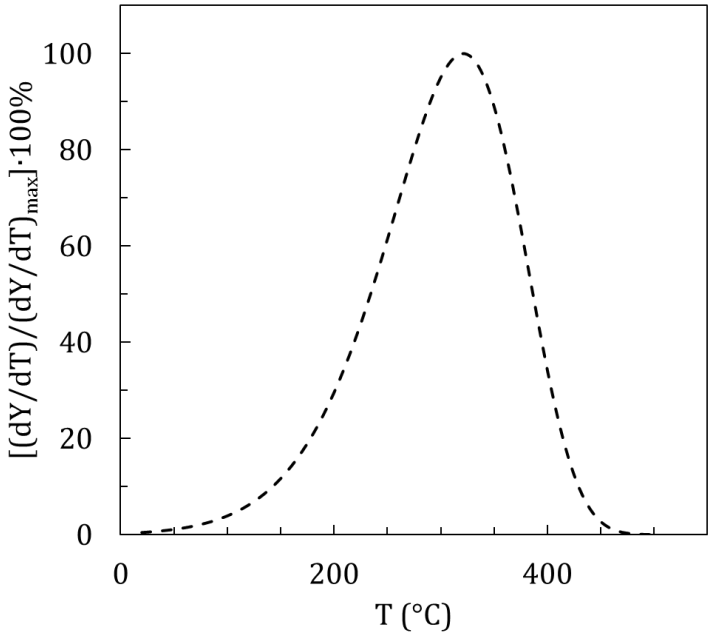

Figure 42: Normalized slope of the hydrogen versus temperature exponential decay curve

7.6 Summary

A few observations could be made as a result of this study:

- Strengthening via Hall-Petch is the most significant strengthening mechanism and decreases with increasing degassing temperature.

- Dislocation Forest strengthening has the potential to significantly strengthen the material but was found to be very susceptible to thermally activated annihilation.
- The friction stress, which is a measure of the inherent strength of the material, includes solid solution strengthening and provides moderate strengthening to the material regardless of the degassing schedule.
- Orowan strengthening from the Al_6(MnFeCr) provides a minor amount of strength to the material.
- Orowan strengthening from the nanoscale carbides, oxides and nitrides, produced as a result of the cryomilling process, provide a minor amount of strength to the material but plays an important role in grain pinning.
- The total strength of the material has the potential to be in excess of 1 GPa.
- If optimization of the degassing process requires minimal hydrogen concentration, the recommended degassing temperature is 430°C.

CHAPTER 8: COMPREHENSIVE SUMMARY

High strength, nanocrystalline aluminum can be produced through a cryomilling powder metallurgy process for the production of lightweight structural materials for civilian or military transport applications. The strengthening mechanisms for these materials include: solid solution strengthening, Hall-Petch strengthening, dislocation forest strengthening and Orowan strengthening. The potential magnitude of strengthening afforded by each mechanism was estimated by surveying the literature to determine the types and quantity of features responsible for each strengthening mechanism. For example, the nanocrystalline grain size of cryomilled materials supplies strength through the Hall-Petch mechanism. It was found that both the Hall-Petch and dislocation forest strengthening could play large roles in strengthening of the material while solid solution strengthening provided moderate strength (~100 MPa) and the contribution to strength from the Orowan mechanism ranged from minor to moderate. Together the potential strengthening contribution was well over 1 GPa.

Degassing, a type of heat treatment, of the aluminum powder is a critical step which removes volatiles such as moisture and hydrogen and improves formability. However, degassing induces microstructural and chemical changes such as recovery, grain growth, formation of dispersoids and desorption of impurities. Grains grew from 34 nm in the as-cryomilled state up to 79 nm after degassing at 500°C for 8 hours. The microstrain and grain size, measured through XRD, was used to estimate the dislocation density via the Williamson-Smallman equation. Dislocation densities were calculated to be in the range of

10^{14} – 10^{15} m^{-2} and decreased with increasing degassing temperature. Dispersoids were identified as $Al_6(MnFeCr)$, Al_4C_3, and Al_2O_3 through a combination of XRD, SEM and TEM. The presence of AlN was inferred from previous studies. The concentration of O, N and H was measured via inert gas fusion and thermal conductivity analysis. Oxygen and nitrogen increased as a result of cryomilling but remained constant afterwards regardless of degassing temperature. Hydrogen concentration initially increased up to 616 ± 17.32 PPM as a result of cryomilling but decreased with increasing degassing temperature down to a minimum of 45 ± 3.16 PPM after degassing at 500°C for 8 hours.

Grain growth, occurring during the degassing process, was modelled using two different equations: the general grain growth equation and Burke's equation. In this study, the transition temperature was rationalized as the critical temperature between the Harrison A and B kinetic regimes and is estimated as 287°C. In the Harrison A kinetic regime, a combination of lattice and grain boundary diffusion occurs. Assuming that the grains are spherical, the volume fraction of grain boundaries was estimated as 0.031. Using a rule of mixtures approach, the activation energy for grain growth in the higher temperature, type A regime was 141.5 $kJ \cdot mol^{-1}$. The lower temperature regime was assumed to be grain boundary diffusion-controlled and the activation energy was estimated as 81.5 $kJ \cdot mol^{-1}$. The general grain growth formula was successfully fitted to the grain size with a grain growth exponent equal to 11.8 and the rate constant was $3.34 \cdot 10^{27}$ $nm^2 \cdot s^{-1}$. Burke's equation for grain growth in the presence of pinning forces overestimated the grain size at the higher temperatures. This may be indicative that the dispersoids

present in cryomilled Al alloys are much more effective as pinning forces than allowed for in Burke's equation.

Hydrogen, in the form of volatiles such as moisture, H_2 gas and hydrogen-containing PCA, is desorbed during the degassing process. The kinetics of the desorption of volatiles were explored using two models: Fickian diffusion in spherical coordinates and an empirical exponential decay function. A parametric study of Crank's solution for the desorption from a sphere was conducted to determine how each parameter affected the desorption behavior. A few observations were made: higher temperatures and times reduced the impurity content in the material. A larger agglomerate size resulted in a slower desorption response. Diffusivity of the volatile species strongly affected the shape of the curve. Crank's solution was fitted to the concentration of hydrogen as a function of degassing temperature. The activation energy for degassing was 19.8 $kJ \cdot mol^{-1}$. A better fit was obtained by using an exponential decay function however this equation does not incorporate any kinetic coefficients and therefore is without scientific value.

The mechanical properties were re-evaluated with respect for the observed microstructure as a function of degassing temperature. Grain growth during degassing dramatically reduced the estimated Hall-Petch strengthening from 866 MPa in the as-cryomilled state to 569 MPa after degassing at 500°C for 8 hours. Regardless, the Hall-Petch strengthening was found to remain as the primary strengthening mechanism. The dislocation density calculated by the Williamson-Smallman equation is much smaller than the maximum dislocation density measured in the literature. As a result, this strengthening mechanism was re-evaluated to provide only moderate strength to the material. Orowan

strengthening remained the smallest contributor to strength and was within the ranges predicted.

APPENDIX A: LIST OF PUBLICATIONS AND PRESENTATIONS

A.1 Publications

1. **C. Hofmeister**, L. Zhou, A. Giri, T. Delahanty, K. Cho, Y.H. Sohn, "Cryogenic Attrition of Magnesium WE43 Alloy Powders," in preparation.
2. K.H. Kaisar, **C. Hofmeister**, M.M. Schneider, B. Yao, A. Pedigo, A.K. Giri, Y. Sohn, K.C. Cho, M. van den Bergh, B.S. Majumdar, "Tensile Properties and Microstructure of a Cryomilled Nanograined Al-Mg Alloy Near the AA5083 Composition," in preparation.
3. **C. Hofmeister**, A. Giri, T. Zahra, H. Hyer, B. Majumdar, K. Cho, Y.H. Sohn, "Influence of Cryomilling Time and Chemistry on the Microstructure and Mechanical Behavior of Nanocrystalline AA5083 Consolidated by Hot Isostatic Pressing and Extrusion," Light Metals TMS 2017: in preparation.
4. **C. Hofmeister**, L. Zhou, F. Kellogg, A. Giri, K. Cho, Y.H. Sohn, "Microstructural and Compositional Evolution in Cryomilled AA5083 Powders during the Degassing Process," Journal of Materials Science: submitted.
5. B. McWilliams, J. Yu, **C. Hofmeister**, F. Kellogg, "Flash sintering phenomenon in aluminum alloy powder," Powdermet 2016: Sintering II, June 5-8, 2016, Boston, MA, USA, 274-279.
6. M. Nezafati, A. Giri, **C. Hofmeister**, K. Cho, M.M. Schneider, L. Zhou, Y.H. Sohn, C.S. Kim, "Atomistic study on the interaction of nitrogen and Mg lattice and the nitride formation in nanocrystalline Mg alloys synthesized using cryomilling process," Acta Materialia: Volume 115 (2016), pp. 295-307; DOI 10.1016/j.actamat.2016.06.012.
7. F. Kellogg, L. Zhou, **C. Hofmeister**, A. Giri, Y.H.Sohn, K. Cho, "Nanostructuring of Tungsten through Cryogenic Attrition," Powdermet 2015: Novel Processing, May 17-20, 2015, San Diego, CA, USA, 364-378.
8. **C. Hofmeister**, M. Klimov, T. Delahanty, K. Cho, Y.H. Sohn, "Quantification of nitrogen impurity and estimated Orowan strengthening through secondary ion mass spectroscopy in aluminum cryomilled for extended durations," Materials Science & Engineering A: Volume 648 (2015), pp. 412-417; DOI 10.1016/j.msea.2015.09.007.
9. L. Zhou, F.R. Kellogg, **C. Hofmeister**, A. Giri, K.C. Cho, Y.H. Sohn, "Nanostructured Tungsten through Cryogenic Attrition," International Journal of Refractory Metals and Hard Materials: Volume 52 (2015), pp. 70-77; DOI 10.1016/j.ijrmhm.2015.05.016.
10. **C. Hofmeister**, A. Giri, S. Brennan, Y.H. Sohn, T. Delahanty, K. Cho, "Effect of Process Control Agent on the Microstructure and Mechanical Behavior of an Aluminum and B_4C Metal Matrix Composite," Light Metals or Magnesium Technology: Light-metal Matrix (Nano)-composites, February 16-20, 2014, San Diego, CA, USA, 1-4.
11. Y. H. Sohn, T. Patterson, **C. Hofmeister**, C. Kammerer, W. Mohr, M. van den Bergh, M. Shaeffer, J. Seaman and K. Cho, "Tailoring Microstructure and Properties of Hierarchical Aluminum Metal Matrix Composites Through Friction Stir Processing," Journal of Metals (JOM): Volume 64, Issue 2 (2012), pp. 234-238; DOI 10.1007/s11837-012-0249-9.
12. **C. Hofmeister**, B. Yao, T. Delahanty, M. van den Bergh, K. Cho, Y.H. Sohn, "Composition and Structure of Nitrogen-containing Dispersoids in Tri-modal Aluminum Metal Matrix Composites," Journal of Materials Science, Vol. 45 (2010) pp. 4871-4876; DOI 10.1007/s10853-010-4571-8.

13. B. Yao, T. Patterson, **C. Hofmeister**, Y.H. Sohn, M. van den Bergh, C. Smith, T. Delehanty, K. Cho, "Microstructural Features Influencing the Strength of Commercial Scale Lightweight Nanoengineered Trimodal Aluminum Composites," Composites Part A 41(2010) pp. 933-941; DOI 10.1016/j.compositesa.2010.02.013.
14. B. Yao, **C. Hofmeister**, Y.H. Sohn, K. Cho, "Analytical Characterization and First-Principle Calculation of Dispersoids in Trimodal Aluminum Metal Matrix Composites," Advances in Powder Metallurgy & Particulate Materials - 2010, June 27-30, 2010, Hollywood, FL, USA, II-9-3.

A.2 Conference Presentations

1. **C. Hofmeister**, A. Giri, T. Zahra, H. Hyer, B. Majumdar, K. Cho, Y.H. Sohn, "Influence of Cryomilling Time and Chemistry on the Microstructure and Mechanical Behavior of Nanocrystalline AA5083 Consolidated by Hot Isostatic Pressing and Extrusion," To be presented at the 2017 TMS Annual Meeting & Exhibition: Aluminum Alloys, Processing and Characterization, February 26- March 2, 2017, San Diego, CA, USA.
2. **C. Hofmeister**, L. Zhou, F. Kellogg, A. Giri, T. Zahrah, K. Cho, Y.H. Sohn, "Microstructure and Mechanical Properties of AA5083 Produced through Cryogenic Attrition and HIP," Presented at the 2016 TMS Annual Meeting & Exhibition: Ultrafine Grained Materials, February 14-18, 2016, Nashville, TN, USA.
3. K. Cho, A. Giri, F. Kellogg, **C. Hofmeister**, C. Kammerer, L. Zhou, E. Geller, A. Mehta, Y.H. Sohn, "Progress Towards Development of Nanostructured Magnesium Alloys and Composites: Understanding of Magnesium Strengthening by Solid Solutioning and Grain Size Reduction," Presented at 2016 TMS Annual Meeting & Exhibition: Bulk Processing of Nanostructured Powders and Nanopowders by Consolidation, February 14-18, 2016, Nashville, TN, USA.
4. F. Kellogg, B. McWilliams, **C. Hofmeister**, A. Giri, Y.H. Sohn, K. Cho, "Spark Plasma Sintering of Nanostructured AA5083 Powder with Varying Cryomilling Duration," Presented at the 2016 TMS Annual Meeting & Exhibition: Bulk Processing of Nanostructured Powders and Nanopowders by Consolidation, February 14-18, 2016, Nashville, TN, USA.
5. Y.H. Sohn, **C. Hofmeister**, L. Zhou, F. Kellogg, A. Giri, K. Cho, "Development of AA5083 Metal Matrix Composite for Lightweight Vehicles: Lessons Learned," Presented at Materials Science & Technology 2015: Ultra High Performance Metals, Metal Alloys, Intermetallics, and Metal Matrix Composites for Aerospace and Defense Applications, October 4-8, 2015, OH, USA.
6. **C. Hofmeister**, L. Zhou, A. Giri, T. Delehanty, K. Cho, Y.H. Sohn, "Evolution of Microstructure and Chemistry with Cryogenic Attrition of Magnesium WE43 Powders," Presented at Materials Science & Technology 2015: Ultra High Performance Metals, Metal Alloys, Intermetallics, and Metal Matrix Composites for Aerospace and Defense Applications, October 4-8, 2015, Columbus, OH, USA.
7. **C. Hofmeister**, F. Kellogg, A. Giri, K. Cho, Y.H. Sohn, "Kinetic Model for the Degassing of Hydrogen from Nanocrystalline AA5083 Powder," Presented at Materials Science & Technology 2015: Ultra High Performance Metals, Metal Alloys, Intermetallics, and Metal Matrix Composites for Aerospace and Defense Applications, October 4-8, 2015, Columbus, OH, USA.
8. F. Kellogg, **C. Hofmeister**, A. Giri, Y.H. Sohn, K. Cho, "Nanostructuring of Tungsten through Cryogenic Attrition," Presented at Powdermet 2015: Refractory Metals, Carbides & Ceramics, Tungsten, Alloys, and Composites, May 17-21, 2015, San Diego, CA, USA.
9. **C. Hofmeister**, F. Kellogg, A. Giri, K. Cho, Y.H. Sohn, "Optimization of Degassing Parameters for nanocrystalline AA5083 Powder," Presented at the 2015 TMS Annual

Meeting & Exhibition: Aluminum Alloys: Development, Characterization, and Applications, March 15-19, 2015, Orlando, FL, USA.

10. F. Kellogg, **C. Hofmeister**, A. Giri, Y.H. Sohn, K. Cho, "Tungsten Grain Refinement via Low-Energy Cryogenic Ball Milling," Presented at the 2015 TMS Annual Meeting & Exhibition: Refractory Metals 2015, March 15-19, 2015, Orlando, FL, USA.
11. **C. Hofmeister**, L. Zhou, T. Delehanty, A. Giri, F. Kellogg, K. Cho, Y.H. Sohn, "Microstructure and Nitrogen Impurity Concentration of Nanocrystalline AA5083 Cryomilled for Extended Durations," Invited Presentation at Materials Science & Technology 2014: Advanced Aluminum Alloys, Composites, and Process Technologies, October 12-16, 2014, Pittsburgh, Pennsylvania, USA.
12. **C. Hofmeister**, A. Giri, S. Brennan, Y.H. Sohn, T. Delahanty, K. Cho, "Effect of Process Control Agent on the Microstructure and Mechanical Behavior of an Aluminum and B_4C Metal Matrix Composite," Presented at the 2014 TMS Annual Meeting & Exhibition: Light-metal Matrix (Nano)-composites, February 16-20, 2014, San Diego, CA, USA.
13. **C. Hofmeister**, J. Hamilton O. Ahmed, W. Mohr, K. Cho, Y.H. Sohn, "Friction Stir Lap Joints between AA2139-T8 and B4C Reinforced AA5083 Metal Matrix Composites" (Poster), Presented at the 8th International Conference on Advanced Materials (THERMEC 2013), December 2-6, 2013, Las Vegas, USA.
14. Y.H. Sohn, B. Yao**, C. Hofmeister**, C. Kammerer, B. Masumdar, A. Giri, K. Cho, "Nano-scale Grain Size Effects Observed on Aluminum Metal Matrix Composites: Strengthening, Stability and Growth," Invited Presentation at 2013 TMS Annual Meeting & Exhibition: 2013 Symposium on Functional Nanomaterials – Synthesis, Properties and Applications, March 3-7, 2013, San Antonio, Texas, USA.
15. **C. Hofmeister**, T. Topping, M. van den Bergh, Y.H. Sohn, K. Cho, "Microstructural Characteristics of High Rate Plastic Deformation in Al Trimodal Metal Matrix Composites," Presented at the 13th International Conference on Aluminum Alloys, June 3-7, 2012, Pittsburgh, USA.
16. W. Mohr, M. van den Bergh, K. Cho, M. Shaeffer, Y.H. Sohn, **C. Hofmeister**, J. Seaman, "Friction Stir Processing of Trimodal 5083 for Improved Toughness," Presented at the Defense Manufacturing Conference (DMS 2011), November 28 - December 1, 2011, Anaheim, California, USA.
17. S. Harary, B. Yao, **C. Hofmeister**, T. Patterson, Yong-ho Sohn, "Microstructure of Al Trimodal Metal Matrix Composites" (Poster), Presented at NSTC/AMPAC K-12/Undergraduate/RET 2011 Summer Research Showcase, August 11, 2011, University of Central Florida, Orlando, FL, USA.
18. T. Patterson, **C. Hofmeister**, B. Yao, "Stability of Nanocrystalline Aluminum Grain Size in Cryomilled AA5083/B_4C Metal Matrix Composites," Presented at Symposium on Phase Stability, Diffusion, Kinetics and Their Applications (PSDK-V), Materials Science & Technology 2010 (MS&T2010), October 17-21, 2010, Houston, Texas, USA.
19. T. Patterson, B. Yao, **C. Hofmeister**, T. Zahrah, Y.H. Sohn, "Hot Isostatic Pressing of Trimodal Aluminum Metal Matrix Composites," Presented at Symposium on Fundamentals and Characterization: Recent Advances in Structural Characterization of

Materials, Materials Science & Technology 2010 (MS&T2010), October 17-21, 2010, Houston, Texas, USA.

20. T. Patterson, B. Yao, **C. Hofmeister**, B. Mohr, B. Thompson, Y.H. Sohn, "Microstructural Development in Friction Stir Welded Trimodal Aluminum Metal-Matrix Composite," Presented at Symposium on High Strain Rate Behaviors of Composites and Heterogeneous Materials: Experiments, Modeling, and Simulation, Materials Science & Technology 2010 (MS&T2010), October 17-21, 2010, Houston, Texas, USA.
21. B. Yao, **C. Hofmeister**, Y.H. Sohn, K. Cho, "Analytical Characterization and First-Principle Calculation of Dispersoids in Trimodal Aluminum Metal Matrix Composites," Presented at the 2010 International Conference on Powder Metallurgy & Particulate Materials, June 27-30, 2010, Hollywood, FL, USA.
22. Y.H. Sohn, B. Yao, T. Patterson, **C. Hofmeister**, H. Heinrich, "Microstructural Analysis for Manufacturing Optimization of Trimodal Al Matrix Composites," Invited Presentation at Aluminum for Defense Applications Workshop, May 3-4, 2010, Baltimore, MD, USA.
23. **C. Hofmeister**, B. Yao, T. Patterson, Y.H. Sohn, T. Delahanty, M. van den Bergh, K. Cho, "Composition and Structure of Nitrogen-Containing Dispersoids in Tri-Modal Metal Matrix Composites", Presented at the Florida Chapter of the AVS Science and Technology Society (FLAVS), March 7, 2010, University of Central Florida, Orlando, FL, USA.
24. **C. Hofmeister**, B. Yao, Y.H. Sohn, T. Delahanty, M. van den Bergh, K. Cho, "Composition and Structure of Nitrogen-containing Dispersoids in Tri-modal Metal Matrix Composites," Presented at 2010 TMS Annual Meeting & Exhibition: 6th International Symposium on Ultrafine Grained Materials, February 14-18, 2010, Seattle, WA, U.S.A.
25. B. Yao, **C. Hofmeister**, T. Patterson, Y.H. Sohn, K. Cho, "Effects of Processing on the Microstructure and Properties of the Commercial-Scale Trimodal Al Metal Matrix Composites," NATO Advanced Research Workshop on Boron Rich Solids, December 14-17, 2009, Orlando, Florida, USA.
26. B. Yao, **C. Hofmeister**, T.J. Patterson, Y.H. Sohn, G. Wolfe, M. van den Bergh, K. Cho, "Effects of Processing on The Microstructure and Properties of the Commercial-Scale Tri-Modal Al Metal Matrix Composites," Presented at Materials Science and Technology 2009 Conference, October 25-29, 2009, Pittsburgh, Pennsylvania, U.S.A.
27. **C. Hofmeister**, Y.H. Sohn, "Composition and Structure of Nitrogen-Containing Dispersoids in Trimodal Metal Matrix Composites," 2009 NanoFlorida: 2nd Annual NanoScience Technology Symposium, September 25-26, 2009, University of Central Florida, Orlando, Florida, U.S.A.
28. B. Yao, T. Patterson, **C. Hofmeister**, H. Heinrich, Y.H. Sohn, G. Wolfe, M. van den Burgh, K. Cho, "Engineering Properties via Microstructure Design of Commercial Scale Lightweight Nanoengineered Aluminum Composites," Presented at the 17th International Conference on Composite/Nano Engineering, July 26 – August 1, 2009, Honolulu, Hawaii, USA.
29. **C. Hofmeister**, B. Yao, T. Patterson, Y.H. Sohn, C.A. Smith, M. van den Bergh, K. Cho, "Microscopic and Spectroscopic Characterization of Cryomilled Nanostructure of Aluminum Alloy and B_4C Powders," Presented at 2009 TMS Annual Meeting &

Exhibition: Symposium on Nanostructured Composites, February 15-19, 2009, San Francisco, CA, U.S.A.

LIST OF REFERENCES

1. Sohn, Y.H., et al., *Tailoring Microstructure and Properties of Hierarchical Aluminum Metal Matrix Composites Through Friction Stir Processing.* Jom, 2012. **64**(2): p. 234-238.

2. Yao, B., et al., *Microstructural features influencing the strength of Trimodal Aluminum Metal-Matrix-Composites.* Composites Part A: Applied Science and Manufacturing, 2010. **41**(8): p. 933-941.

3. Witkin, D.B. and E.J. Lavernia, *Synthesis and mechanical behavior of nanostructured materials via cryomilling.* Progress in Materials Science, 2006. **51**(1): p. 1-60.

4. Hofmeister, C., et al., *Composition and structure of nitrogen-containing dispersoids in trimodal aluminum metal-matrix composites.* Journal of Materials Science, 2010. **45**: p. 4871-6.

5. Li, Y., et al., *HRTEM and EELS study of aluminum nitride in nanostructured Al 5083/B4C processed via cryomilling.* Acta Materialia, 2010. **58**(5): p. 1732-1740.

6. Estrada, J.L., J. Duszczyk, and B.M. Korevaar, *Gas entrapment and evolution in prealloyed aluminium powders.* Journal of Materials Science, 1991. **26**: p. 1431-1442.

7. Liddicoat, P.V., et al., *Nanostructural hierarchy increases the strength of aluminium alloys.* Nat Commun, 2010. **1**: p. 63.

8. Zhou, F., et al., *Microstructural evolution during recovery and recrystallization of a nanocrystalline Al-Mg alloy prepared by cryogenic ball milling.* Acta Materialia, 2003. **51**(10): p. 2777-2791.

9. Suryanarayana, C., *Mechanical alloying and milling.* Progress in Materials Science, 2001. **46**: p. 1-184.

10. Singer, R.F., W.C. Oliver, and W.D. Nix, *Identification of Dispersoid Phases Created in Aluminum During Mechanical Alloying.* Metallurgical and Materials Transactions A, 1980. **11A**: p. 1895-1901.

11. Bray, J.W., *Aluminum Mill and Engineered Wrought Products*, in *ASM Metals Handbook Volume 2 - Properties and Selection: Nonferrous Alloys and Special-Purpose Materials*. 1990, ASM. p. 118-138.

12. Cayless, R.B.C., *Alloy and Temper Designation Systems for Aluminum and Aluminum Alloys*, in *ASM Metals Handbook Volume 2 - Properties and Selection: Nonferrous Alloys and Special-Purpose Materials*. 1990, ASM. p. 41-112.

13. Nam, S.W. and D.H. Lee, *The Effect of Mn on the Mechanical Behavior of Al Alloys.* Metals and Materials, 2000. **6**(1): p. 13-16.

14. Okamoto, H., *Al-Mg (Aluminum-Magnesium).* Journal of Phase Equilibria, 1998. **19**(6): p. 598.

15. Sridharan, K., et al., *Mitigation of Corrosion in 5xxx Series Al-Mg Alloys in Marine Environments: Grain Boundary Engineering and Cold Spray Coating Approaches*, D.o. Defense, Editor. 2014, Office of Naval Research: Arlington, VA. p. 1-71.

16. Raghavan, V., *Al-Mg-Mn (Aluminum-Magnesium-Manganese).* Journal of Phase Equilibria and Diffusion, 2009. **30**(6): p. 626-629.

17. Dieter, G.E., *Strengthening Mechanisms*, in *Mechanical Metallurgy*, M.B. Bever, et al., Editors. 1976, McGraw-Hill: New York. p. 190-246.

18. Hasegawa, H., et al., *Thermal stability of ultrafine-grained aluminum in the presence of Mg and Zr additions.* Materials Science and Engineering A, 1999. **265**: p. 188-196.

19. Fecht, H.-J., *Nanostructure Formation by Mechanical Attrition.* NanoStructured Materials, 1995. **6**: p. 33-42.

20. Goujon, C., et al., *Mechanical alloying during cryomilling of a 5000 Al alloy/AlN powder: the effect of contamination.* Journal of Alloys and Compounds, 2001. **315**: p. 276-283.

21. Hashemi-Sadraei, L., et al., *Influence of Nitrogen Content on Thermal Stability and Grain Growth Kinetics of Cryomilled Al Nanocomposites.* Metallurgical and Materials Transactions A, 2011. **43**(2): p. 747-756.

22. Hull, D. and D.J. Bacon, *Dislocations*, in *Introduction to Dislocations*. 2001, Butterworth Heinemann: Oxford. p. 14-21.

23. Ramesh, K.T., *Plastic Deformation of Nanomaterials*, in *Nanomaterials: Mechanics and Mechanisms*. 2009, Springer Dordrecht Heidelberg: New York. p. 121-178.

24. Bahrami, A., A. Miroux, and J. Sietsma, *Modeling of Strain Hardening in the Aluminum Alloy AA6061.* Metallurgical and Materials Transactions A, 2013. **44**(5): p. 2409-2417.

25. Barlat, F., *A simple model for dislocation behavior, strain and strain rate hardening evolution in deforming aluminum alloys.* International Journal of Plasticity, 2002. **18**(7): p. 919-939.

26. El-Awady, J.A., *Unravelling the physics of size-dependent dislocation-mediated plasticity.* Nat Commun, 2015. **6**: p. 5926.

27. Ye, J., et al., *A tri-modal aluminum based composite with super-high strength.* Scripta Materialia, 2005. **53**(5): p. 481-486.

28. Lucadamo, G., et al., *Microstructure characterization in cryomilled Al 5083.* Materials Science and Engineering A, 2006. **430**(1-2): p. 230-241.

29. Rooy, E.L., *Introduction to Aluminum and Aluminum Alloys*, in *ASM Metals Handbook Volume 2 - Properties and Selection: Nonferrous Alloys and Special-Purpose Materials*. 1990, ASM. p. 17-38.

30. *Al6Mn (MnAl6) Crystal Structure: Datasheet from "LINUS PAULING FILE Multinaries Edition – 2012" in SpringerMaterials* http://materials.springer.com/isp/crystallographic/docs/sd_1210771*)*, P. Villars and K. Cenzual, Editors. 2014, Springer-Verlag Berlin Heidelberg & Material Phases Data System (MPDS), Switzerland & National Institute for Materials Science (NIMS), Japan.

31. Benjamin, J.S. and J. Bomford, *Dispersion Strengthened Aluminum Made by Mechanical Alloying.* Metallurgical and Materials Transactions A, 1977. **8A**: p. 1301-5.

32. Hofmeister, C., et al. *Effect of Process Control Agent on the Microstructure and Mechanical Behavior of an Aluminum and B4C Metal Matrix Composite*. in *TMS (The Minerals, Metals & Materials Society), 2014*. 2014. San Diego, CA: John Wiley & Sons, Inc.

33. Hofmeister, C., et al., *Quantification of nitrogen impurity and estimated Orowan strengthening through secondary ion mass spectroscopy in aluminum cryomilled for extended durations.* Materials Science and Engineering A, 2015. **648**: p. 412-417.

34. *Al4C3 Crystal Structure: Datasheet from "LINUS PAULING FILE Multinaries Edition – 2012" in SpringerMaterials (*http://materials.springer.com/isp/crystallographic/docs/sd_1250388*)*, P. Villars and K. Cenzual, Editors. 2014, Springer-Verlag Berlin Heidelberg & Material Phases Data System (MPDS), Switzerland & National Institute for Materials Science (NIMS), Japan.

35. Lawley, A., *Physicochemical Considerations in Powder Metallurgy.* Journal of Materials, 1990. **42**(4): p. 12-14.

36. Kowalski, L., B.M. Korevaar, and J. Duszczyk, *Some new aspects of the theory of oxidation and degassing of aluminium-based alloy powders.* Journal of Materials Science, 1992. **27**: p. 2770-2780.

37. Tellkamp, V.L., et al., *Grain growth behavior of a nanostructured 5083 Al-Mg alloy.* Journal of Materials Research, 2001. **16**(4): p. 938-944.

38. Schneider, C.A., W.S. Rasband, and K.W. Eliceiri, *NIH Image to ImageJ: 25 years of image analysis.* Nature Methods, 2012. **9**(7): p. 671-675.

39. Williamson, G.K. and R.E. Smallman, *Dislocation Densities in Some Annealed and Cold-Worked Metals from Measurements on the X-ray Debye-Scherrer Spectrum.* Philosophical Magazine, 1956. **1**(1): p. 34-46.

40. Smallman, R.E. and K.H. Westmacott, *Stacking Faults in Face-Centered Cubic Metals and Alloys.* Philosophical Magazine, 1957. **2**(17): p. 669-683.

41. Mhadhbi, M., et al., *Characterization of Mechanically Alloyed Nanocrystalline Fe(Al): Crystallite Size and Dislocation Density.* Journal of Nanomaterials, 2010. **2010**: p. 1-8.

42. Zhao, Y.H., et al., *Microstructures and mechanical properties of ultrafine grained 7075 Al alloy processed by ECAP and their evolutions during annealing.* Acta Materialia, 2004. **52**(15): p. 4589-4599.

43. Zhao, Y.H., H.W. Sheng, and K. Lu, *Microstructure Evolution and Thermal Properties in Nanocrystalline Fe During Mechanical Attrition.* Acta Materialia, 2001. **49**: p. 365-375.

44. Tellkamp, V.L., A. Melmed, and E.J. Lavernia, *Mechanical Behavior and Microstructure of a Thermally Stable Bulk Nanostructured Al Alloy.* Metallurgical and Materials Transactions A, 2001. **32A**.

45. Cullity, B.D., *Elements of X-Ray Diffraction*. 1978, Reading, Massachusetts: Addison-Wesley Publishing Company, Inc.

46. McAlister, A.J. and J.L. Murray, *Al-Mn (Aluminum - Manganese)*, in *ASM Metals Handbook: Alloy Phase Diagrams*, H. Baker, Editor. 1987, ASM International. p. 307-308.

47. San-Martin, A. and F.D. Manchester, *Al-H (Aluminum - Hydrogen)*, in *ASM Metals HandBook*. 1992, ASM. p. 299.

48. Hu, H., *Recovery, Recrystallization, and Grain-Growth Structures*, in *ASM Handbook*. 1992, ASM International. p. 1497-1512.

49. Zhou, F., et al., *High Grain Size Stability of Nanocrystalline Al Prepared by Mechanical Attrition.* Journal of Materials Research, 2001. **16**(12): p. 3451-3458.

50. Maung, K., et al., *Thermal stability of cryomilled nanocrystalline aluminum containing diamantane nanoparticles.* Journal of Materials Science, 2011. **46**: p. 6932-6940.

51. Roy, I., et al., *Thermal Stability in Bulk Cryomilled Ultrafine-Grained 5083 Al Alloy.* Metallurgical and Materials Transactions A, 2006. **37A**: p. 721-730.

52. Mohamed, F.A. and T.G. Langdon, *Deformation Mechanism Maps Based on Grain Size.* Metallurgical Transactions, 1974. **5**: p. 2339-2345.

53. Rothman, S.J., et al., *Tracer Diffusion of Magnesium in Aluminum Single Crystals.* Physica status solidi (B), 1974. **63**: p. K29-K33.

54. Heitjans, P. and J. Karger, *Diffusion in Condensed Matter: Methods, Materials, Models*. 2005, New York: Springer-Verlag Berlin Heidelberg.

55. Harrison, L.G., *Influence of Dislocations on Diffusion Kinetics in Solids with Particular Reference to the Alkali Halides.* Transactions of the Faraday Society, 1961. **57**: p. 1191-1199.

56. Belova, I.V. and G.E. Murch, *The transition from Harrison type-B to type-A kinetics in grain-boundary tracer diffusion.* Philosophical Magazine A, 2001. **81**(10): p. 2447-2455.

57. Mehrer, H., *Diffusion in Solids: Fundamentals, Methods, Materials, Diffusion-Controlled Processes*. Solid-State Sciences, ed. M. Cardona, et al., New York: Springer-Verlag Berlin Heidelberg. 1-645.

58. Crank, J., *Mathematics of Diffusion*. 1964, Amen House, London: Oxford University Press.

59. Young, G.A. and J.R. Scully, *The Diffusion and Trapping of Hydrogen in High Purity Aluminum.* Acta Materialia, 1998. **46**(18): p. 6337-6349.

60. Ye, J., J. He, and J.M. Schoenung, *Cryomilling for the Fabrication of a Particulate B4C Reinforced Al Nanocomposite: Part I. Effects of Process Conditions on Structure.* Metallurgical and Materials Transactions A, 2006. **37A**: p. 3099-3109.

61. Saitoh, H., Y. Iijima, and H. Tanaka, *Hydrogen diffusivity in aluminium measured by a glow discharge permeation method.* Acta Metallurgica et Materialia, 1994. **42**(7): p. 2493-2498.

62. Hashimoto, E. and T. Kino, *Hydrogen diffusion in aluminium at high temperatures.* Journal of Physics F: Metal Physics, 1983. **13**(6): p. 1157-1166.

63. Papp, K. and E. Kovacs-Csetenyi, *Diffusion of hydrogen in solid aluminium.* Scripta Metallurgica, 1977. **11**(11): p. 921-923.

64. *Al2O3 Crystal Structure: Datasheet from "LINUS PAULING FILE Multinaries Edition – 2012" in SpringerMaterials (*http://materials.springer.com/isp/crystallographic/docs/sd_0541335*)*, P. Villars and K. Cenzual, Editors. 2014, Springer-Verlag Berlin Heidelberg & Material Phases Data System (MPDS), Switzerland & National Institute for Materials Science (NIMS), Japan.

65. *Al-N*, in *Landolt-Bornstein - Group IV Physical Chemistry Numberical Data and Functional Relationships in Science and Technology*. SpringerMaterials. p. 173-174.

66. *AlN Crystal Structure: Datasheet from "LINUS PAULING FILE Multinaries Edition – 2012" in SpringerMaterials (*http://materials.springer.com/isp/crystallographic/docs/sd_1623783*)*, P. Villars and K. Cenzual, Editors. 2014, Springer-Verlag Berlin Heidelberg & Material Phases Data System (MPDS), Switzerland & National Institute for Materials Science (NIMS), Japan.